

Investigation of Lithium Ion Battery Electrodes:  
Using Mathematical Models Augmented with Data  
Science to Understand Surface Layer Formation, Mass  
Transport, Electrochemical Kinetics, and Chemical  
Phase Change

Nicholas W. Brady

Submitted in partial fulfillment of the  
requirements for the degree of  
Doctor of Philosophy  
in the Graduate School of Arts and Sciences

Columbia University

2019

© 2019

Nicholas William Brady

All rights reserved

# Abstract

Investigation of Lithium Ion Battery Electrodes: Using Mathematical Models Augmented with Data Science to Understand Surface Layer Formation, Mass Transport, Electrochemical Kinetics, and Chemical Phase Change

Nicholas W. Brady

This thesis first uses physical scale models to investigate solid-state phenomena - surface layer formation, solid-state diffusion of lithium, electrochemical reactions at the solid-electrolyte interface, as well as homogeneous chemical phase change reactions. Evidence is provided that surface layer formation on the magnetite,  $\text{Fe}_3\text{O}_4$ , electrode can accurately be described mathematically as a nucleation and growth process. To emulate the electrochemical results of the  $\text{LiV}_3\text{O}_8$  electrode, a novel method is developed to capture the phase change process; this method describes phase change as a nucleation and growth process. The physical parameters of the  $\text{LiV}_3\text{O}_8$  electrode: the solid-state diffusion coefficient, phase change saturation concentration, phase reaction rate constant, and exchange current density, are all quantified and the agreement with experimental results is compelling. Electrochemical evidence, corroborated by results from density functional theory, indicate that delithiation is a more facile process than lithiation in the  $\text{LiV}_3\text{O}_8$  electrode.

Further investigation of the  $\text{LiV}_3\text{O}_8$  electrode is undertaken by coupling the crystal scale model to electrode scale phenomena. Characterization of the  $\text{LiV}_3\text{O}_8$  electrode by operando EDXRD experiments provides a unique and independent set of observations

that validate the previously estimated physical constants for the phase change saturation concentration and phase change reaction rate constant; they are both found to be consistent with their previous estimates. Finally, it is observed that anodic physical phenomena are important during delithiation of the cathode because the kinetics at the anode become mass-transfer limited.

Finally, it is illustrated that coupling physical models to data science and algorithmic computing is an effective method to accelerate model development and quantitatively guide the design of experiments.

# Contents

|   |           |
|---|-----------|
| <b>List of Figures</b>  | <b>iv</b> |
| <b>List of Tables</b>   | <b>xi</b> |
| <b>Chapter 1: Introduction</b>  | <b>1</b>  |
| 1.1 Why batteries? . . . . .  | 2         |
| 1.2 Why Modeling? . . . . .   | 2         |
| 1.3 Why Data Science? . . . . .   | 3         |
| 1.4 Bibliography . . . . .  | 5         |
| <b>Chapter 2: Galvanostatic Interruption of Lithium Insertion into Magnetite: Evidence of Surface Layer Formation</b> | <b>7</b>  |
| 2.1 Introduction . . . . .  | 8         |
| 2.2 Experimental . . . . .  | 9         |
| 2.3 Theory . . . . .  | 10        |
| 2.4 Surface Layer Formation . . . . .   | 11        |
| 2.5 Salt Saturation Limit . . . . .   | 12        |
| 2.6 Results and Discussion . . . . .  | 13        |
| 2.7 Conclusions . . . . .   | 20        |
| 2.8 Acknowledgements . . . . .  | 20        |
| 2.9 List of Symbols . . . . .   | 21        |
| 2.10 Bibliography . . . . .   | 22        |

|                   |  |           |
|-------------------|--|-----------|
| <b>Chapter 3:</b> | <b>Discharge, Relaxation, and Charge Model for the Lithium<br/>Trivanadate Electrode: Reactions, Phase Change, and Trans-<br/>port</b> | <b>25</b> |
| 3.1               | Introduction . . . . .   | 26        |
| 3.2               | Experimental . . . . .   | 27        |
| 3.2.1             | Materials Synthesis and Characterization . . . . .   | 28        |
| 3.2.2             | Electrochemical Measurements . . . . .   | 28        |
| 3.2.3             | Ab-Initio Theory Calculations . . . . .  | 28        |
| 3.2.4             | Experimental Results . . . . .   | 29        |
| 3.3               | Theory . . . . .   | 30        |
| 3.3.1             | Boundary and Initial Conditions . . . . .  | 34        |
| 3.3.2             | Kinetics of Phase Change . . . . .   | 35        |
| 3.3.3             | Numerical Methods . . . . .  | 37        |
| 3.4               | Parameter Estimation . . . . .   | 38        |
| 3.5               | Results . . . . .  | 42        |
| 3.6               | Conclusions . . . . .  | 46        |
| 3.7               | Acknowledgements . . . . .   | 46        |
| 3.8               | Appendix A . . . . .   | 47        |
| 3.9               | Appendix B . . . . .   | 48        |
| 3.10              | List of Symbols . . . . .  | 50        |
| 3.11              | Bibliography . . . . .   | 52        |
| <b>Chapter 4:</b> | <b><i>Operando</i> Study of LiV<sub>3</sub>O<sub>8</sub> Cathode: Coupling EDXRD<br/>Measurements to Simulations</b>                   | <b>55</b> |
| 4.1               | Introduction . . . . .   | 56        |
| 4.2               | Experimental . . . . .   | 58        |
| 4.3               | Theory . . . . .   | 59        |
| 4.3.1             | Boundary and Initial Conditions . . . . .  | 62        |
| 4.3.2             | Numerical Methods . . . . .  | 64        |
| 4.4               | Results . . . . .  | 66        |

|   |   |            |
|---|---|------------|
| 4.5   | Conclusions . . . . .   | 73         |
| 4.6   | Acknowledgements . . . . .                                    | 74         |
| 4.7   | Bibliography . . . . .  | 75         |
| <b>Chapter 5: Quantitative Parameter Estimation, Model Selection, and<br/>Variable Selection in Battery Science</b> |   | <b>77</b>  |
| 5.1   | Introduction . . . . .  | 78         |
| 5.2   | Methods . . . . .   | 81         |
| 5.2.1   | Sampling . . . . .  | 82         |
| 5.2.2   | Markov-Chain Monte-Carlo . . . . .                            | 83         |
| 5.2.3   | Physical Model of $\text{Li}_x\text{V}_3\text{O}_8$ . . . . . | 84         |
| 5.2.4   | Algorithmic Model Development and Analysis . . . . .          | 85         |
| 5.3   | Results and Discussion . . . . .                              | 86         |
| 5.3.1   | Parameter Estimation . . . . .                                | 86         |
| 5.3.2   | Model Selection . . . . .                                     | 90         |
| 5.3.3   | Variable Selection . . . . .                                  | 93         |
| 5.3.4   | Model Guided Design of Experiment . . . . .                   | 96         |
| 5.4   | Conclusion . . . . .  | 100        |
| 5.5   | Acknowledgements . . . . .                                    | 100        |
| 5.6   | Bibliography . . . . .  | 102        |
| <b>Chapter 6: Conclusion</b>  |   | <b>107</b> |

# List of Figures

|            |  |    |
|------------|--|----|
| Figure 2.1 | Voltage recovery for 6 nm $\text{Fe}_3\text{O}_4$ electrodes that were initially lithiated to an average lithium concentration of $\text{Li}_{0.5}\text{Fe}_3\text{O}_4$ . Simulations with surface layer formation were conducted using $n = 1, 2, 3,$ or $4$ in the Avrami equation (Eq. 2.3). Inset provides a visualization of the proposed mechanism of surface layer formation: progressive nucleation and three-dimensional growth ( $n = 4$ ). . . . . | 14 |
| Figure 2.2 | Side by side comparisons of experimental and simulated lithiation and voltage recovery for electrodes comprised of a) 6 nm and b) 8 nm crystals. Recovery was conducted after lithiation to different levels of intercalation ( <i>i.e.</i> , $x$ in $\text{Li}_x\text{Fe}_3\text{O}_4$ ). Each experiment was conducted with a separate cell. . . . .   | 15 |
| Figure 2.3 | Experimental and simulated voltage during: I) first oxidation at $C/200$ , then constant voltage hold at 3.0 V), II) second reduction at $C/200$ , and III) second voltage recovery (open circuit). The first oxidation was conducted after a reduction to $x = 0.5$ (for $x$ in $\text{Li}_x\text{Fe}_3\text{O}_4$ ) and an OCP relaxation for 30 days. . . . .   | 16 |
| Figure 2.4 | Experiments and simulations of the second voltage recovery with simulations accounting for (solid) and not accounting for (dashed) active material transformation. Comparisons are made for a) $x = 0.5$ and b) $x = 1.0$ in $\text{Li}_x\text{Fe}_3\text{O}_4$ . . . . .  | 18 |
| Figure 2.5 | Plot comparing the active material lost (not utilized) due to transformation (left-axis) and active material not utilized due to solid-state transport resistances (right-axis). . . . .   | 19 |

|            |  |    |
|------------|--|----|
| Figure 3.1 | SEM images of $\text{LiV}_3\text{O}_8$ crystals sintered at $550^\circ\text{C}$ for 2 hours. The inset highlights a representative crystal with the three faces labeled with their respective planes. . . . .  | 27 |
| Figure 3.2 | Representative potential curve during discharge and recovery. The constant voltage plateau seen during the discharge indicates a two-phase region. The voltage recovery (inset) is divided into charge-transfer losses ( $\eta_{CT}$ ) and mass-transfer losses ( $\eta_{MT}$ ). The characteristic relaxation time, $\tau$ , is also determined from the voltage recovery data. . . . .   | 29 |
| Figure 3.3 | (Top) Schematic of the modeling domain. It is assumed that $\text{Li}^+$ predominantly inserts through the (001) crystal face and therefore concentration variations only occur along the [001] direction. (Bottom) Qualitative representations of two models for phase-change are compared: the commonly utilized shrinking-core method and the nucleation and growth model. As lithium is inserted into the material, the concentration of lithium increases. Once the concentration of lithium exceeds the saturation value, phase change commences, and a new lithium rich $\beta$ -phase is created. As more lithium is inserted, the amount of $\beta$ -phase increases. The shrinking-core method assumes that the new phase forms in a layer by layer process, while the nucleation and growth model produces a profile that is similar, but with a more dispersed $\beta$ -phase. . . . . | 31 |
| Figure 3.4 | A) Illustration of the effect of changing $\psi_{Th}$ on the $\theta_\beta$ profile within the crystal for $\bar{i} = 10$ . The profiles are also compared to the profiles produced using the shrinking-core model; it can be seen that at high values of $\psi_{Th}$ , the model collapses to the shrinking-core model. B) Illustration of the effect of changing $\bar{i}$ on the $\theta_\beta$ profile within the crystal for $\psi_{Th} = 5$ . . . . .  | 36 |
| Figure 3.5 | An illustration of the $\theta_\beta$ profile within a crystal ( $\psi_{Th} = 10,000$ , $m = 0$ ) during a current cycling process ( $\bar{i} = 60$ ). The predicted spatial variation of the regions with two phases is a strong function of the battery usage. . . . .   | 37 |

|             |  |    |
|-------------|--|----|
| Figure 3.6  | Qualitative comparisons used for parameter estimation of A) $k_{rxn}$ , B) $D_\alpha$ , C) $x_{\alpha,sat}$ , and D) $k_\beta$ . A) compares varying exchange current densities with the charge-transfer losses at different current rates. B) compares varying diffusion coefficient at a current rate of 1C; C) and D) compare varying saturation concentrations and phase change reaction coefficients, respectively, with experiments conducted at C/10. . . . .         | 39 |
| Figure 3.7  | Experimental (dashed lines) and simulated (solid lines) potential during discharge (lithiation) and after interruption of current. Comparisons are shown for four discharge rates. The rapid change in slope of the curves is the result of current interruption. . . . .  | 42 |
| Figure 3.8  | Experimental (A) potential during charge (delithiation) at different rates. The corresponding simulated (B) potential is shown for comparison. The simulations do not capture the relatively small changes in potential with charge rate observed at low equivalence. . . . .  | 44 |
| Figure 3.9  | Experimental (A) potential during charge and discharge at different rates. The corresponding simulated (B) potential is shown for comparison. If the diffusion coefficient is increased during charge, then the simulation curves collapse onto each other as is observed experimentally, providing significant improvement from those observed in Figure 3.8. . . . .   | 45 |
| Figure 3.10 | Estimation of the potential drops in the lithium trivanadate electrode at a current rate of C/5, focusing on the two-phase region. The graph shows qualitatively the contributions to the observed overpotential. 1) reversible potential, 2) charge-transfer resistance only, 3) charge-transfer and estimated phase-change resistances, assuming no concentration variations, 4) charge transfer, estimated phase-change, and estimated mass-transfer resistances. . . . . | 45 |
| Figure 3.11 | Open-circuit voltage measurements (squares) were taken and the empirical open-circuit voltage curve (solid red) was constructed to reside between the discharge and charge curve (dashed) at the lowest current rate.  | 49 |

|            |  |    |
|------------|--|----|
| Figure 4.1 | The volume fraction of $\beta$ -phase in a 561 $\mu\text{m}$ thick $\text{LiV}_3\text{O}_8$ cathode as a function of position at 0, 1, 2, and 10 hours after the end of discharge.   | 57 |
| Figure 4.2 | A schematic of the setup used for operando EDXRD measurements. White beam radiation was focused to a final gauge volume of $3.6 \times 0.1 \times 0.02 \text{ mm}^3$ . Coin cells were placed on the sample stage, which was moved vertically in 20 $\mu\text{m}$ increments to acquire the EDXRD patterns for various regions inside the cell. The germanium energy detector was set to $2\theta = 3^\circ$ .       | 59 |
| Figure 4.3 | Cell potential of a 561 $\mu\text{m}$ thick $\text{LiV}_3\text{O}_8$ cathode discharge data current rate of C/18. Dashed (black) lines are experimental measurements. Simulations neglecting electrode scale resistances (i.e. only modeling crystal-scale resistances) are shown in green and simulations accounting for both electrode and crystal scale resistances in blue, assuming $\epsilon = 0.45$ .         | 67 |
| Figure 4.4 | Simulated and experimental potential as a function of state of charge at a current rate of C/18. The points along the simulation curve correspond to the average equivalence of the EDXRD scans. The insets are model predictions for the concentration profiles of lithium in the $\alpha$ -phase as well as the volume fraction of $\beta$ -phase as a function of electrode position.                             | 68 |
| Figure 4.5 | A) The position (measured from separator) where $\beta$ -phase is present as a function of the state of charge. Points are determined from the EDXRD measurements and the solid lines are simulations of this interface assuming volume fractions of 0%, 5%, and 10% as the detection thresholds. B) Representative EDXRD scan illustrating how the scans were analyzed to determine the presence of $\beta$ -phase. | 69 |
| Figure 4.6 | The position (measured from separator) where $\beta$ -phase is present as a function of the state of charge. Points are determined from the EDXRD measurements and the solid lines are simulations of this interface. Simulations show the sensitivity of the model to phase-change kinetic parameters A) $k_\beta$ and B) $x_{\alpha,sat}$ , assuming a 5% volume fraction detection limit.                         | 69 |

|            |  |    |
|------------|--|----|
| Figure 4.7 | Simulated and experimental cell potential as a function of state of charge at a current rate of C/18. Simulations are shown as the blue solid line and experiments as the black dashed line. The points along the simulation curve indicate the average equivalence when EDXRD scans were taken during delithiation. The insets are two scans at the end of delithiation, $x \sim 1.5$ (scan 18) and $x \sim 1.3$ (scan 19) in $\text{Li}_x\text{V}_3\text{O}_8$ . . . . . | 70 |
| Figure 4.8 | Simulated volume fraction of $\beta$ -phase, $\theta_\beta$ , as a function of electrode position (measured from separator) for an $\text{LiV}_3\text{O}_8$ electrode 561 $\mu\text{m}$ thick and operated at a current rate of C/18. Solid lines track the evolution of the $\beta$ -phase profile during lithiation, and dashed lines track the disappearance of the $\beta$ -phase during delithiation. . . . .   | 72 |
| Figure 4.9 | A) Simulated concentration profiles of $\text{Li}^+$ ions in the electrolyte for varying degrees of lithiation and delithiation. B) The deviation of the positional overpotential from the overpotential if there were no concentration variations in the electrolyte for lithiation (solid) and delithiation (dashed). . . . .  | 73 |
| Figure 5.1 | Flow diagram illustrating a computationally scalable framework to perform model development and subsequent analysis of the model output. . . . .   | 86 |
| Figure 5.2 | Physical model parameter estimates obtained from Sobol sampling followed by Markov-Chain Monte-Carlo analysis using the lithiation and voltage recovery data from all four current rates. . . . .  | 87 |
| Figure 5.3 | Physical model parameter estimates obtained from Sobol sampling calculation of the likelihood of the parameter values using equation 5.3. The comparison with 5.2 shows that the derived parameter estimates are identical. This indicates that this simpler, more efficient method can be used in place of MCMC after Sobol sampling to obtain identical results. . . . .   | 88 |

Figure 5.4 A) Parameter distribution estimates for the solid-state diffusion coefficient,  $D_\alpha$ , obtained from the lithiation data at C/10 using two different estimates of the experimental standard deviation: uniform estimates of  $s_{exp} = 100, 50,$  and  $20$  mV, and an empirically determined estimate, which is shown as the inset. B) Comparison of the simulated data with parameter estimates from assuming  $s_{exp} = 50$  mV (green) and parameter estimates from using the empirically calculated deviation (blue). The C/10 lithiation data are shown in black; the error bars show the experimental deviation. 89

Figure 5.5 A) The MCMC determined distributions of the diffusive mass-transfer coefficient  $D_{agg}$  for the agglomerate scale model and B) the MCMC determined distributions of the solid-state mass-transfer coefficient,  $D_x$ , for crystal scale model. The parameters were determined using discharge data (blue) as well voltage recovery data (red). C) Comparisons of the simulated data using the mass-transfer coefficients determined by fitting each model to the relaxation data. The inset shows the average test error per experimental lithiation data point. . . . . 91

Figure 5.6 A) The average deviation per observation between the simulations and experiments versus the value of  $\lambda$ . B) The optimum values of  $\beta_j$  versus the value of  $\lambda$ . The vertical dashed lines indicate the value of  $\lambda$  where an additional parameter is allowed to vary (an additional  $\beta_j \neq 0$ ). A grid mesh of  $13 \times 13 \times 13$  was constructed and the  $\beta_j$ 's were allowed to vary from  $[0, 1]$  for each parameter. . . . . 93

Figure 5.7 The left two plots show, for given true values of  $k_\beta$ , how the estimated value of  $k_\beta$ ,  $\mu_{k_\beta}$ , and the uncertainty in the estimation,  $\sigma_{k_\beta}$ , vary for different applied currents. The right two plots show, for  $k_\beta = 5 \times 10^{-3} \text{ s}^{-1}$  (red), how the apparent value,  $\mu_{k_\beta}$ , and uncertainty,  $\sigma_{k_\beta}$ , vary for different applied currents. These data are overlaid with the estimated value and uncertainty of  $k_\beta$  derived from four current rates: C/10, C/5, C/2, 1C. . 96

Figure 5.8 The plot on the left shows how the best simulated  $\theta_\beta$  profile compares to the ideal profile as a function of applied current. The plot on the right shows representative  $\theta_\beta$  plots for three current rates: 2, 18, and 30 mA/g as well as the defined ideal profile. . . . . 98

# List of Tables

|           |   |    |
|-----------|---|----|
| Table 2.1 | Comparison of governing equations for model with and without transformation of $\text{Fe}_3\text{O}_4$ to an inactive state due to reactions with the electrolyte. . . . .  | 11 |
| Table 3.1 | Value of $m$ for different mechanisms of phase change . . . . .   | 35 |
| Table 3.2 | Parameter values used to model the $\text{LiV}_3\text{O}_8$ electrode. . . . .  | 41 |
| Table 3.3 | Parameters for the empirical open circuit potential of the $\alpha$ -phase derived from the Redlich-Kister expression (see equation 3.28 and Figure 3.11). . . . .  | 50 |
| Table 4.1 | Comparison of model parameters from previously published study and current study on the $\text{LiV}_3\text{O}_8$ . . . . .  | 60 |
| Table 4.2 | Governing equations and boundary conditions used to model the thick $\text{LiV}_3\text{O}_8$ electrode. The crystal scale and electrochemical reaction rate equations are consistent with those reported by Brady et al. <sup>6</sup> . . . . | 66 |
| Table 5.1 | Correlation between the simulation parameters and agreement with experimental observations ( $RSS$ ) for a given applied current. . . . .   | 83 |
| Table 5.2 | Physical equations used to model the $\text{Li}_x\text{V}_3\text{O}_8$ cathode. . . . .   | 85 |
| Table 5.3 | The estimated mean and standard deviation for the physical parameters as a function of applied current, as well as the estimates and standard deviations derived using all rates. . . . .   | 87 |

# Acknowledgements

First, I would like to thank my advisor, Dr. Alan West for the excellent guidance and opportunities he has given me, as well as for his patience. I would like to thank my family, especially my mother, father, and sister, who even though were far away were still able to provide ample support. I would like to thank my experimental collaborators at Stony Brook University and Brookhaven National Lab in particular, Dr. Esther Takeuchi, Dr. Amy Marschilok, Dr. David Bock, Dr. Ping Liu, Dr. Qing Zhnag, Dr. Christiana Cama, and Dr. Andrea Bruck; their input and excellent scientific endeavors made my work more enjoyable and meaningful. I would like to thank current and former members of the West group for their support, advice, and commraderie, especially Dr. Kevin Knehr, Dr. Christianna Lininger, Christian Gould, Jon Vardner, Zeyu Hui, and Karthik Mayilvahanan. I would like to give a special thanks to Dr. Tim Jones whose help was essential in applying statistical methods to our model development process. I would like to thank my long-time roommates and friends Dr. Swupnil Sahai, Dr. George Mountoufaris, Sebastian Russell, and Scarlett Wang for making my home in New York City exciting and welcoming. I would especially like to thank the front office: Kathy Marte, Ariel Sanchez, Rezarta Binaj, and Aurna Malakar for making sure I hit my milestones for always having time to help me solve problems. I would like to thank Dr. Mayank Misra and Dr. Thi Vo; they were invaluable resources in helping me develop my scripting algorithms. I would like to thank those I have shared an office with: Dr. Jack Davis, Dr. Brian Tackett, Dr. Christianna Lininger, Dr. Weiming Wan, Anna Dorfi, Marissa Beatty, Dr. Xiangye Liu, Jon Vardner, Ryan Gusley, Zhexi Lin, Xiaoran Niu, Steven Denny, and Dr. Natalie Labrador - I remember it fondly, others may have different perspectives. To the Latin

Dance Club at the Columbia Medical School, the Riverside Premier League, and the countless people who I have played soccer, basketball, and cycled with thanks for keeping me active. To those who I played Avalon with, I was always good; Sebastian was always evil. I would like to thank my uncle Bill for always inviting me to watch either the NCAA tournament or the NBA finals - I always enjoyed it and looked forward to it and gave me a fun outlet from scientific research. I would like to thank my committee members for agreeing to review my thesis and ensure that I am producing the best possible work.

Finally, I would like to thank the amazing friends I have made during my time at Columbia and in New York City: Jack Davis, Brian Tackett, Christianna Lininger, Andrew Jimenez, Jessica Small, Xiangye Liu, Weiming Wan, Zhexi Lin, Sara Hamilton, Xiaoran Niu, Sebastian Russell, Swupnil Sahai, Tim Jones, and Jon Vardner to name but a few.

# Chapter 1

## Introduction

Energy storage technology can be used to complement both existing traditional power generation and rising renewable energy sources, such as wind and solar.<sup>1,2</sup> In the absence of energy storage technology, energy needs to be produced to match demand. This means that power plants are not designed to meet average power demand, but peak power demand. These limitations prevent power plants from being designed with a practical sense of efficiency. Using energy storage would allow power plants to be designed closer to the average daily power demand, instead of peak demand.<sup>1,2</sup> In addition to traditional power generation, electrical energy storage will be necessary for the widespread implementation of intermittent renewable energy sources such as wind and solar.<sup>1,2</sup>

## 1.1 Why batteries?

Several technologies are being investigated for electrical energy storage applications such as pumped hydro, compressed air energy storage, flow cells, and fuel cells to name a few.<sup>1,2</sup> Batteries, in particular lithium ion batteries, are attractive electrical energy storage devices because they deliver high round trip efficiency, low self-discharge rates, reasonable cycle lives, and have demonstrated scalability.<sup>1,2</sup> In addition to grid level applications of lithium ion batteries, lithium ion batteries currently are the most common type of battery found in electric vehicles due to their high gravimetric energy density. According to both Exxon Mobil<sup>3</sup> and the International Energy Agency (IEA)<sup>4</sup>, the number of electric vehicles in the global fleet is project to increase by 40× in the next 20 years, so research on lithium ion batteries has huge practical implications.

## 1.2 Why Modeling?

Batteries are inherently complex devices; the very nature of a battery involves at least two electrodes and an electrolyte and so it can become challenging and in some ways impossible to practically study individual components of a battery. Mathematical modeling provides a surrogate method to interrogate individual components of complex systems. There is a plethora of empirical evidence that mathematical models are effective

tools in studying complex systems, such as batteries.<sup>5-7</sup> In some situations, simulations are the only effective method to quantitatively interrogate battery physics and validate physical hypotheses, and because of this they are essential in deepening our understanding of the physical phenomena that govern performance. Models also allow us to identify what is still unknown and quantify our uncertainty. Finally, optimal design and control of these processes and devices will require physically accurate and predictive mathematical models.

### 1.3 Why Data Science?

Models are effective tools to interrogate the dynamic physics present in battery systems, however they are very time-consuming to develop. Optimizing the physical parameters to best fit the experimental data can take months. Testing new physical hypotheses often requires building a unique model for each hypothesis; because each model needs to be optimized for proper comparison with the experimental data, this process can take a month or more for each unique hypothesis. Human time is expensive, while computer time is cheap and getting cheaper every year. Being able to outsource some of the model development process to computers has the potential to accelerate and cheapen the process of battery material exploration.

There is strong empirical evidence (autonomous cars, strategic games<sup>8,9</sup>, spam filtering<sup>10</sup>, natural language processing<sup>11</sup>) that computer algorithms and artificial intelligence are capable of performing complex tasks and they are not only cheaper, but they can also be more effective than humans. It is important for all industries, including chemical engineering and even those in academic research, to recognize the rising utility of computational resources and adopt methodologies to try and leverage these potentially paradigm altering tools.<sup>12-14</sup>

While some aspects of the model development process use quantitative metrics for decision making, such as relaxation time-constant analysis to provide intuition about the dominant length scale, many other aspects of model development lack rigorous quan-

titative metrics for model selection or decision making in general. Selecting between different models classically has been performed by visually comparing the simulation results from different hypotheses to experimental results and choosing the simulations results that appear to most accurately emulate the experimental observations. Developing more quantitative metrics for parameter optimization and decision making will allow these processes to be outsourced to computer algorithms and will also improve academic reproducibility.

This thesis covers several aspects of the model development process for battery systems. The next three chapters of this thesis illustrate how mathematical models are built for batteries, and how they can incorporate various physical phenomena; they also provide additional evidence that mathematical models are essential to understanding the complex physical phenomena that occur in batteries. Chapters 2 and 3 develop crystal scale models for both the  $\text{Fe}_3\text{O}_4$  and  $\text{LiV}_3\text{O}_8$  systems, respectively. These crystal scale models are built upon in Chapter 4 by coupling the crystal scale physics to electrode scale phenomena. Chapter 5 provides insight into how computer algorithms can be applied to the model development process to perform physical parameter estimation as well as model selection and variable selection. In addition, Chapter 5 shows how mathematical models in conjunction with computer algorithms can be used to intelligently and quantitatively design experiments.

## 1.4 Bibliography

- [1] H. Chen, T. N. Cong, W. Yang, C. Tan, Y. Li, and Y. Ding, *Progress in Natural Science*, **19**(3), 291 (2009).
- [2] Z. Yang, J. Zhang, M. C. W. Kintner-Meyer, X. Lu, D. Choi, J. P. Lemmon, and J. Liu, *Chemical Reviews*, **111**, 3577 (2011).
- [3] Exxon Mobil, 2018 Outlook for Energy: A View to 2040, Technical report, Exxon Mobil (2018).
- [4] IEA (International Energy Agency), Global EV Outlook 2018: Towards cross-modal electrification, Technical report, International Energy Agency (2018).
- [5] J. Newman and W. Tiedemann, *AIChE Journal*, **21**(1), 25 (1975).
- [6] M. Doyle, T. F. Fuller, and J. Newman, *Journal of The Electrochemical Society*, **140**(6), 1526 (1993).
- [7] V. Ramadesigan, P. W. C. Northrop, S. De, S. Santhanagopalan, R. D. Braatz, and V. R. Subramanian, *Journal of the Electrochemical Society*, **159**(3), R31 (2012).
- [8] D. Silver, A. Huang, C. J. Maddison, A. Guez, L. Sifre, G. van den Driessche, J. Schrittwieser, I. Antonoglou, V. Panneershelvam, M. Lanctot, S. Dieleman, D. Grewe, J. Nham, N. Kalchbrenner, I. Sutskever, T. Lillicrap, M. Leach, K. Kavukcuoglu, T. Graepel, and D. Hassabis, *Nature*, **529**(7587), 484 (2016).
- [9] D. Silver, J. Schrittwieser, K. Simonyan, I. Antonoglou, A. Huang, A. Guez, T. Hubert, L. Baker, M. Lai, A. Bolton, Y. Chen, T. Lillicrap, F. Hui, L. Sifre, G. van den Driessche, T. Graepel, and D. Hassabis, *Nature*, **550**(7676), 354 (2017).
- [10] I. Androutsopoulos, J. Koutsias, K. V. Chandrinos, G. Paliouras, and C. D. Spyropoulos (2000).
- [11] C. D. Manning, C. D. Manning, and H. Schütze, *Foundations of statistical natural language processing*, MIT press (1999).

- [12] V. Venkatasubramanian, *AIChE Journal*, **55**(1), 2 (2009).
- [13] D. Beck, J. Pfaendtner, J. Carothers, and V. Subramanian, *Chemical Engineering Progress*, **113**(2), 21 (2017).
- [14] N. Dawson-Elli, S. B. Lee, M. Pathak, K. Mitra, and V. R. Subramanian, *Journal of The Electrochemical Society*, **165**(2), A1 (2018).

## Chapter 2

# Galvanostatic Interruption of Lithium Insertion into Magnetite: Evidence of Surface Layer Formation<sup>†</sup>

---

<sup>†</sup>This work has been published: Nicholas W. Brady, K. W. Knehr, Christina A. Cama, Christianna N. Lininger, Zhou Lin, Amy C. Marschilok, Kenneth J. Takeuchi, Esther S. Takeuchi, and Alan C. West. “Galvanostatic interruption of lithium insertion into magnetite: Evidence of surface layer formation.” *Journal of Power Sources* 321 (2016): 106-111.

The thesis writer’s contribution to this work was the model development and the analysis of the simulated results. The electrochemical observations were provided by C.A. Cama and Z. Lin from the Marschilok-Takeuchi Research Group at Stony Brook University.

## 2.1 Introduction

Nanostructuring of lithium-insertion materials may improve the performance of lithium-ion batteries by increasing the surface area to volume ratio and by lowering the solid-state diffusion resistances in the electrodes.<sup>1-9</sup> Increasing the surface area to volume ratio is beneficial because it provides more sites for the electrochemical reactions, thereby decreasing surface overpotential for a given nominal current density. However, extensive nanostructuring may have negative effects because it increases the amount of active material that can be exposed to side reactions and surface layer formation.<sup>10-12</sup> For instance, during the first cycle(s) of a lithium-ion battery, reactions between the electrolyte and the electrodes may result in the formation of thin layers of material on the electrode surfaces, commonly referred to as the solid electrolyte interphase (SEI) for graphite anodes and the cathode electrolyte interphase for cathodes.<sup>13-15</sup> The formation of these layers typically involves the transformation of active material into a surface layer, thereby reducing theoretical capacity.<sup>13</sup>

Herein, we compare simulations to experiments and hypothesize that the complex potential transients upon current interruption seen after a relatively small amount of lithium is inserted into magnetite ( $x = 0.5, 1.0, \text{ and } 1.5$  in  $\text{Li}_x\text{Fe}_3\text{O}_4$ ) is related to the formation of a thin layer of inactive material. In short, for small crystal sizes (6 and 8 nm) the potential initially increases due to relaxation of the concentration profile of reduced lithium, and then at longer times, decreases. Previous simulations capture the initial rise in potential caused by rearrangement of solid-state lithium<sup>16,17</sup>, but the fall in potential during relaxation cannot be explained. We hypothesize that it is caused by transformation of the active material ( $\text{Fe}_3\text{O}_4$ ) into inactive material. The transformation is confined to the crystal surface and occurs through a (as of yet unidentified) reaction, which increases the concentration of intercalated lithium in the remaining active material. The coupling of these effects – concentration profile relaxation by mass transport (rise) and increase of intercalated lithium (fall) – gives better experimental agreement. This chapter uses a previously described mass-transfer model and incorporates a mechanism for surface layer formation. The formation of the surface layer appears to occur via

nucleation and growth, which is qualitatively consistent with literature.<sup>18</sup> The Avrami model describes the formation of the surface layer.<sup>19–21</sup>

## 2.2 Experimental

Experiments were conducted using electrodes comprised of nanocrystalline magnetite. Small crystals, 6 and 8 nm average diameter, were synthesized using a coprecipitation method previously reported by the authors.<sup>8,22</sup> Larger crystals, ~32 nm (data not shown), were purchased from Alpha Aesar. Electrodes were prepared using 90% magnetite, 5% carbon, and 5% polyvinylidene fluoride binder (by weight) coated onto an aluminum foil substrate. Each electrochemical test was performed using a two-electrode coin-type experimental cell with a lithium metal anode and 1M LiPF<sub>6</sub> in 1:1 dimethyl carbonate: ethylene carbonate as the electrolyte. The electrodes had a nominal thickness of 50 μm and a nominal active mass loading of 4.1 mg cm<sup>-2</sup>.

Galvanostatic interruption experiments were conducted for electrodes comprised of nanocrystalline magnetite with average diameters of 6, 8 and 32 nm. The experimental cells were first lithiated at a C/200 rate (4.63 mA g<sup>-1</sup> of Fe<sub>3</sub>O<sub>4</sub>) to x = 0.5, 1.0, 1.5, and 2.0 electron equivalents per Fe<sub>3</sub>O<sub>4</sub> and then held at open circuit for up to 30 days. After the rest period, the cells were delithiated to a cutoff voltage of 3.0 V using a C/200 rate, followed by a constant voltage oxidation at 3.0 V for two hours. Subsequently, a second experiment was performed, where the current interruption was applied after the reduction of a specified amount of charge, which was equivalent to the amount of charge passed during the first lithiation.

In addition, second lithiation experiments were conducted at a rate of C/100 (9.26 mA g<sup>-1</sup> of Fe<sub>3</sub>O<sub>4</sub>) for electrodes made of 42.5% Fe<sub>3</sub>O<sub>4</sub>, 42.5% acetylene carbon black, and 15% polyvinylidene fluoride binder (PVDF) by weight. The magnetite was lithiated at the C/100 rate until a charge of 100 mAh g<sup>-1</sup> was passed. The magnetite was subsequently delithiated to a cut-off voltage of 3.0 V at the same C/100 rate and then held at 3.0 V for 1 hour, and lithiated again at C/100 to the same capacity, 100 mAh g<sup>-1</sup>.<sup>23</sup> All voltage

recovery experiments were conducted at 30°C using a freshly fabricated cell.

## 2.3 Theory

This section provides an outline of the present model, which was developed by modifying a previously validated multi-scale model to include the effects of the transformation of active material.<sup>16,17</sup> Table 1 contains a comparison of the governing equations for the two models. Consistent with multi-scale simulation results for 6 and 8 nm crystals, the present model assumes mass transport resistances only occur on the agglomerate length scale (i.e., no concentration variations within the crystals or across the bulk electrode). This assumption provides a valid approximation for the present experiments, where the focus is on understanding the complex voltage transients during the relaxation of electrodes comprised of crystals with diameters of 6 and 8 nm. The transport of lithium-ions in the agglomerate is simulated using dilute solution theory. The concentration of lithium-ions in the agglomerate is coupled to the concentration of solid-state lithium in the crystals through a Butler-Volmer kinetic expression. It is assumed that the formation of the surface layer has a negligible impact on the reaction kinetics. The thermodynamic potential as a function of lithium in the solid-state and in the agglomerate  $U(c_x, c_{agg})$  was modeled by fitting a modified Nernst equation to experimental data. The rate of change of solid-state lithium within the crystals,  $c_x$ , is calculated from the following material balance:

$$\frac{\partial(\epsilon_{active}c_x)}{\partial t} = \frac{ai_{rxn}}{F} \quad (2.1)$$

When held at the open circuit, the local current density  $i_{rxn}$  may not be zero because the crystals within the agglomerate galvanically interact until the concentration variations completely relax.  $\epsilon_{active}$  is the volume fraction of active material in the electrode. It is given by

$$\epsilon_{active} = (1 - \epsilon) \frac{V_{x,0} - \xi V_S}{V_{x,0}}, \quad V_{x,0} = \frac{4}{3}\pi r_x^3 \quad (2.2)$$

where  $\xi$  is the volume fraction of magnetite in the surface layer. For these simulations,  $\xi = 50\%$  and it is assumed that  $\epsilon = 0.26$ , consistent with closed packed spheroidal crystals. Other volume fractions  $\xi$  were explored, and they did not have a significant impact on the simulated results. Equations 2.1 and 2.2 were formulated assuming the transformation of magnetite to an inactive phase does not alter the total amount of solid-state lithium within the remaining magnetite. This implies that the local concentration of solid-state lithium within the active material increases as a result of the loss of active magnetite.

|                   | w/o $\text{Fe}_3\text{O}_4$ Transformation<br>(agglomerate-only)  | w/ $\text{Fe}_3\text{O}_4$ Transformation<br>(agglomerate-only)  |
|-------------------|---|--|
| Mass<br>(agg.)    | $\epsilon \frac{\partial c_{agg}}{\partial t} = \epsilon D_{agg} \frac{\partial^2 c_{agg}}{\partial r^2} + \frac{2\epsilon D_{agg}}{r} \frac{\partial c_{agg}}{\partial r} + \frac{ai_{rxn}}{F}$                    | No change  |
| Mass<br>(crystal) | $\epsilon_{active} \frac{\partial c_x}{\partial t} = -\frac{ai_{rxn}}{F}$<br>-  | $\frac{\partial(\epsilon_{active} c_x)}{\partial t} = -\frac{ai_{rxn}}{F}$<br>$\epsilon_{active} = (1 - \epsilon) \frac{V_{x,0} - \xi V_S}{V_{x,0}}$ |
| Reaction          | $i_{rxn} = i_0 \left[ \exp\left(\frac{\alpha_a F(V-U)}{R_G T}\right) - \exp\left(\frac{-\alpha_c F(V-U)}{R_G T}\right) \right]$<br>$i_0 = F k_{rxn} c_{agg}^{\alpha_a} c_x^{\alpha_c} (c_{x,max} - c_x)^{\alpha_a}$ | No Change<br>No Change   |

**Table 2.1:** Comparison of governing equations for model with and without transformation of  $\text{Fe}_3\text{O}_4$  to an inactive state due to reactions with the electrolyte.

## 2.4 Surface Layer Formation

The surface layer formation was initially modeled assuming a uniform, layer-by-layer growth. The results were able to capture some of the salient features of the OCP relaxation. However, better agreement was achieved by assuming a nucleation-and-growth mechanism, whereby the volume of the surface layer can be described through the Avrami model<sup>19-21</sup>:

$$V_S = V_{max,S} [1 - \exp(-k_S t^n)] \quad (2.3)$$

When the exponent  $n = 1$ , equation 2.3 is consistent with a layer-by-layer growth mechanism. More generally,  $n$  is determined by the relative rate of nucleation to growth and the dimensionality of the growth (e.g., two- vs. three-dimensional). The value of  $V_{max,S}$  is set by a final thickness of the surface layer:

$$V_{max,S} = \frac{4\pi}{3} (r_x^3 - (r_x - \lambda_{max})^3) \quad (2.4)$$

where  $\lambda_{max}$  is the maximum thickness of the surface layer, which was determined from the final measured open circuit potential.

Along with increasing the size of the crystals, the formation of the inactive layer is expected to increase the overall size of the agglomerate. In the present study, the agglomerate radius may, at most, increase by a factor of 7/6, which corresponds to a 1 nm thick surface layer forming on the 6 nm crystals (see below for further discussion on the model fitting of  $\lambda_{max} = 1$  nm). Simulations incorporating a 7/6 expansion of the agglomerate were conducted, but they did not have a significant impact on the simulated results. Therefore, the present model does not include the expansion of the agglomerate.

## 2.5 Salt Saturation Limit

During delithiation, the concentration of lithium salt within the pores of the agglomerate increases due to the slow mass transport processes. If the concentration exceeds the solubility limit of the salt, an additional solid-phase precipitates, and this plugs the pores and prevents the electrochemical reactions from occurring. To account for this process, the model includes the following conditional statement on the reaction current:

$$i_{rxn} = \begin{cases} i_{rxn}, & \text{if } c_{agg} < c_{sat} \\ 0, & \text{if } c_{agg} \geq c_{sat} \end{cases} \quad (2.5)$$

In equation 2.5,  $c_{agg}$  is the concentration of lithium salt in the agglomerate pores, and  $c_{sat}$  is the saturation concentration where the salt starts to precipitate. To the best of the authors knowledge, the exact value of  $c_{sat}$  for this system has not been published.

Therefore,  $c_{sat}$  was taken as a fitted parameter in the model. It was selected to ensure that the simulated delithiation reached the 3.0 V cutoff at the same time as the experiments.

Equations 2.2-2.4 along with the equations outlined in Table 1 were solved using a numerical algorithm outlined by Newman.<sup>24</sup> Physical properties were assumed to be the same as given in references 13, 14. In all cases, simulations were performed to be as consistent as possible with the experimental protocols. When the saturation limit was included in the model, the simulated and experimental charge passed prior to the cutoff voltage was in excellent agreement. To ensure a reasonable comparison between theory and experiment when the salt saturation limit was not included, the cells were oxidized at a rate of C/200 until an equivalent number of coulombs were passed. The simulations were then held at open-circuit for the remainder of the experimental oxidation time (see Figure 2.3). Continuous operation simulations followed the experimental protocol in ref. 19.

## 2.6 Results and Discussion

Figure 2.1 shows the experimental and simulated voltage during recovery after a lithiation at C/200 (4.63 mA g<sup>-1</sup>) until an average lithium concentration of  $x = 0.5$  (for  $x$  in  $\text{Li}_x\text{Fe}_3\text{O}_4$ ). The experimental voltage curve rises to a maximum after approximately 100 hours and appears to plateau. After 200 hours, the potential falls until it begins to reach a steady state at around 400 hours. The initial rise in voltage is explained by relaxation of concentration profiles within the agglomerate, and the subsequent decline in voltage is due to inactive layer formation. Qualitatively similar results are seen for 8-nm crystals, but no maximum is observed for the variation of the open circuit potential for 32-nm crystals.

The simulations in Figure 2.1 are based on the original model (no surface layer formation) as well as the modified model with surface layer formation. For each of the models with surface layer formation, the parameter  $k_S$  was adjusted to obtain the best fit. The agreement between experiment and simulation when  $n = 3$ , or  $n = 4$  is particularly

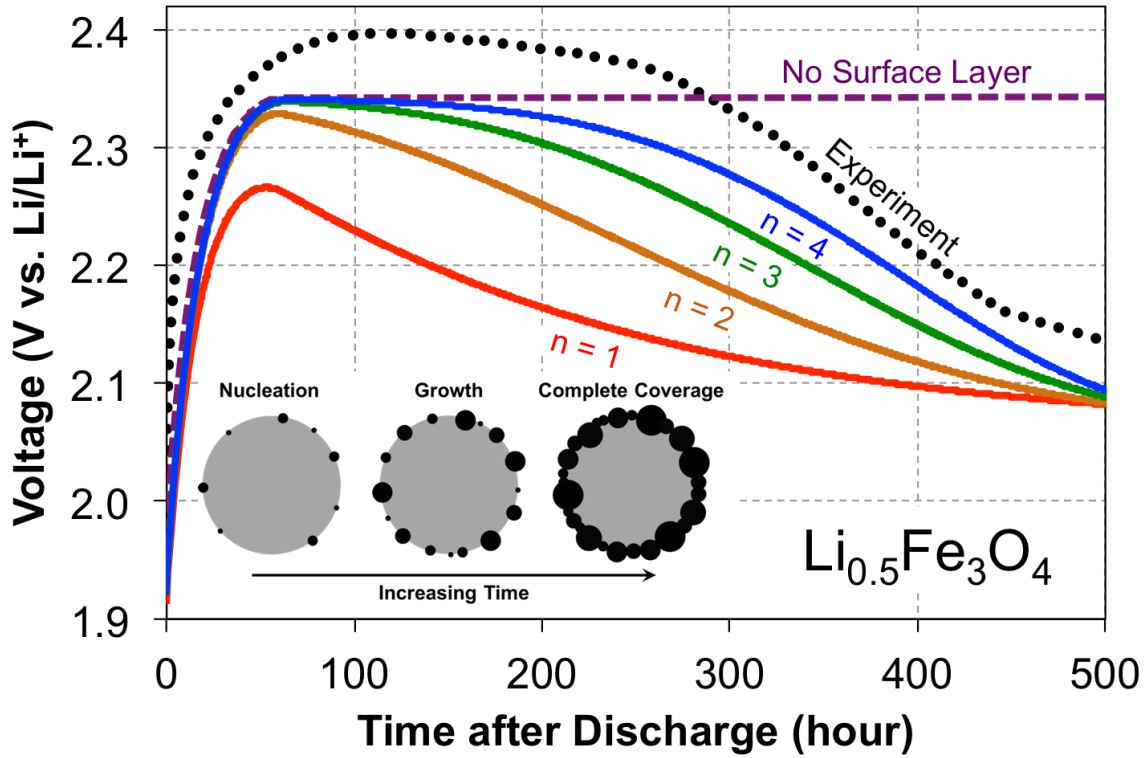


**Figure 2.1:** Voltage recovery for 6 nm  $\text{Fe}_3\text{O}_4$  electrodes that were initially lithiated to an average lithium concentration of  $\text{Li}_{0.5}\text{Fe}_3\text{O}_4$ . Simulations with surface layer formation were conducted using  $n = 1, 2, 3,$  or  $4$  in the Avrami equation (Eq. 2.3). Inset provides a visualization of the proposed mechanism of surface layer formation: progressive nucleation and three-dimensional growth ( $n = 4$ ).

compelling. The physical interpretation implies that the phase grows through a nucleation and growth process. However, it cannot be concluded definitively whether the nucleation is progressive or instantaneous or if the growth is two-dimensional or three-dimensional. It is assumed that surface layer growth terminates when magnetite is no longer in direct contact with electrolyte. The two parameters used to fit the model to experiment were  $k_S$  and  $\lambda_{max}$ , with  $k_S = 2.0 \times 10^{-25} \text{ s}^{-4}$  when  $n = 4$ , and  $\lambda_{max} = 1 \text{ nm}$ . The reported surface layer thickness is within the range reported in the literature for surface layers.<sup>10,13,25,26</sup>

Figure 2.2 shows a comparison of simulated ( $n = 4$ ) and measured transients for interruption after reduction to different levels of lithiation for 6 and 8 nm crystals. The initial drop in potential corresponds to insertion of lithium, and the initial rise indicates the beginning of recovery after current interruption. Comparisons are made without adjustment of the values of  $k_S$  and  $\lambda_{max}$ . In general, good agreement is observed between the simulations and experiments. Discrepancies may be attributed to changes in the

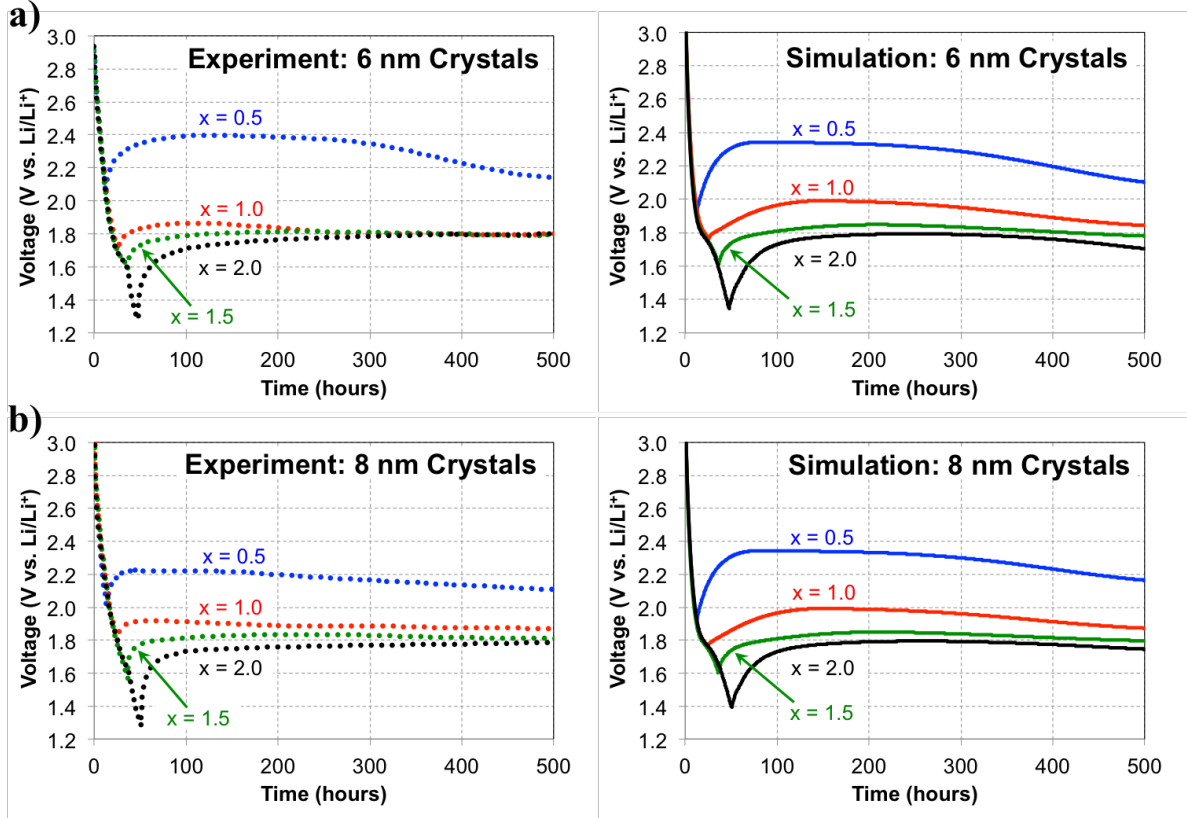


**Figure 2.2:** Side by side comparisons of experimental and simulated lithiation and voltage recovery for electrodes comprised of a) 6 nm and b) 8 nm crystals. Recovery was conducted after lithiation to different levels of intercalation (*i.e.*,  $x$  in  $\text{Li}_x\text{Fe}_3\text{O}_4$ ). Each experiment was conducted with a separate cell.

nucleation and growth kinetics at different depths of lithiation. For instance, inactive layer formation can be influenced by many factors including the cell potential and the lithiation time.<sup>27–29</sup> While a detailed analysis of the relationship between the kinetic parameters ( $k_S$  and  $\lambda_{max}$ ) and the operating conditions may be beneficial, it is currently out of scope with this work.

At higher degrees of lithiation (e.g.,  $x = 1.5$  and  $2.0$ ), both experimental and simulated results in Fig. 2 show no or very small maxima in the open circuit potential. The simulations suggest that the disappearance in the maximum is not because the surface layer is already fully formed. Instead, the maxima disappear because the open circuit potential does not change significantly in the range  $1.0 \leq x \leq 2.0$  (for  $x$  in  $\text{Li}_x\text{Fe}_3\text{O}_4$ ). This can be observed in Figure 5 of Ref. 13, which shows the fit of the open circuit voltage equation to experimental voltage recovery data. When simulations are extended to 32-nm crystals, the simulations correctly predict only small maxima with potential

(data not shown). This result is consistent with an assumption that the volume fraction transformed is proportional to the crystal surface area and that the surface layer thickness is the same for all crystal sizes. For instance, assuming that  $\lambda_{max}$  does not vary with crystal size, only a small percentage of the active material is transformed in the 32-nm crystals, which minimizes the increase in the solid-state lithium concentration. For example, the simulations indicate that a fully formed surface layer on a 32-nm crystal would only increase the concentration of solid-state lithium from  $x = 0.5$  to  $x \sim 0.55$ , which corresponds to a 33 mV change in voltage. This is a small variation when compared to the case with 6-nm crystals, where the concentration of solid-state lithium is predicted to increase by over 70% (from  $x = 0.5$  to  $x \sim 0.86$ , 270 mV).

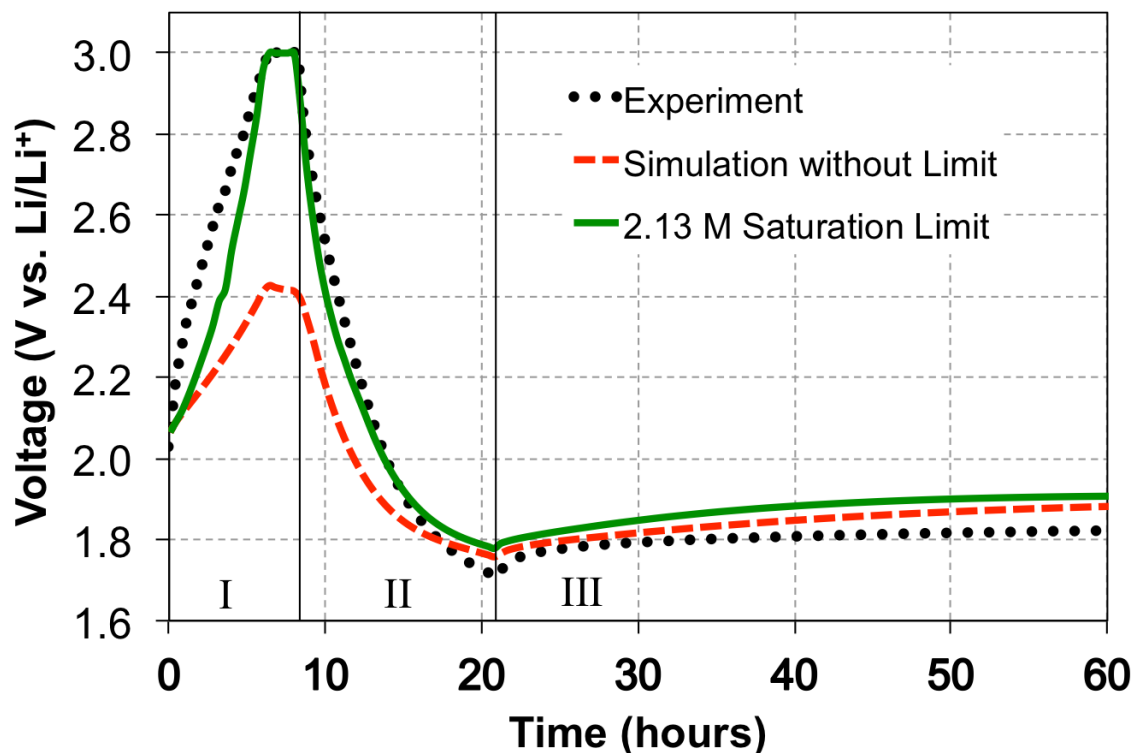


**Figure 2.3:** Experimental and simulated voltage during: I) first oxidation at C/200, then constant voltage hold at 3.0 V), II) second reduction at C/200, and III) second voltage recovery (open circuit). The first oxidation was conducted after a reduction to  $x = 0.5$  (for  $x$  in  $\text{Li}_x\text{Fe}_3\text{O}_4$ ) and an OCP relaxation for 30 days.

Another test of the hypothesis is to compare potential-time variation for the first and second reduction cycles. Figure 2.3 shows the experimental and simulated voltage curves for a cell that rested at open circuit for 30 days at a state of  $x = 0.5$  in  $\text{Li}_x\text{Fe}_3\text{O}_4$ .

Initially, the electrode was driven anodically to a cutoff voltage of 3.0 V. Next, the cell was held at 3.0 V for 2 hours. Coulometric analysis of the experimental data in Figure 2.3 show that  $x \sim 0.25$  at the end of oxidation. The cell was then lithiated to  $x \sim 0.75$  ( $0.25 + 0.50$ ), and allowed to relax. Simulations with and without a salt saturation limit show that including a solid-salt phase precipitation dramatically improves agreement with the experimental potential. Solid-salt precipitation is a factor because during the first voltage recovery solid-state lithium relaxes to a uniform concentration throughout the agglomerate. When the agglomerate is delithiated, poor mass transport through the agglomerate causes the concentration of oxidized lithium-ions in the pores to build up at the center of the agglomerate, eventually surpassing the saturation concentration.

Based on this analysis, delithiation of magnetite should be easier if the solid-state lithium does not redistribute toward the center of the agglomerate. This suggests that oxidation is less difficult if the electrode is operated continuously. For example, for magnetite reduced to an average concentration of  $x = 1.0$  (results not shown), simulations predict that  $\Delta x = -0.76$  (prior to a 3.0V cutoff) can be achieved by delithiation at a constant rate of  $C/100$  (experimental value is  $\Delta x = -0.78$ ) if the oxidation current is applied immediately after the reduction reaction. However, if the electrode rests at OCP for 30-days prior to the oxidation reaction, simulations predict  $\Delta x = -0.5$ , in accord with the experimental value of  $\Delta x = -0.55$  electron equivalents.

Further evidence that the surface layer reduces capacity can be seen from an analysis of the first and second lithiation processes of the galvanostatic interruption experiments, *c.f.* Figures 2.2 and 2.3. For instance, experiments show a reduction in specific energy between the first and second lithiation processes of 14%, 11%, and 11% for cells lithiated to  $x = 0.5$ , 1.0, and 1.5 respectively, whereby  $x$  corresponds to the change of lithiation. The specific energy was determined by integrating the power vs. time curves. Simulations of these experimental studies that account for surface-layer formation are in accord with experiments (predicted reduction of specific energies of 11%, 9%, and 16%, respectively). Simulations without the surface layer formation predicted specific-energy reductions of 3%, 1%, and 2%, with the reductions arising from an incomplete delithiation during the

charging protocol. While the present simulations incorporating surface-layer formation are in fair agreement with experiments, a more complex model may be able to capture the impact of potential-time history on the surface layer, possibly leading to improvements in the predictions.

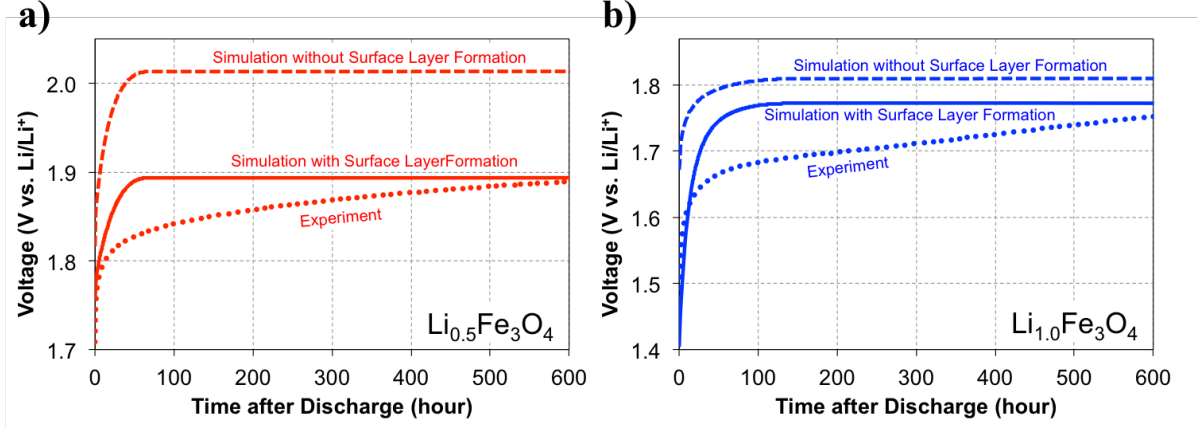


**Figure 2.4:** Experiments and simulations of the second voltage recovery with simulations accounting for (solid) and not accounting for (dashed) active material transformation. Comparisons are made for a)  $x = 0.5$  and b)  $x = 1.0$  in  $\text{Li}_x\text{Fe}_3\text{O}_4$ .

Figure 2.4 shows the experimental and simulated voltage recovery (*cf.*, zone III of Figure 2.3), for  $x = 0.5$  and for  $x = 1.0$ . When the impact of inactive layer formation is included, the simulations of the potential recovery after the second lithiation step are in much better agreement with the final OCP. However, the simulations predict a more rapid transition to the steady-state OCP than is seen experimentally. It appears as if the diffusion coefficient is lower after the formation of the surface layer on the magnetite. One explanation is that the surface mobility of lithium on the new surface is significantly decreased, as this is believed to impact the agglomerate-scale diffusion coefficient.

Figure 2.5 summarizes the impact of nanosizing magnetite on electrode capacity. Assuming that a 0.5 nm layer of magnetite is transformed into a surface layer, the fraction of active material lost decreases rapidly with increasing crystal size. However, depending on lithiation rates and transport resistances, large crystal sizes result in a significant fraction of the magnetite not being used prior to the lithiation cutoff potential. To illustrate this effect, we have simulated performance of a hypothetical magnetite electrode with varying crystal sizes and varying insertion rate. The battery is hypothetical because it is

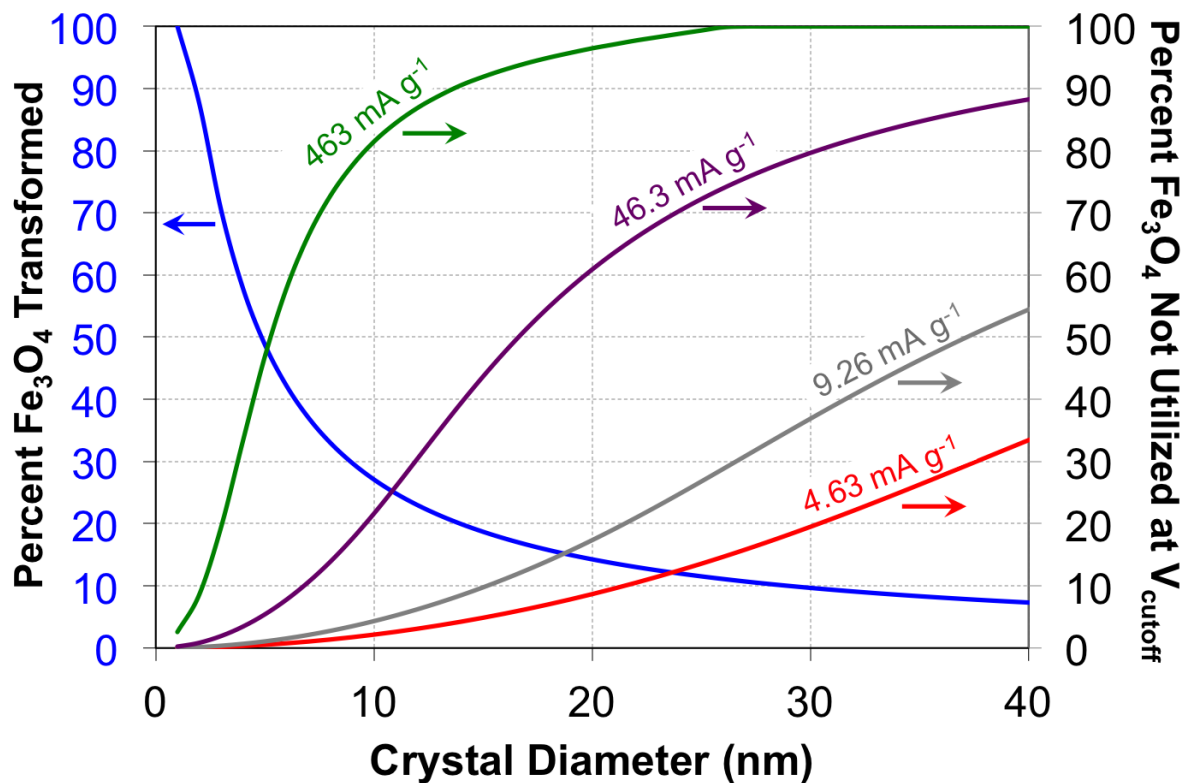


**Figure 2.5:** Plot comparing the active material lost (not utilized) due to transformation (left-axis) and active material not utilized due to solid-state transport resistances (right-axis).

assumed that it has been fabricated in such a manner that the only transport resistance in the battery is the solid-state diffusion in the crystal. Presently, as constructed, agglomerate scale diffusion is another significant resistance within the magnetite electrodes.<sup>16,17</sup> Simulations were conducted using dilute solution theory with  $D_x = 2.0 \times 10^{-18} \text{ cm}^2 \text{ s}^{-1}$ , and a cutoff voltage of 1.5 V.

Results, shown for four lithiation rates, illustrate that the fraction of unused magnetite increases as crystal radius increases. Clearly, the trend is the opposite for the fraction of magnetite transformed by surface layer formation. The results summarized in Figure 2.5 are hypothetical because they assume agglomerate-free electrode construct and cannot be quantitatively compared to experiments. Depending on the application, an optimal crystal size may exist, where performance may even decline if the crystal is made too small. While the above asserts that inactive layer formation may have a negative effect on capacity for nanoparticles, it is well documented that SEIs (a type of surface layer) have an important role in improving stability, cyclability, rate capability,

and safety in lithium ion batteries.<sup>13,14,30–35</sup>

At present, the precise composition and structure of the surface layer identified in this work are unknown. The surface layer may correspond to the transformation of magnetite to a different, less reversible phase. It may also correspond to the formation of an SEI on the magnetite surface, similar to that observed by Lee *et al.* for 10 to 12-nm crystals.<sup>36</sup> Either way, the simulated results suggest that a portion of the active material is lost, which reduces the capacity of the material.

## 2.7 Conclusions

Magnetite reacts with electrolyte to form a surface layer, and when the magnetite is made nanocrystalline, a significant fraction of the active material may be transformed. It is suggested by the open-circuit potential relaxation that during surface layer formation, the intercalated lithium is concentrated in the remaining magnetite. Comparisons of simulations to experiments suggest that the surface layer formation can be described by a nucleation and growth mechanism. Agreement with experimental oxidation data can be improved by accounting for a saturation- induced solid-salt formation within the pores of the agglomerate. The process of surface layer formation is very complicated. This particular system allowed for insights into the formation process, but it is unclear if the methods outlined here can be extended to other chemistries.

## 2.8 Acknowledgements

This work was supported as part of the Center for Mesoscale Transport Properties, an Energy Frontier Research Center supported by the U. S. Department of Energy, Office of Science, Basic Energy Sciences, under award #DE-SC0012673. The computing was performed on the Yeti Shared HPC Cluster at Columbia University, which includes support from Empire State Developments Division of Science, Technology, and Innovation under contract number C090171.

## 2.9 List of Symbols

|                     |   |                                   |
|---------------------|---|-----------------------------------|
| $a$                 | specific surface area                                 | ( $\text{cm}^2 \text{ cm}^{-3}$ ) |
| $c_{agg}$           | lithium concentration in the agglomerate              | ( $\text{mol cm}^{-3}$ )          |
| $c_{sat}$           | saturation limit of lithium salt in the electrolyte   | ( $\text{mol cm}^{-3}$ )          |
| $c_x$               | solid-state lithium concentration                     | ( $\text{mol cm}^{-3}$ )          |
| $D_x$               | solid-state diffusion coefficient                     | ( $\text{cm}^2 \text{ s}^{-1}$ )  |
| $F$                 | Faradays constant                                     | (96,485 C mol <sup>-1</sup> )     |
| $i_{rxn}$           | reaction rate   | (A cm <sup>-2</sup> )             |
| $k_S$               | reaction rate constant of the surface layer formation | (s <sup>-4</sup> )                |
| $n$                 | denotes mode of nucleation and growth                 | (-)                               |
| $r_x$               | crystal radius  | (cm)                              |
| $t$                 | time  | (s)                               |
| $V_{agg}$           | agglomerate volume                                    | (cm <sup>3</sup> )                |
| $V_x$               | crystal volume  | (cm <sup>3</sup> )                |
| $V_S$               | surface layer volume                                  | (cm <sup>3</sup> )                |
| $V_{max,S}$         | maximum surface layer volume                          | (cm <sup>3</sup> )                |
| $\epsilon_{active}$ | volume fraction of active material                    | (-)                               |
| $\lambda_{max}$     | maximum surface layer thickness                       | (cm)                              |
| $\xi$               | volume fraction of magnetite in the surface layer     | (-)                               |

### Subscript

|       |                     |
|-------|---------------------|
| $agg$ | denotes agglomerate |
| $x$   | denotes crystal     |
| $S$   | denotes surface     |

## 2.10 Bibliography

- [1] S. Mitra, P. Poizot, A. Finke, and J. M. Tarascon, *Advanced Functional Materials*, **16**(17), 2281 (2006).
- [2] Vikram Sivakumar, Sundeep Kumar, Caroline A. Ross and Y. Shao-Horn, *IEEE Transactions on Magnetism*, **43**(6), 3121 (2007).
- [3] Z.-m. Cui, L.-y. Jiang, W.-g. Song, and Y.-g. Guo, *Chemistry of Materials*, **21**(6), 1162 (2009).
- [4] S. Komaba, T. Mikumo, and A. Ogata, *Electrochemistry Communications*, **10**(9), 1276 (2008).
- [5] S. Komaba, T. Mikumo, N. Yabuuchi, A. Ogata, H. Yoshida, and Y. Yamada, *Journal of The Electrochemical Society*, **157**(1), A60 (2010).
- [6] M. C. Menard, A. C. Marschilok, K. J. Takeuchi, and E. S. Takeuchi, *Electrochimica Acta*, **94**, 320 (2013).
- [7] M. C. Menard, K. J. Takeuchi, A. C. Marschilok, and E. S. Takeuchi, *Physical chemistry chemical physics : PCCP*, **15**(42), 18539 (2013).
- [8] S. Zhu, A. C. Marschilok, E. S. Takeuchi, G. T. Yee, G. Wang, and K. J. Takeuchi, *Journal of The Electrochemical Society*, **157**(11), A1158 (2010).
- [9] S. Zhu, A. C. Marschilok, C.-Y. Lee, E. S. Takeuchi, and K. J. Takeuchi, *Electrochemical and Solid-State Letters*, **13**(8), A98 (2010).
- [10] R. A. Ali-zade, *Inorganic Materials*, **42**(11), 1215 (2006).
- [11] R. Chantrell, J. Popplewell, and S. Charles, *IEEE Transactions on Magnetism*, **14**(5), 975 (1978).
- [12] R. Kaiser and G. Miskolczy, *Journal of Applied Physics*, **41**(3), 1064 (1970).
- [13] P. Verma, P. Maire, and P. Novák, *Electrochimica Acta*, **55**(22), 6332 (2010).

- [14] Y. Wang and P. B. Balbuena, in *Lithium-Ion Batteries: Solid-Electrolyte Interphase*, chapter Chapter 5, p. 227–275, Imperial College Press, London (2003).
- [15] R. Fong, U. von Sacken, and J. R. Dahn, *Journal of The Electrochemical Society*, **137**(7), 2009 (1990).
- [16] K. W. Knehr, N. W. Brady, C. N. Lininger, C. A. Cama, D. C. Bock, Z. Lin, A. C. Marschilok, K. J. Takeuchi, E. S. Takeuchi, and A. C. West, *ECS Transactions*, **69**(1), 7 (2015).
- [17] K. W. Knehr, N. W. Brady, C. A. Cama, D. C. Bock, Z. Lin, C. N. Lininger, A. C. Marschilok, K. J. Takeuchi, E. S. Takeuchi, and A. C. West, *Journal of The Electrochemical Society*, **162**(14), A2817 (2015).
- [18] R. N. Methekar, P. W. C. Northrop, K. Chen, R. D. Braatz, and V. R. Subramanian, *Journal of The Electrochemical Society*, **158**(4), A363 (2011).
- [19] M. Avrami, *The Journal of Chemical Physics*, **7**, 1103 (1939).
- [20] M. Avrami, *The Journal of Chemical Physics*, **8**, 212 (1940).
- [21] M. Avrami, *Journal of Chemical Physics*, **9**, 177 (1941).
- [22] S. Zhu, A. C. Marschilok, E. S. Takeuchi, and K. J. Takeuchi, *Electrochemical and Solid-State Letters*, **12**(4), A91 (2009).
- [23] D. C. Bock, K. C. Kirshenbaum, J. Wang, W. Zhang, F. Wang, J. Wang, A. C. Marschilok, K. J. Takeuchi, and E. S. Takeuchi, *ACS Applied Materials & Interfaces*, **7**(24), 13457 (2015).
- [24] J. Newman and K. E. Thomas-Alyea, *Electrochemical Systems*, John Wiley & Sons Inc., Hoboken, New Jersey, 3rd edition (2004).
- [25] D. Aurbach, *Journal of Power Sources*, **89**, 206 (2000).
- [26] T. Yoshida, M. Takahashi, S. Morikawa, C. Ihara, H. Katsukawa, T. Shiratsuchi, and J.-i. Yamaki, *Journal of The Electrochemical Society*, **153**(3), A576 (2006).

- [27] D. Aurbach, *Journal of The Electrochemical Society*, **143**(12), 3809 (1996).
- [28] E. Peled, *Journal of The Electrochemical Society*, **145**(10), 3482 (1998).
- [29] J. Li, E. Murphy, J. Winnick, and P. A. Kohl, *Journal of Power Sources*, **102**, 302 (2001).
- [30] J. Xu, Y. Hu, T. Liu, and X. Wu, *Nano Energy*, **5**, 67 (2014).
- [31] X. Wu, J. Guo, M. J. McDonald, S. Li, B. Xu, and Y. Yang, *Electrochimica Acta*, **163**, 93 (2015).
- [32] Z. Zhang, D. Fouchard, and J. Rea, *Journal of Power Sources*, **70**, 16 (1998).
- [33] G. Park, H. Nakamura, Y. Lee, and M. Yoshio, *Journal of Power Sources*, **189**, 602 (2009).
- [34] Y. Zheng, Y. B. He, K. Qian, B. Li, X. Wang, J. Li, S. W. Chiang, C. Miao, F. Kang, and J. Zhang, *Electrochimica Acta*, **176**, 270 (2015).
- [35] M. Matsui, K. Dokko, Y. Akita, H. Munakata, and K. Kanamura, *Journal of Power Sources*, **210**, 60 (2012).
- [36] S. H. Lee, S.-H. Yu, J. E. Lee, A. Jin, D. J. Lee, N. Lee, H. Jo, K. Shin, T.-Y. Ahn, Y.-W. Kim, H. Choe, Y.-E. Sung, and T. Hyeon, *ACS Nano Letters*, **13**, 4249 (2013).

# Chapter 3

## Discharge, Relaxation, and Charge Model for the Lithium Trivanadate Electrode: Reactions, Phase Change, and Transport<sup>‡</sup>

---

<sup>‡</sup>This work has been published: Nicholas W. Brady, Qing Zhang, K. W. Knehr, Ping Liu, Amy C. Marschilok, Kenneth J. Takeuchi, Esther S. Takeuchi, and Alan C. West. “Discharge, Relaxation, and Charge Model for the Lithium Trivanadate Electrode: Reactions, Phase Change, and Transport.” *Journal of The Electrochemical Society* 163, no. 14 (2016): A2890-A2898.

The thesis writer’s contribution to this work was the model development and the analysis of the simulated results. The electrochemical observations and microscopy images were provided by Qing Zhang from the Marschilok-Takeuchi Research Group at Stony Brook University. The density function theory analysis was provided by Ping Liu from Brookhaven National Laboratory.

## 3.1 Introduction

Large scale transportation and stationary applications of lithium ion batteries require inexpensive, reliable, and safe systems.<sup>1</sup> Transition metal (cobalt, iron, nickel, manganese, vanadium, titanium, tungsten, and molybdenum) oxides are attractive lithium intercalation cathode materials for these applications because of their natural abundance and high redox potentials.<sup>2</sup> Conventional anode materials, such as graphite, typically have higher specific capacities than cathode materials, such as  $\text{LiCoO}_2$  and  $\text{LiFePO}_4$ . This difference in capacity is because typical cathode materials can only accept one lithium per formula unit; therefore there is potential breakthrough in developing cathode materials that are able to host lithium-ions in excess of one per formula unit. For example,  $\text{LiV}_3\text{O}_8$  is an attractive material because of its high potential suitable for battery applications ( $\sim 3\text{V}$ ) and high theoretical specific energy ( $\sim 374 \text{ mAh g}^{-1}$ ).<sup>3-5</sup> The high capacity comes from the ability of the matrix to host three additional (excess) lithium ions ( $\text{Li}_4\text{V}_3\text{O}_8$ ).<sup>6</sup>

Because  $\text{LiV}_3\text{O}_8$  is a promising mid-voltage material with high capacity and good cycling ability, it has received research attention. However, despite this attention, important physical parameters such as the diffusion coefficient of lithium in the material are not known with precision, varying by at least two orders of magnitude.<sup>7,8</sup> In addition, the material undergoes a phase change at  $\sim 2.5 \text{ V}$  from  $\text{Li}_{1+x}\text{V}_3\text{O}_8$  to  $\text{Li}_4\text{V}_3\text{O}_8$ ,<sup>6,9,10</sup> but the equilibrium composition, specifically in the lithium-deficient phase is not known with precision<sup>11</sup> and, to the authors knowledge, there are no studies on the kinetics of phase change in this material.

Through the development of a continuum model, this chapter seeks to quantify the diffusion coefficient as well as the parameters governing phase change in lithium trivanadate. In other materials, several models have been proposed to account for phase change, including shrinking-core, mosaic, domino-cascade, and core-shell models.<sup>12-15</sup> The shrinking-core model is the most commonly used model because it gives good agreement with electrochemical measurements, it is intuitive, and numerically robust. Conceptually, this method is limited because it generally assumes instantaneous phase transformation kinetics. Because we seek to quantify the phase change kinetics, the shrinking-core

method is of little use.

In order to quantify the kinetics of the phase transition, this chapter develops a model which accounts for lithium diffusion and phase change reaction as parallel processes. Depending on parameter values, this model can replicate a shrinking-core model, yet it is easier to implement. The model retains the main advantages of the shrinking-core model: agreement with electrochemical measurements, intuitive, numerically robust, and has the added advantage that it does not require the tracking of moving interior boundaries. This model utilizes the Avrami treatment of nucleation and growth to describe phase change.<sup>16-18</sup> While a description of nucleation and growth has been used previously to describe phase change in battery materials,<sup>19,20</sup> this work is the first to validate a continuum model using Avrami kinetics against electrochemical measurements taken during discharge, charge, and relaxation.

## 3.2 Experimental

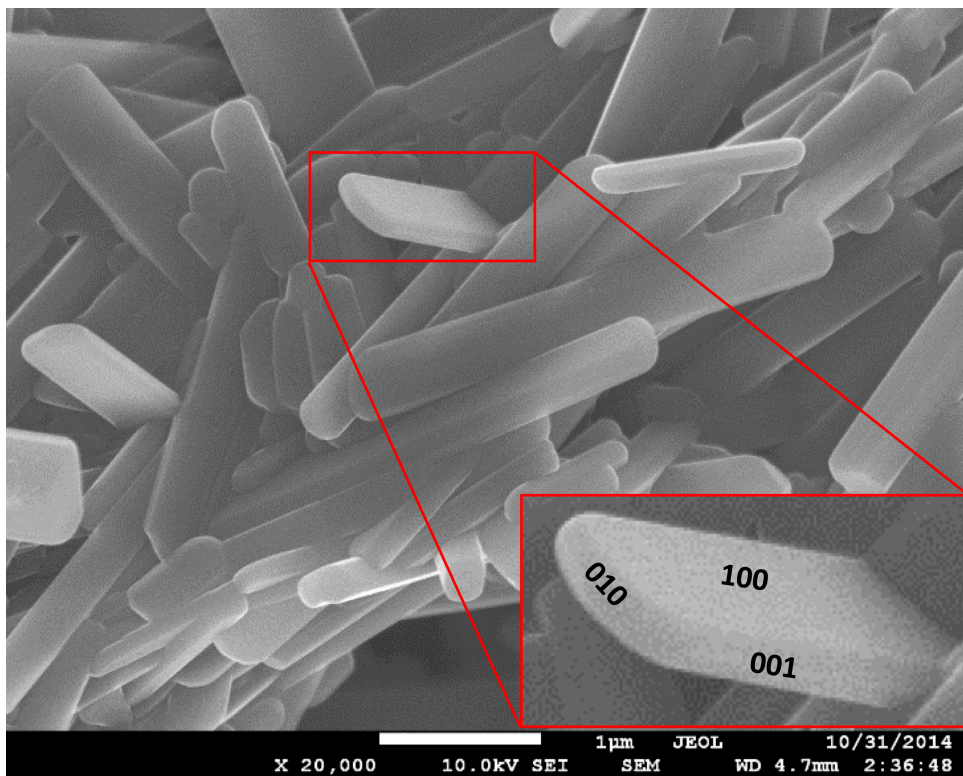


**Figure 3.1:** SEM images of  $\text{LiV}_3\text{O}_8$  crystals sintered at  $550^\circ\text{C}$  for 2 hours. The inset highlights a representative crystal with the three faces labeled with their respective planes.

### 3.2.1 Materials Synthesis and Characterization

$\text{Li}_{1.1}\text{V}_3\text{O}_8$  materials were prepared via a sol-gel approach.<sup>21</sup> Briefly,  $\text{LiOH}\cdot\text{H}_2\text{O}$  and  $\text{V}_2\text{O}_5$  in a stoichiometric ratio of  $\text{Li}:\text{V}=1.1:3$  were used as starting materials and stirred in 50 °C aqueous solution under  $\text{N}_2$  atmosphere for 24 h followed by freeze-drying. The precursor materials were heat-treated at 550 °C to get the final product. SEM images were taken with an accelerating voltage of 10 kV on a JEOL 7600F Field Emission Scanning Electron Microscopy at the Center of Functional Nanomaterials at Brookhaven National Laboratory.

### 3.2.2 Electrochemical Measurements

$\text{Li}_{1.1}\text{V}_3\text{O}_8$  cathodes were prepared by mixing  $\text{Li}_{1.1}\text{V}_3\text{O}_8$  powders, carbon, graphite and polyvinylidene fluoride in N-Methyl-2-pyrrolidone solution and the slurry was cast onto Al foil. Coin cells were assembled in an Argon-filled glovebox with lithium-metal as the anode and 1M  $\text{LiPF}_6$  EC (ethylene carbonate)/DMC (dimethyl carbonate) (volume ratio 3:7) as electrolyte. Galvanostatic cycling tests were carried out on Maccor Battery Test Equipment at C/10 to 1.9 electron equivalents or at C/5, C/2 and 1C rate to 2.4 V.

### 3.2.3 Ab-Initio Theory Calculations

DFT calculations were performed within the Generalized Gradient Approximation (GGA) using the PW91<sup>22</sup> pseudo-potential as implemented in VASP.<sup>23</sup> A +U correction term was used for vanadium, 3.1 eV, cited from fitting enthalpy of formation for binary oxides.<sup>24</sup>  $\text{LiV}_3\text{O}_8$  surfaces were modeled by two  $\text{Li}_4\text{V}_{12}\text{O}_{32}$  layers, where the bottom  $\text{Li}_4\text{V}_{12}\text{O}_{32}$  layers in the unit cell was fixed in their optimized bulk positions while the top layer was allowed to relax. The Brillouin-zone integration was performed on a grid of  $2\times 3\times 1$  Monkhorst-Pack<sup>25</sup> special k-points. A vacuum layer of 20 Å thick was applied perpendicular to the slab to avoid artificial interactions between the slab and its periodic images.

### 3.2.4 Experimental Results

From the SEM images of the synthesized  $\text{LiV}_3\text{O}_8$  crystals, the particle dimensions were measured using ImageJ software. Measuring many of these crystals gives order of magnitude estimations for the dimensions: 10 - 100 nm, 1000 nm, 100 nm for the [100], [010], and [001] directions respectively.

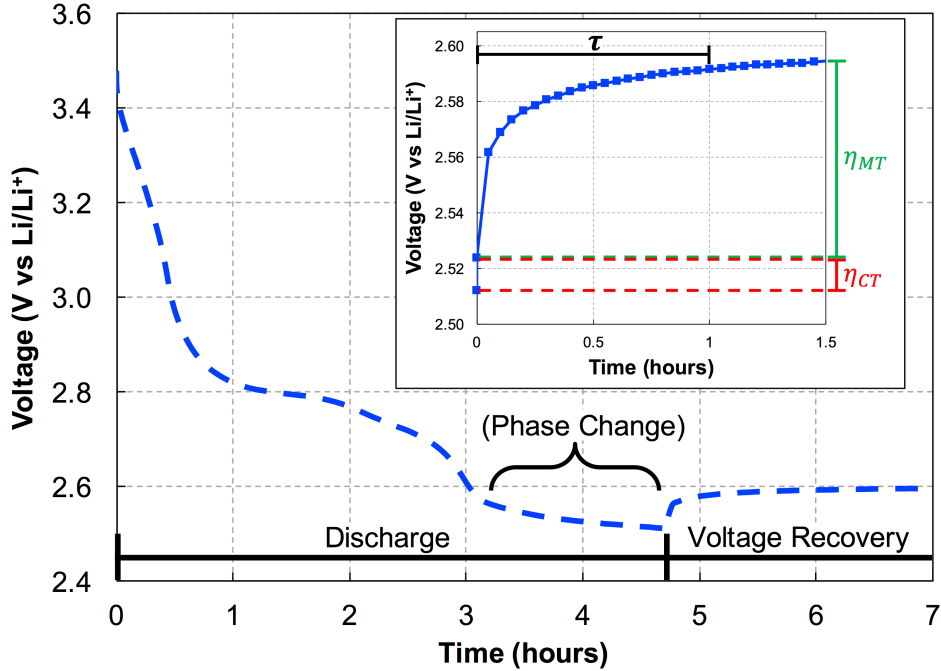


**Figure 3.2:** Representative potential curve during discharge and recovery. The constant voltage plateau seen during the discharge indicates a two-phase region. The voltage recovery (inset) is divided into charge-transfer losses ( $\eta_{CT}$ ) and mass-transfer losses ( $\eta_{MT}$ ). The characteristic relaxation time,  $\tau$ , is also determined from the voltage recovery data.

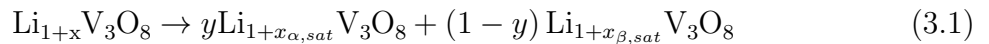
Figure 2 is a discharge curve conducted at a C/10 current rate (37.49 mA g<sup>-1</sup>) to a depth of  $x = 1.9$  in  $\text{Li}_{1+x}\text{V}_3\text{O}_8$  (176.82 mAh g<sup>-1</sup>). The voltage plateau at about 2.5 V suggests a two-phase region, as has been documented previously.<sup>6,9,10</sup> At the end of discharge, the current is interrupted and voltage recovery is measured. The recovered voltage is composed of a charge-transfer overpotential,  $\eta_{CT}$ , and a mass-transfer overpotential,  $\eta_{MT}$ , associated with non-uniformities of the solid-state lithium concentration within the crystal. It is seen that the charge-transfer losses recover nearly instantaneously, while the mass-transfer overpotential relaxes over longer time periods (on the order of an hour). It is important to understand on which length scales these mass-transfer losses are occurring because it informs us which processes are performance limiting, from which we can im-

prove electrode design. Using the bulk electrode thickness and bulk diffusion coefficient, relaxation is expected to occur on the order of a minute,  $\tau = \frac{L^2}{D} = \frac{(0.005 \text{ cm})^2}{(10^{-6} \text{ cm}^2 \text{ s}^{-1})} = 25 \text{ s}$ . This suggests that mass-transport within the electrolyte is not performance limiting.

The  $\text{LiV}_3\text{O}_8$  crystal has a layered structure,<sup>8,11</sup> where intralayer transport of lithium, along the [010] and [001] directions, is preferred over interlayer transport, the [100] direction.<sup>26,27</sup> Assuming that transport in the [100] direction is negligible compared to transport in the other directions, and assuming that rates of transport in the [010] and [001] directions are approximately equal, it is hypothesized that diffusion in the [001] direction is performance limiting. Using the crystal thickness in the [001] direction and the solid-state diffusion coefficient, we expect the characteristic diffusion time (relaxation time) to be on the order of an hour,  $\tau = \frac{L^2}{D} = \frac{(0.005 \text{ nm})^2}{(10^{-13} \text{ cm}^2 \text{ s}^{-1})} = 1000 \text{ s}$ . Although Figure 1 shows that the crystals agglomerate, the dimensional analysis suggests that mass transfer losses are dominated by diffusion resistances on the crystal scale. To further test this hypothesis a mathematical model was developed.

### 3.3 Theory

A qualitative comparison of the shrinking-core and nucleation and growth models is given in Figure 3. For both formulations, lithium inserts into the active material, and below a threshold concentration,  $c_{\alpha, \text{sat}}$ , there is no phase change. However once the local concentration of lithium in the  $\alpha$ -phase exceeds  $c_{\alpha, \text{sat}}$ , the material phase separates into a lithium-deficient  $\alpha$ -phase and a lithium-rich  $\beta$ -phase as follows:



At equilibrium, the molar ratio of  $\alpha$ -phase to  $\beta$ -phase can be calculated:

$$y = \frac{x_{\beta, \text{sat}} - x}{x_{\beta, \text{sat}} - x_{\alpha, \text{sat}}}; \quad x_{\alpha, \text{sat}} < x < x_{\beta, \text{sat}} \quad (3.2)$$

Following the development outlined by Knehr et al.<sup>28,29</sup> the hypothesis of phase formation was further explored by developing a nucleation and growth model on the

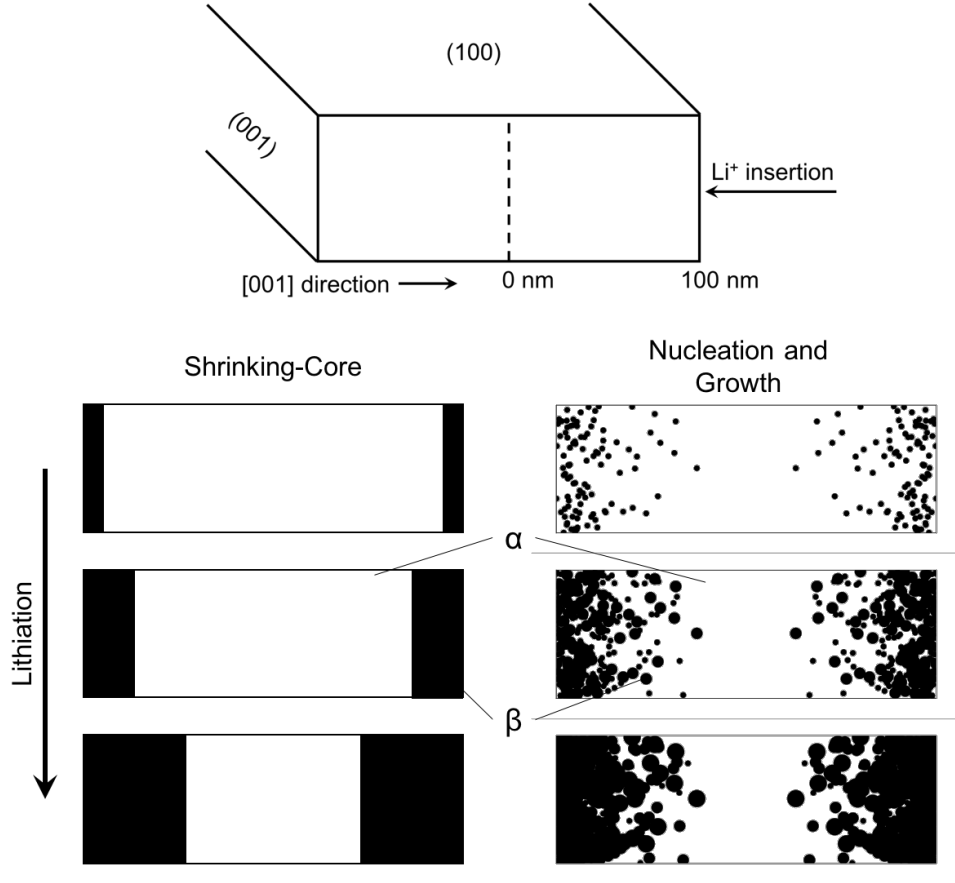


**Figure 3.3:** (Top) Schematic of the modeling domain. It is assumed that  $\text{Li}^+$  predominantly inserts through the (001) crystal face and therefore concentration variations only occur along the [001] direction. (Bottom) Qualitative representations of two models for phase-change are compared: the commonly utilized shrinking-core method and the nucleation and growth model. As lithium is inserted into the material, the concentration of lithium increases. Once the concentration of lithium exceeds the saturation value, phase change commences, and a new lithium rich  $\beta$ -phase is created. As more lithium is inserted, the amount of  $\beta$ -phase increases. The shrinking-core method assumes that the new phase forms in a layer by layer process, while the nucleation and growth model produces a profile that is similar, but with a more dispersed  $\beta$ -phase.

crystal scale with the following assumptions:

1. The system is isothermal
2. Dilute solution theory is applicable to describe solid-state transport
3. Variations in concentration and potential on the bulk electrode scale and agglomerate scale are negligible.
4. The  $\text{LiV}_3\text{O}_8$  crystals are considered to be rectangular prisms and have a constant volume.
5. The polarization associated with the lithium-metal negative electrode is negligible.

6. Only the  $\alpha$ -phase is electrochemically active. Lithium can only enter the  $\beta$ -phase by first inserting into the  $\alpha$ -phase, and then through a chemical reaction, enter into the  $\beta$ -phase.
7. Mass-transfer along the [001] direction is assumed to be rate limiting and concentration variations in the [100] and [010] directions are negligible.

Assumption 7 is informed from an analysis of the materials crystal structure and DFT calculations. The spacing between vanadate layers is about 6.36 Å, while the atoms within a vanadate layer are more close-packed.<sup>30,31</sup> This crystal structure indicates lithium transport is anisotropic: diffusion is favored in directions parallel to the vanadate plane ([010] and [001]) and hindered in the direction normal to the plane, [100]. Using the diffusive activation energies calculated in Ref. 27 (0.61 eV: 0.36 eV: 0.36 eV for the directions [100]:[010]:[001]), and the crystal aspect ratios obtained from the SEM image (Figure 1), it would be concluded that the mass flow (flux multiplied by area of appropriate face) rates in the [100] and [001] directions may be approximately equal. Furthermore, grain boundaries might also be a more significant transport route along the shorter distance perpendicular to the [100] plane.

However, DFT calculations suggest that the adsorption and diffusion of  $\text{Li}^+$  are preferential on the (001) surface via the unique tunnel along the [001] direction. The tunnel is constructed along the zig-zag  $\text{VO}_x$  plane, which provides highly symmetric oxygen sites for  $\text{Li}^+$  adsorption and diffusion. The (001) face provides a  $\text{Li}^+$  binding energy of -0.56 eV; accordingly, the (001) face can be anticipated to be active during lithiation. In contrast, on the (010) face, lithiation is hindered by a weakened  $\text{Li}^+$  adsorption with a binding energy of -0.08 eV, which likely results in a lower coverage. The (100) face is the most inert face during lithiation, providing an adsorptive binding energy of 0.40 eV. Charge-transfer on the (100) face may be hindered by an unfavorable binding energy, essentially rendering the (100) face an insulator during lithiation. These factors indicate that the mass-transport process can be approximated as one-directional along the [001] direction.

The description of the lithium insertion is given by equation 3.3.



where  $\Gamma$  and  $\text{Li}\Gamma$  are unoccupied and occupied host sites in the crystal ( $\Gamma = \alpha\text{-LiV}_3\text{O}_8$ ).

The charge-transfer kinetics of this reaction are estimated using the Butler-Volmer kinetic expression, equations 3.4 and 3.5.

$$i = i_0 \left[ \exp\left(\frac{\alpha_a F \eta}{R_G T}\right) - \exp\left(-\frac{\alpha_c F \eta}{R_G T}\right) \right] \quad (3.4)$$

$$i_0 = F k_{rxn} c_0^{\alpha_a} c_\alpha^{\alpha_c} (c_{\alpha, max} - c_\alpha)^{\alpha_a} \quad (3.5)$$

In the crystal, the conservation of mass for lithium in the  $\alpha$ -phase and  $\beta$ -phase is given by

$$\frac{\partial ((\theta_\alpha + \theta_{gb}) c_\alpha)}{\partial t} + \frac{\partial (\theta_\beta c_\beta)}{\partial t} = \nabla \cdot (D_{eff} \nabla c_\alpha) \quad (3.6)$$

$$\frac{\partial \theta_\beta}{\partial t} = r_\beta \quad (3.7)$$

$$\theta_\alpha + \theta_\beta + \theta_{gb} = 1 \quad (3.8)$$

where  $c_\alpha$  and  $c_\beta$  are the concentrations of lithium in the  $\alpha$  and  $\beta$ -phases,  $\theta_\alpha$  and  $\theta_\beta$  are the volume fractions of the  $\alpha$  and  $\beta$ -phases respectively,  $r_\beta$  is the rate at which lithium enters the  $\beta$ -phase (leaves the  $\alpha$ -phase) and is discussed below, with further detail in the appendix.  $\theta_{gb}$  is the volume fraction of grain boundaries. It is assumed that some fraction of the particle is composed of voids or grain boundaries and that lithium can reside in these gaps. The void volume of the  $\beta$ -phase is some presumably very small fraction,  $\zeta$ , of the  $\beta$ -phase:

$$\theta_{gb} = \zeta \theta_\beta \quad (3.9)$$

It was initially hypothesized that the effective diffusion coefficient was given by  $D_{eff} = \theta_\alpha D_\alpha$ , where mass transport is increasingly resistive as more  $\beta$ -phase formed. However, this formulation was inconsistent with experiment because it underpredicts the materials capacity when there are significant amounts of  $\beta$ -phase formation. Instead it was hypothesized that diffusion could take place not only through the  $\alpha$ -phase, but also along grain-boundaries and that these two processes could proceed in parallel.

$$D_{eff} = \theta_\alpha D_\alpha + \theta_{gb} D_{gb} \quad (3.10)$$

This formulation is more consistent with experimental observations if  $D_{gb} \sim 100 D_\alpha$  and  $\zeta \sim 0.01$ .

### 3.3.1 Boundary and Initial Conditions

At the beginning of the simulation, the values of  $c_\alpha$  and  $\theta_\beta$  are set to initial values:

$$c_\alpha|_{t=0} = c_{\alpha,0}; \quad \theta_\beta|_{t=0} = \theta_{\beta,0} \quad (3.11)$$

For each crystal, the flux at the (001) surface is defined by the specific current density and symmetry is invoked at the center of the crystal, along the [001] direction:

$$\left. \frac{\partial c_\alpha}{\partial x} \right|_{x=L} = \frac{1}{D_{eff}} \frac{i}{F} \quad (3.12)$$

$$\left. \frac{\partial c_\alpha}{\partial x} \right|_{x=0} = 0 \quad (3.13)$$

where the current density,  $i$ , and specific current,  $i_{app}$ , are related by equation 3.14

$$i = i_{app} \rho L \quad (3.14)$$

### 3.3.2 Kinetics of Phase Change

The kinetics of phase change, equation 3.15 are developed from Avramis mathematical formulation of nucleation and growth,<sup>16-18</sup> where  $k_\beta$  is the reaction rate constant,  $c_\alpha c_{\alpha,sat}$  is the driving force for phase change,  $\theta_\beta$  represents the interfacial area between the  $\alpha$  and  $\beta$ -phases, and  $1 - \theta_\beta$  is the correction for impinging nuclei. A detailed derivation is given in Appendix A. The value of  $m$  changes depending on the rate of nucleation relative to that of growth and the dimensionality of growth (1, 2, or 3-dimensional).

$$\frac{\partial \theta_\beta}{\partial t} = k_\beta (c_\alpha - c_{\alpha,sat}) (\theta_\beta^m) [1 - \theta_\beta]; \quad 0 \leq m \leq 1 \quad (3.15)$$

| <b>3-D<br/>Progressive</b> | <b>3-D<br/>Instantaneous</b> | <b>2-D<br/>Instantaneous</b> | <b>1-D<br/>Instantaneous</b> |
|----------------------------|------------------------------|------------------------------|------------------------------|
| $\theta$                   | $\theta^{2/3}$               | $\theta^{1/2}$               | $\theta^0$                   |

**Table 3.1:** Value of  $m$  for different mechanisms of phase change

Table 3.1 gives the value of  $m$  for some scenarios, but  $m$  can take on any value between 0 and 1. Combining equations 3.6, 3.7, and 3.15 assuming 1-directional diffusion in rectangular coordinates yields

$$\frac{\partial (\theta_\alpha c_\alpha)}{\partial t} = D_{eff} \frac{\partial^2 c_\alpha}{\partial x^2} - k_\beta (c_\alpha - c_{\alpha,sat}) (\theta_\beta^m) [1 - \theta_\beta] \quad (3.16)$$

By introducing dimensionless concentration, position, and time:

$$\bar{c} = \frac{c_\alpha}{c_{\alpha,sat}}; \quad \bar{x} = \frac{x}{L}; \quad \tau = \frac{t}{L^2/D_{eff}} \quad (3.17)$$

equation 3.16 can be recast in dimensionless form:

$$\frac{\partial (\theta_\alpha \bar{c})}{\partial \tau} = \frac{\partial^2 \bar{c}}{\partial \bar{x}^2} - \psi_{Th} (\bar{c} - 1) \theta_\beta^m (1 - \theta_\beta) \quad (3.18)$$

where  $\psi_{Th}$  is the ratio of phase-transformation rate to diffusion rate, akin to the Thiele modulus,

$$\psi_{Th} = \frac{k_\beta L^2}{D_{eff}} \quad (3.19)$$

The boundary condition given by equation 3.12 is also given in dimensionless form:

$$\left. \frac{\partial \bar{c}}{\partial \bar{x}} \right|_{\bar{x}=1} = \bar{i} \quad (3.20)$$

where  $\bar{i}$  is a dimensionless current density:

$$\bar{i} = \frac{L^2 \rho}{D_{eff} c_{\alpha, sat}} \frac{i_{app}}{F} \quad (3.21)$$

As  $\psi_{Th}$  approaches zero, the phase fraction  $\theta_\beta$  is uniform across the crystal, while values approaching infinity will produce profiles resembling step functions. The shrinking-core method assumes instantaneous phase change kinetics,  $\psi_{Th} \rightarrow \infty$ , producing the step change seen in Figure 4. At higher values of  $\psi_{Th}$  the profiles resemble the shrinking-core profile. Figure 4B illustrates the effect of  $\bar{i}$  on the uniformity of the  $\theta_\beta$ -profile. It is observed that, as with  $\psi_{Th}$ , increasing  $\bar{i}$  increases the sharpness of the profile, but the effects are milder. In addition, there is a limit to the extent that changing the flux can affect the profiles. If  $\bar{i}$  is made greater than 100, the profile is identical to the profile when  $\bar{i} = 100$ . The same effect is seen for  $\bar{i}$  less than 0.1.

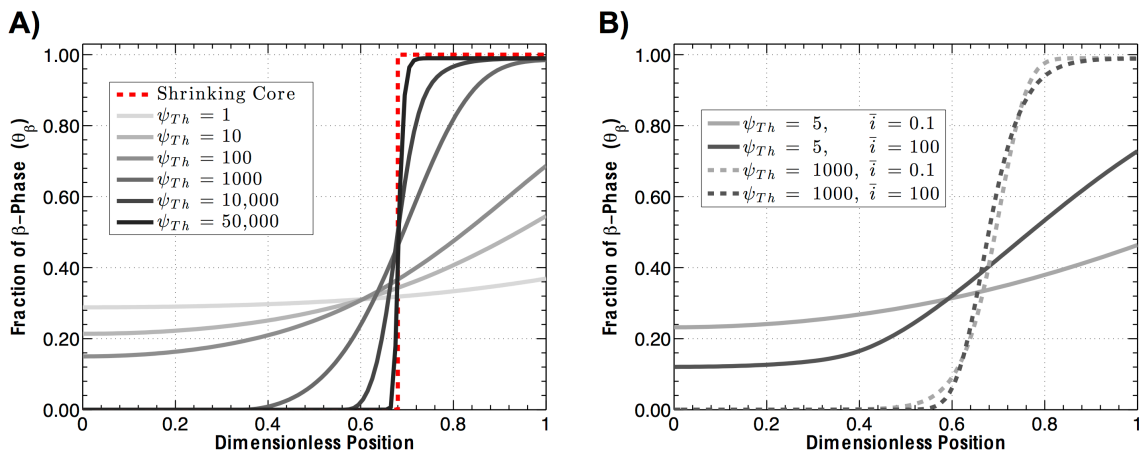


**Figure 3.4:** A) Illustration of the effect of changing  $\psi_{Th}$  on the  $\theta_\beta$  profile within the crystal for  $\bar{i} = 10$ . The profiles are also compared to the profiles produced using the shrinking-core model; it can be seen that at high values of  $\psi_{Th}$ , the model collapses to the shrinking-core model. B) Illustration of the effect of changing  $\bar{i}$  on the  $\theta_\beta$  profile within the crystal for  $\psi_{Th} = 5$ .

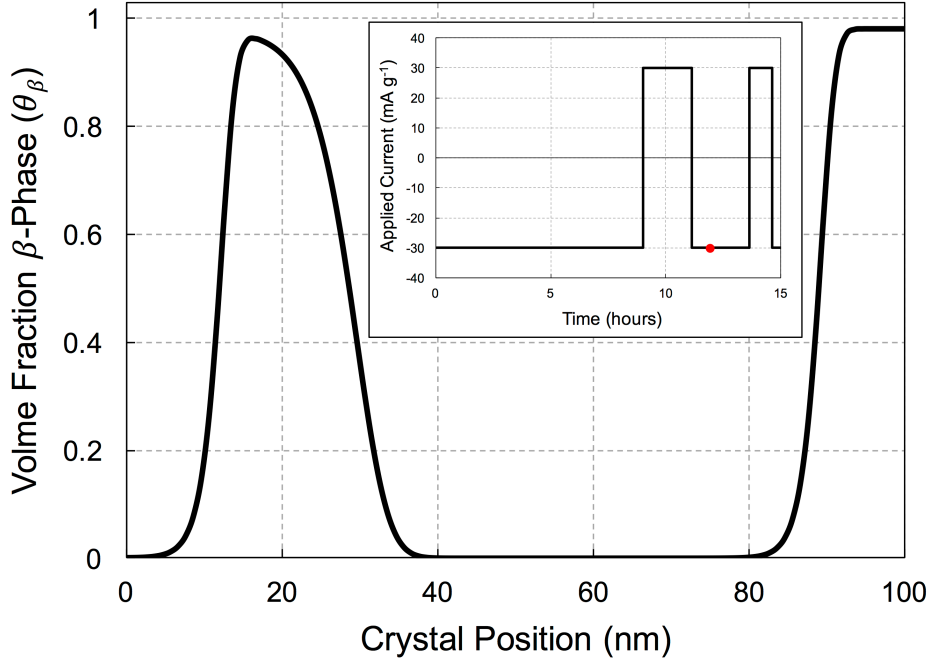


**Figure 3.5:** An illustration of the  $\theta_\beta$  profile within a crystal ( $\psi_{Th} = 10,000$ ,  $m = 0$ ) during a current cycling process ( $\bar{i} = 60$ ). The predicted spatial variation of the regions with two phases is a strong function of the battery usage.

With the shrinking-core method, tracking a few boundaries is manageable, but not trivial. The complexity involved in tracking many boundaries, whose positions vary with time, can make shrinking-core method cumbersome. Additional questions arise concerning the coalescence of boundaries. With the method outlined in this chapter, there is no need to introduce internal boundaries and this is important because simulations of battery cycling may need to account for a large number of scenarios. For example, Figure 5 shows a simulated  $\theta_\beta$  profile, where the battery is discharged before the  $\beta$ -phase is completely consumed during charge. In this case, there are two distinct regions within the crystal with non-zero  $\theta_\beta$ .

### 3.3.3 Numerical Methods

The governing equations were discretized using the forward-time, central-space finite volume method. The scale was discretized, and the resulting block, tri-diagonal matrix was solved in Fortran 95 using the BAND(J) algorithm.<sup>32</sup> The mesh size necessary to adequately resolve the profiles is dependent on the value of  $\psi_{Th}$ ; higher values require

a finer mesh. For comparison to electrochemical data, mesh sizes of 22 points were sufficient. The time step was set to 0.03 seconds. Computer experiments were conducted for the mesh sizes and time steps to ensure convergence.

The shrinking-core method commonly uses a finite volume formulation because it makes handling the internal boundary conditions more manageable. While the finite volume formulation was used to obtain the results shown in this chapter, there are no significant advantages to using the finite volume method over the finite difference method; a corresponding paper treats a different electrochemical system using the finite difference method.<sup>33</sup>

### 3.4 Parameter Estimation

The results of the current interrupt experiments at different rates were used to get order of magnitude estimates for  $k_{rxn}$ ,  $D_\alpha$ , as well as estimates for the equilibrium concentration and the rate constant for  $\beta$ -phase formation. From the voltage recovery data we could elucidate information about charge-transfer and get an estimate for  $k_{rxn}$  (equation 3.5). The instantaneous potential jumps are the sum of the activation and ohmic overpotentials in the electrode. Assuming the ohmic losses are much smaller than the charge-transfer losses, the overpotential can be estimated using Butler-Volmer kinetics. Figure 6A overlays order of magnitude estimations of  $k_{rxn}$  and the experimental voltage jump observed 10 ms after the current is turned off at each current rate.

Using the discharge voltage versus average equivalence (6B) we are able to gain insights into the diffusive properties of lithium in  $\text{LiV}_3\text{O}_8$ . First it should be noted, that estimating the diffusion coefficient requires isolation of mass-transport effects from phase change effects, i.e. we examined the data before the onset of phase-change. In addition, at low current rates ( $C/10$ ) the resolution between  $1 \times 10^{-12}$  and  $1 \times 10^{-13} \text{ cm}^2 \text{ s}^{-1}$  is too low to distinguish between the two conditions. However, using a higher current rate,  $1C$ , improves the resolution between these two cases, from which it is clearly observed that the best estimate of the diffusion coefficient is  $1 \times 10^{-13} \text{ cm}^2 \text{ s}^{-1}$ . Additionally because the

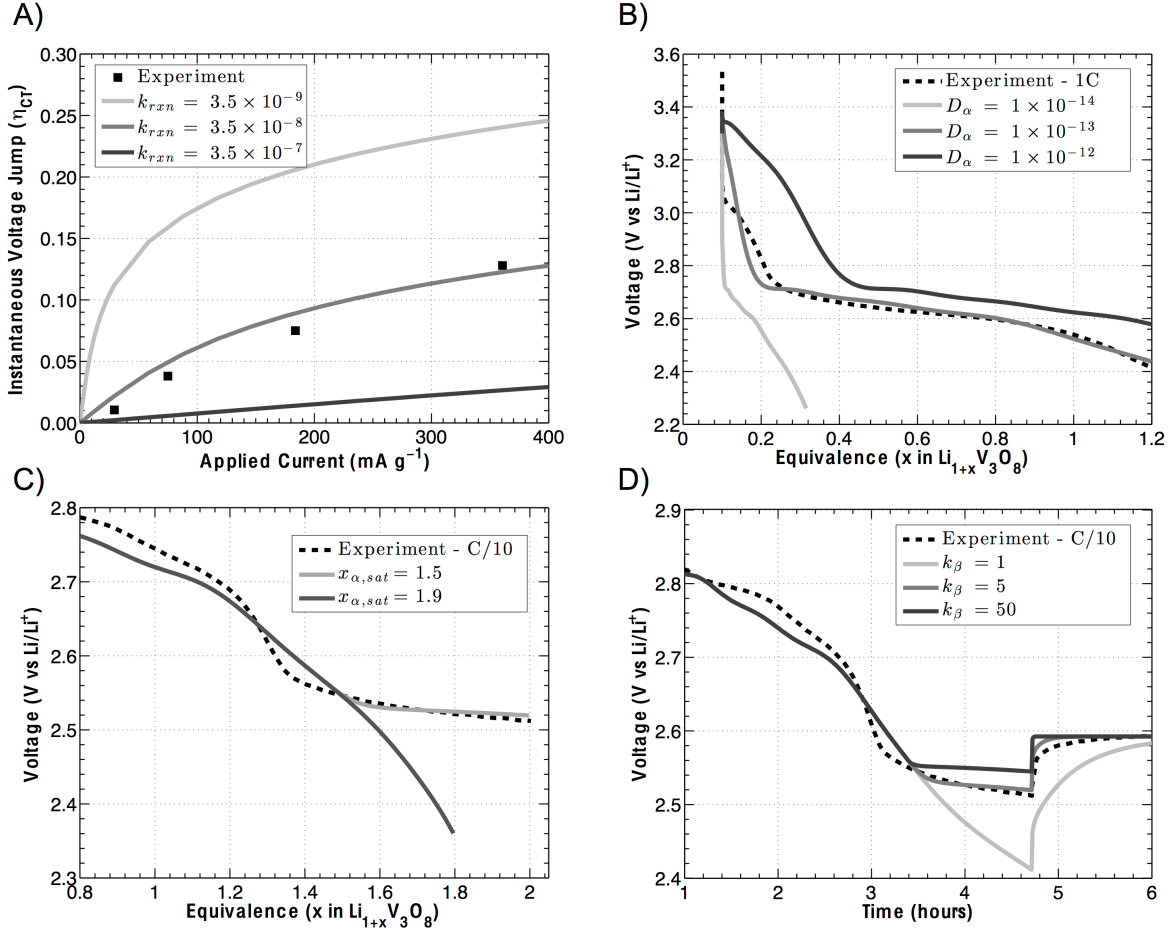


**Figure 3.6:** Qualitative comparisons used for parameter estimation of A)  $k_{rxn}$ , B)  $D_\alpha$ , C)  $x_{\alpha,sat}$ , and D)  $k_\beta$ . A) compares varying exchange current densities with the charge-transfer losses at different current rates. B) compares varying diffusion coefficient at a current rate of 1C; C) and D) compare varying saturation concentrations and phase change reaction coefficients, respectively, with experiments conducted at C/10.

value of the effective diffusion coefficient was not found to change much in the two-phase region,<sup>8</sup>  $D_{gb}$  was assumed to be 100 times greater than  $D_\alpha$ .

Next, it was important to establish equilibrium concentrations of lithium in the  $\alpha$ -phase and  $\beta$ -phase. As previously described, the equilibrium concentration in the lithium-deficient phase was not established with certainty in the literature. Namely, it was debated whether the equilibrium concentrations were  $\text{Li}_{2.5}\text{V}_3\text{O}_8:\text{Li}_4\text{V}_3\text{O}_8$ ,<sup>34,35</sup> or as others suggest  $\text{Li}_{2.9-3.0}\text{V}_3\text{O}_8:\text{Li}_4\text{V}_3\text{O}_8$ .<sup>9,10,36</sup> Because it is generally accepted that the  $\beta$ -phase composition is  $\text{Li}_4\text{V}_3\text{O}_8$ ,  $x_{\beta,sat}$  was set to 3 ( $c_{\beta,sat} = 0.0365 \text{ mol cm}^{-3}$ ). Because the consensus in the literature is that there are only two probable possibilities for the equilibrium concentration in the  $\alpha$ -phase, it is relatively easy for us to test the two cases

and compare the results, which are given in Figure 6C. Clearly,  $x_{\alpha,sat} = 1.5$  ( $c_{\alpha,sat} = 0.0182 \text{ mol cm}^{-3}$ ), or  $\text{Li}_{2.5}\text{V}_3\text{O}_8:\text{Li}_4\text{V}_3\text{O}_8$  gives better agreement with experimental data. While some may contend that the value of  $x_{\alpha,sat}$  needs to be fitted with the value of  $k_\beta$ , this is simply not true for this particular case. While it is true that some non-zero value of  $k_\beta$  needed to be selected, the value of  $k_\beta$  only controls the slope of the voltage plateau, while  $x_{\alpha,sat}$  can be thought of as controlling the vertical position (the analog of the y-intercept). Using this reasoning,  $x_{\alpha,sat}$  and  $k_\beta$  can (and should) be determined independently for this case.

Figure 6D shows a comparison of experimental measurements with simulations incorporating phase change with varying rate constants,  $k_\beta$ . It can be appreciated that as  $k_\beta$  is increased from 1 to  $50 \text{ cm}^3 \text{ mol}^{-1} \text{ s}^{-1}$ , the slope of the voltage plateau decreases, and the performance increases. The performance increase is due to decreases in the concentration overpotentials. As  $k_\beta$  increases, the voltage is also able to recover more quickly. The parameter  $k_\beta$  was selected to obtain the best agreement with experimental data during the voltage plateau as well as during the voltage recovery. The reaction rate constant,  $k_\beta$ , was found to be  $5.0 \times 10^{-3} \text{ cm}^3 \text{ mol}^{-1} \text{ s}^{-1}$ , yielding  $\psi_{Th} = 5$ . The reader should note that the parameter  $m$ , equation 3.15, may also be fit with  $k_\beta$ .

Values of  $m$  not equal to 0, contribute to a shallow local voltage minimum at intermediate values of capacity. Because these local voltage minima were not observed experimentally and because of the fast phase change kinetics observed in the  $\text{LiV}_3\text{O}_8$  electrode,  $m = 0$  was concluded to be the best estimation. The value of  $m = 0$  corresponds to 1-dimensional growth and instantaneous nucleation, and numerical simulations show that  $m = 0$  agrees well with experimental data. New phases have been observed to grow through one-dimensional growth and instantaneous nucleation in electrode materials with similar structures.<sup>37</sup> Other values of  $m$  seem to be in better agreement with other electrode materials.<sup>33</sup>

Because we have adjusted five parameters: the charge-transfer rate constant, the diffusion coefficient, the saturation concentration, the phase change rate constant, as well as the dimensionality of nucleation and growth to achieve the model-experimental fits in

Figure 6, a discussion about the validity of the parameters estimated is necessary. First, the charge-transfer rate constant and diffusion coefficient can be estimated independently, therefore we believe those estimates to be reasonable. In addition, the diffusion coefficient suggested by Figure 6B is within the range reported in the literature,  $1 \times 10^{-11} - 1 \times 10^{-15} \text{ cm}^2 \text{ s}^{-1}$ .<sup>8</sup> The remaining two parameters,  $x_{\alpha,sat}$  and  $k_{\beta}$ , could not be selected without first establishing the diffusion coefficient.

Concerning the saturation composition, the tested compositions are supported by experimental literature. Additionally, DFT calculations indicate that the saturation composition in the  $\alpha$ -phase is  $\text{Li}_{2.5}\text{V}_3\text{O}_8$ .<sup>27</sup> In summary, experiments, theoretical calculations, and this continuum model all suggest the saturation composition in the  $\alpha$ -phase is  $\text{Li}_{2.5}\text{V}_3\text{O}_8$ .

Finally, this brings us to the selection of the phase change kinetic parameters. First, it should be noted that changing the value of  $k_{\beta}$  does not impact the experiment-model agreement before the onset of phase change, above 2.5 V. While it cannot be said that  $k_{\beta}$  is determined independently from the previously fitted parameters, the foundation of the diffusion coefficient and saturation concentration in experimental data lends credence to the validity of the selected phase change kinetic constant. A summary of all the selected model parameters is given in Table 3.2.

| <b>Paramter</b>   | <b>Value</b>         |
|---|----------------------|
| $L$ (nm)  | 100                  |
| $D_{\alpha}$ ( $\text{cm}^2 \text{s}^{-1}$ )                    | $1 \times 10^{-13}$  |
| $D_{gb}$ ( $\text{cm}^2 \text{s}^{-1}$ )                        | $1 \times 10^{-13}$  |
| $\xi$   | 0.01                 |
| $\rho$ ( $\text{g cm}^{-2}$ )                                   | 3.5                  |
| $c_{\alpha,sat}$ ( $\text{mol cm}^{-3}$ )                       | 0.0182               |
| $c_{\beta,sat}$ ( $\text{mol cm}^{-3}$ )                        | 0.0365               |
| $k_{rxn}$ ( $\text{cm}^{5/2} \text{mol}^{-1/2} \text{s}^{-1}$ ) | $3.5 \times 10^{-8}$ |
| $k_{\beta}$ ( $\text{cm}^3 \text{mol}^{-1} \text{s}^{-1}$ )     | $5.0 \times 10^{-3}$ |
| $m$   | 0                    |

**Table 3.2:** Parameter values used to model the  $\text{LiV}_3\text{O}_8$  electrode.

### 3.5 Results

Figure 7 shows the experimental and simulated voltage during discharge and recovery at current rates of C/10, C/5, C/2, and 1C (37.49, 74.98, 182.8, and 360.6 mA g<sup>-1</sup> respectively). Maintaining the same parameter values for each experiment, the simulations accurately predict the voltage plateau (~2.5 V) as well as the transient and the final resting voltage during voltage recovery.

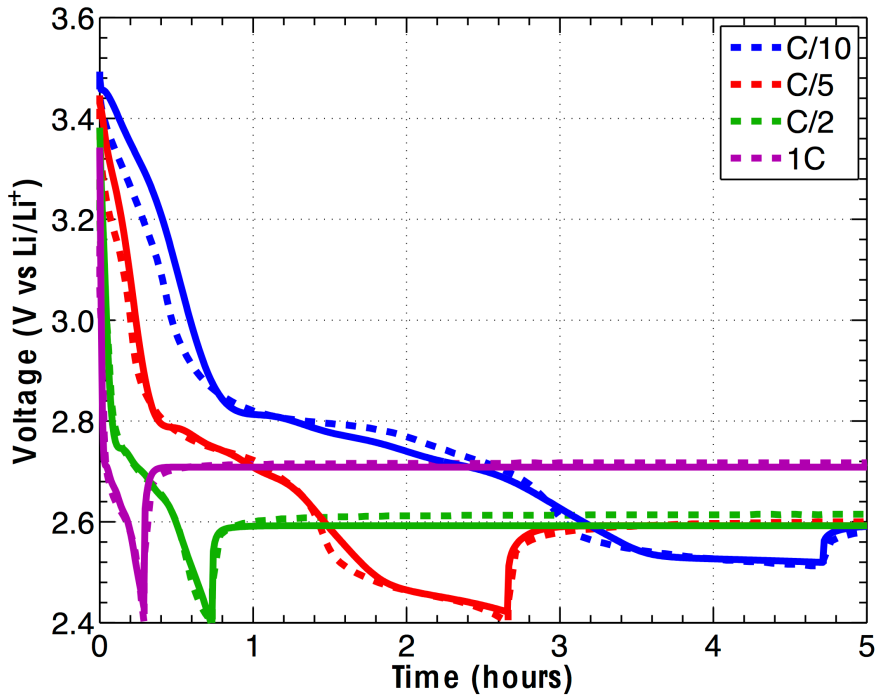


**Figure 3.7:** Experimental (dashed lines) and simulated (solid lines) potential during discharge (lithiation) and after interruption of current. Comparisons are shown for four discharge rates. The rapid change in slope of the curves is the result of current interruption.

Figure 7 appears to validate the model during discharge and voltage recovery; it is also important to validate the model during charge. Figure 8A shows the experimental charge data and Figure 8B shows the simulated charge experiments. The agreement between simulation and experiment is good until the end of charge (low values of capacity), where the voltage rapidly increases with decreasing capacity. In the circled region, the experimental voltage profiles collapse onto each other, suggesting smaller overpotentials during delithiation than lithiation. Simulations were conducted assuming no charge-transfer losses, but this still could not produce the observed trend. Experimental trends

were captured in the simulations by increasing the diffusion coefficient during charge by a factor of 5.

The question is then, why are there differences between lithiation and delithiation? In assumption 7 it was asserted that concentration variations in the [100] direction were negligible, in part because of the lower mobility perpendicular to the [100] direction and in part because charge-transfer at the (100) face was unfavorable due to a relatively low binding energy for  $\text{Li}^+$  (this assumes a mechanism requiring surface adsorption prior to insertion). Possibly, the low sticking probability of  $\text{Li}^+$  on the (100) face may limit the lithiation and may enhance the delithiation rate. If indeed the (100) face is active during delithiation, diffusion may proceed in all directions, albeit with a significantly lower mobility perpendicular to the (100) face. Alternatively, diffusion perpendicular to the (100) face may occur primarily through grain boundaries.

Independent of the precise mechanism, comparisons between experiments (8A) and simulations (8B) during discharge and charge are in agreement by assuming a  $5\times$  increase in an effective diffusion coefficient during charge. Simulations suggest that enhanced activity of the (100) face impacts delithiation NOT by reducing the charge-transfer resistance, but instead by allowing an alternative mass-transfer path for the solid-state lithium to exit the crystal. In other words, transport anisotropy is not required to justify the model during lithiation, an alternative rationale is that the (100) face is an insulator to lithiation because surface adsorption energetics are not favorable. We speculate that both anisotropic transport and face-dependent kinetics may play a role.

Using the model we can examine the factors that contribute to voltage losses within the electrode. This is illustrated in Figure 10 for a rate of  $C/5$ , which focuses only on the two-phase portion of the discharge curve. The experimental data and model fit represent the potential between the lithium-metal anode and the vanadate cathode. The losses can be split into three components: losses due to charge-transfer, non-instantaneous phase change kinetics (supersaturation), and mass-transport. The open-circuit voltage is obtained in simulations assuming zero charge-transfer losses, infinitely fast phase change kinetics, and no mass-transfer resistances. The individual losses can be quantified by

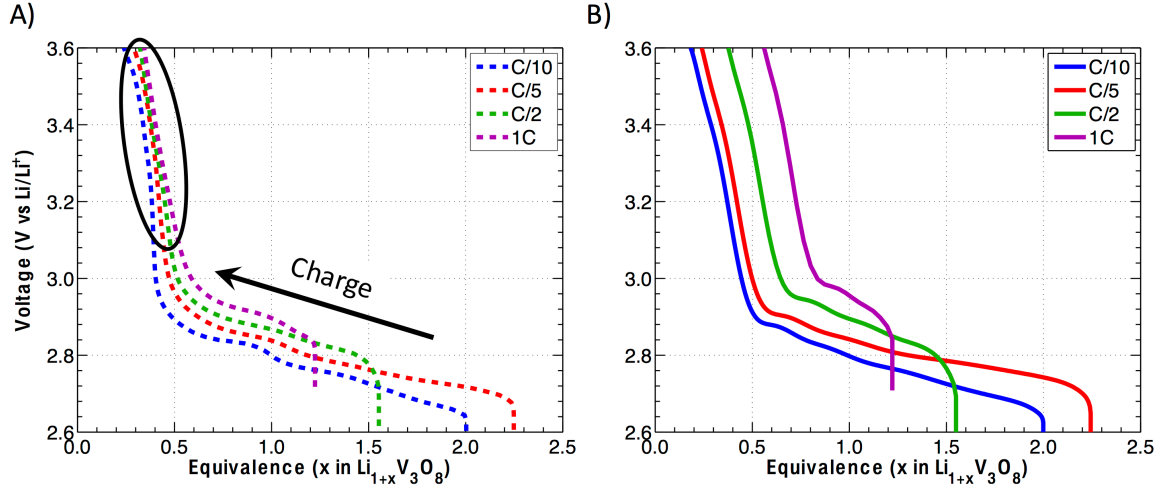


**Figure 3.8:** Experimental (A) potential during charge (delithiation) at different rates. The corresponding simulated (B) potential is shown for comparison. The simulations do not capture the relatively small changes in potential with charge rate observed at low equivalence.

sequentially relaxing these ideal assumptions. Before phase change potential losses arise due to charge-transfer and mass-transfer resistances. At the end of the discharge, all three effects present significant voltage drops to the system. Considering this information in the context of cell design, it suggests that decreasing the crystal size could significantly improve performance by decreasing the diffusion path-length thereby decreasing the mass-transfer resistance; additionally, the smaller crystal sizes would have a larger surface area to volume ratio, which would improve charge-transfer resistance. However, it is unclear how smaller crystals would impact phase-change kinetics and consideration needs to be given to how crystal size will affect cycling performance of this material.

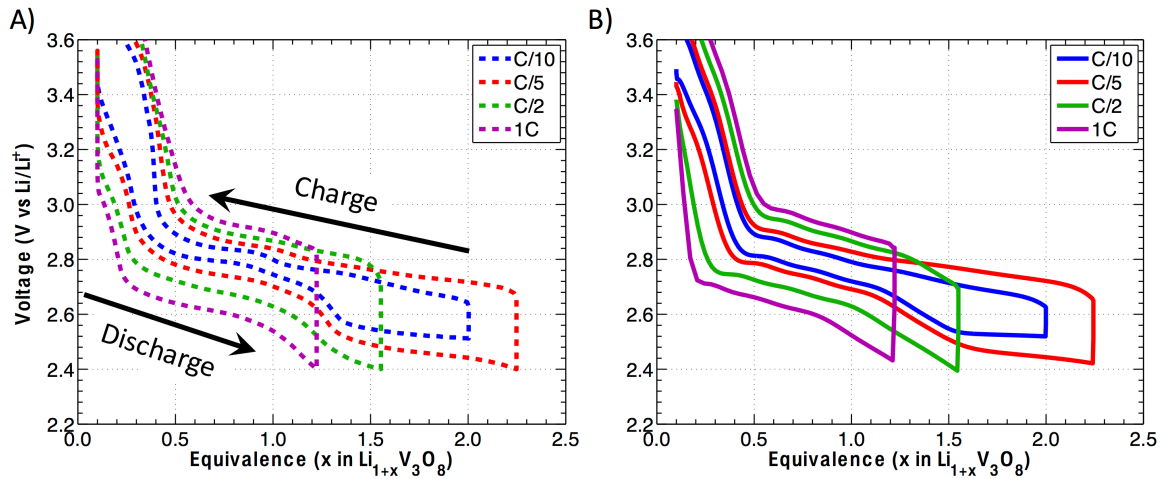


**Figure 3.9:** Experimental (A) potential during charge and discharge at different rates. The corresponding simulated (B) potential is shown for comparison. If the diffusion coefficient is increased during charge, then the simulation curves collapse onto each other as is observed experimentally, providing significant improvement from those observed in Figure 3.8.

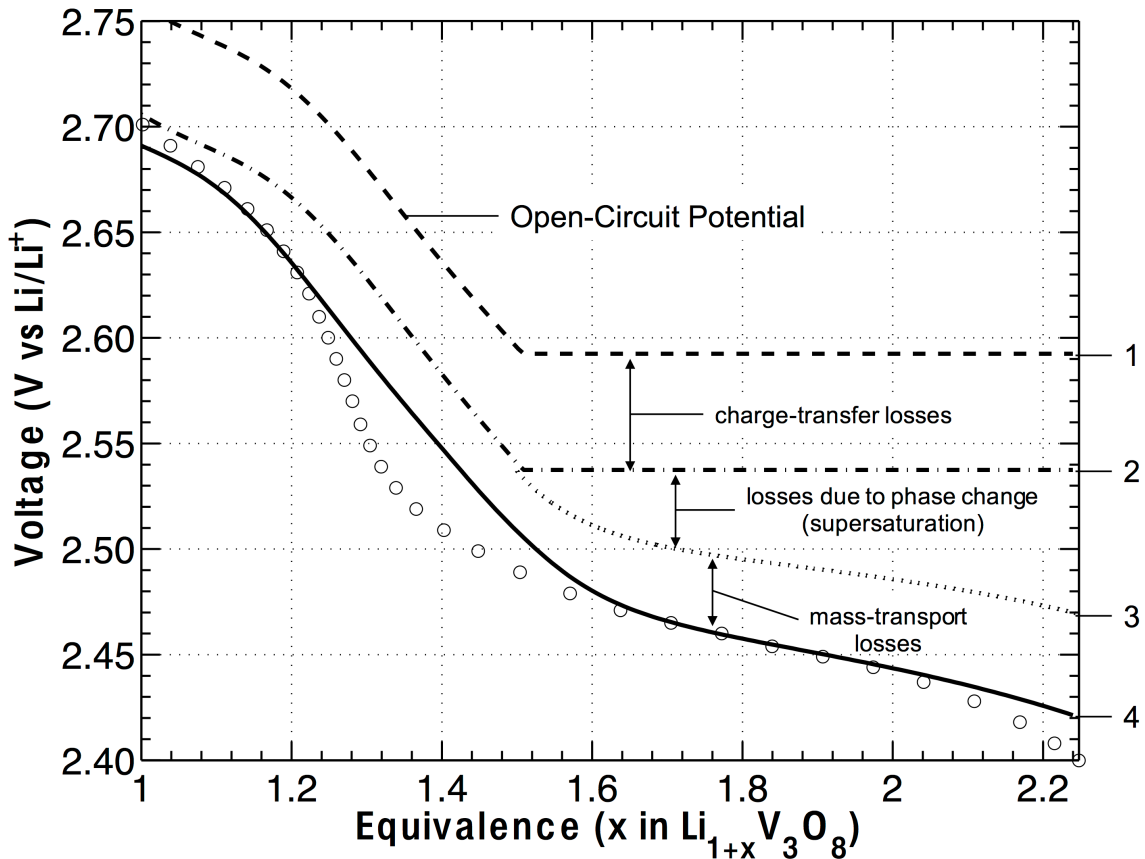


**Figure 3.10:** Estimation of the potential drops in the lithium trivanadate electrode at a current rate of C/5, focusing on the two-phase region. The graph shows qualitatively the contributions to the observed overpotential. 1) reversible potential, 2) charge-transfer resistance only, 3) charge-transfer and estimated phase-change resistances, assuming no concentration variations, 4) charge transfer, estimated phase-change, and estimated mass-transfer resistances.

## 3.6 Conclusions

A combined experimental and theoretical study suggests that the phase transformation from  $\alpha$ - $\text{Li}_{1+x}\text{V}_3\text{O}_8$  to  $\beta$ - $\text{Li}_4\text{V}_3\text{O}_8$  is relatively facile. A model to analyze the electrochemical behavior and phase transformation also requires a description of mass transport of lithium in the crystal host material. Although SEM analysis reveals that the crystals aggregate, from the analysis of the time constant associated with voltage recovery it was concluded that the significant mass transfer resistances occur on the crystal scale and these resistances are consistent with the assumption of 1-D diffusion along the [001] direction. Fitted phase-transformation kinetics suggest that  $\psi \sim 5$ , and a shrinking-core model of phase distributions within a crystal is thus not appropriate. The excellent agreement between simulated and experimental lithiation results validates the selected diffusion coefficient of lithium in  $\text{LiV}_3\text{O}_8$ , as well as the selected value of the equilibrium concentration of lithium in the  $\alpha$ -phase. Comparisons also suggest that transport processes within the crystal may be more rapid during charge than discharge, from which we have hypothesized that the (001) crystal face may be active during charge but not during discharge. An analysis of the potential drop contributions indicates that losses due to charge-transfer, mass-transfer, as well as phase change are all significant.

## 3.7 Acknowledgements

The research was supported by the Center for Mesoscale Transport Properties, an Energy Frontier Research Center supported by the U.S. Department of Energy (DOE), Office of Science, Basic Energy Sciences (BES), under award #DE-SC0012673. Microscopy were conducted at the Center for Functional Nanomaterials at Brookhaven National Laboratory was supported by DOE-BES User Facility Division, under Contract No. DE-SC0012704.

## 3.8 Appendix A

This appendix details the mathematical model for the formulation of a new phase, equation 3.15 in the text, which is based on the formulations for nucleation and growth developed by Avrami.<sup>16-18,38</sup> First, it is assumed that the radius, or characteristic length, of a nucleus grows at a constant rate,  $v$  and can be described by equation 3.22.

$$r(t) = r^* + vt \approx vt \quad (3.22)$$

where  $r^*$  is the critical radius of a nucleus, and  $t$  is time. Assuming spherical particles, the volume of a single nucleus is given by 3.23, and differentiating with respect to the time gives 3.24.

$$V = \frac{4}{3}\pi r^3 = \frac{4}{3}\pi v^3 t^3 \quad (3.23)$$

$$\frac{dV}{dt} = 4\pi v^3 t^2 = k_g V^{\frac{2}{3}} \quad (3.24)$$

where  $k_g$  is the growth rate constant.

Next it is important to quantify the total volume of the  $\beta$ -phase, which is a product of the number of nuclei, and the volume per nuclei,  $V$ :

$$\frac{dV_\beta}{dt} = n \frac{dV}{dt} = n (4\pi v^3 t^2) \quad (3.25)$$

As the nuclei grow they will begin to impinge upon each other. To ensure that there is no double counting,  $n$  represents the number of isolated nuclei, given as  $n_0 [1 - \theta]$ , where  $n_0$  is the total number of nuclei. As the volume fraction of  $\beta$ -phase increases, it becomes more likely that nuclei will impinge on each other, therefore decreasing the number of isolated nuclei. As super-saturation increases it is expected to favor nucleation, i.e.  $(c_\alpha - c_{\alpha,sat})$  is the driving force for nucleation. The growth rate,  $v$ , of an individual nucleus is assumed to be unaffected by super-saturation. Assuming progressive nucleation,  $n$  can be represented using equation 3.26:

$$n = (k_n (c_\alpha - c_{\alpha,sat}) t) [1 - \theta_\beta] \quad (3.26)$$

where  $k_n$  is the nucleation rate constant. Combining equations 3.25 and 3.26 and dividing by the total volume,  $V_{tot}$ , produces 3.27, which is a specific case of equation 3.15, where  $m = 1$ .

$$\begin{aligned} \frac{1}{V_{tot}} \frac{dV_\beta}{dt} &= \frac{1}{V_{tot}} (4\pi v^3 t^3) k_n (c_\alpha - c_{\alpha,sat}) [1 - \theta_\beta] \\ &= \frac{1}{V_{tot}} k_n (c_\alpha - c_{\alpha,sat}) (4\pi V) [1 - \theta_\beta] \\ \frac{d\theta_\beta}{dt} &= k_\beta (c_\alpha - c_{\alpha,sat}) (\theta_\beta) [1 - \theta_\beta] \end{aligned} \quad (3.27)$$

### 3.9 Appendix B

This appendix lists the open-circuit potential of excess lithium in lithium trivanadate ( $\text{LiV}_3\text{O}_8$ ). The expression for the open-circuit potential as a function of lithium concentration in the  $\alpha$ -phase is derived using the approach outlined by Karthikeyan *et al.*<sup>39</sup> The open-circuit potential at a particular lithium concentration was estimated using

$$\begin{aligned} U &= U_{ref} + \frac{RGT}{F} \ln \left[ \left( \frac{c}{c_0} \right) \left( \frac{1 - \bar{c}_{max}}{\bar{c}_{max}} \right) \right] \\ &\quad + \sum_{k=0}^N A_k \left[ (2\bar{c}_{max} - 1)^{k+1} - \frac{2\bar{c}_{max}^k (1 - \bar{c}_{max})}{(2\bar{c}_{max} - 1)^{1-k}} \right] \end{aligned} \quad (3.28)$$

where  $c$  is local concentration of lithium in the electrolyte. The parameters in equation 3.28 are obtained by fitting the equation to experimental data and the values for the parameters are given in Table B1 and the fit is shown in Figure B1. The reason the empirical open-circuit voltage (OCV) falls below the experimental electrochemical data ( $x = 1.6$  in  $\text{Li}_{1+x}\text{V}_3\text{O}_8$ ) is that the empirical OCV neglects the effects of phase change. The

effects of phase change on the experimental data is to suppress the lithium concentration in the  $\alpha$ -phase, see equation 3.6.

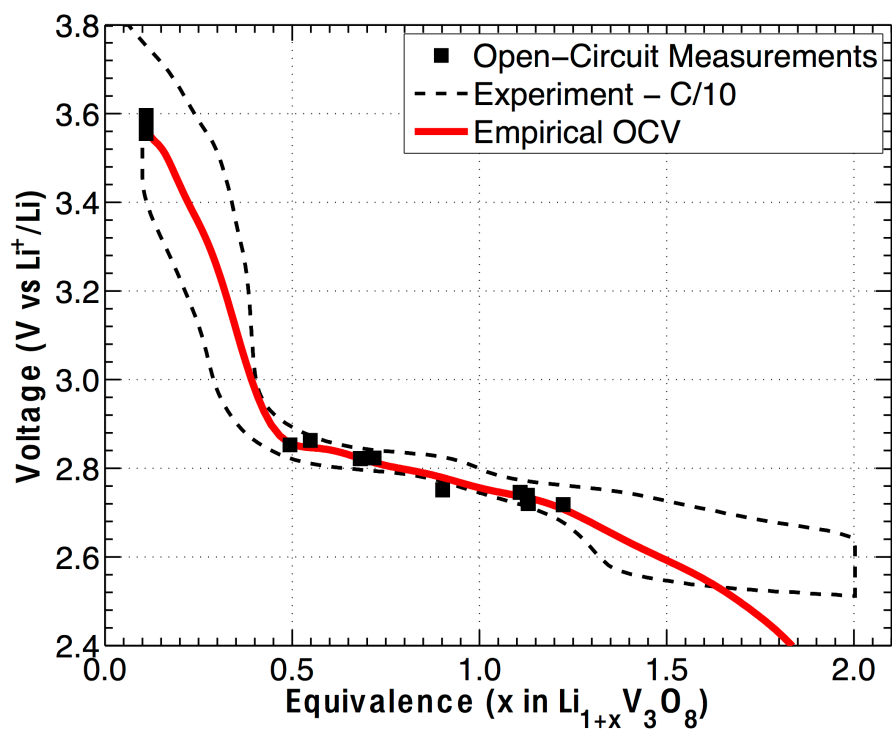


**Figure 3.11:** Open-circuit voltage measurements (squares) were taken and the empirical open-circuit voltage curve (solid red) was constructed to reside between the discharge and charge curve (dashed) at the lowest current rate.

| Parameter                               | Value    |
|---|----------|
| $N$                                     | 20       |
| $U_{ref}$                               | 2.7671   |
| $A_0$                                   | -0.32895 |
| $A_1$                                   | 0.057048 |
| $A_2$                                   | -0.21475 |
| $A_3$                                   | 0.24177  |
| $A_4$                                   | 1.8186   |
| $A_5$                                   | -0.32144 |
| $A_6$                                   | -19.037  |
| $A_7$                                   | 11.997   |
| $A_8$                                   | 107.13   |
| $A_9$                                   | -111.70  |
| $A_{10}$                                | -355.17  |
| $A_{11}$                                | 489.45   |
| $A_{12}$                                | 696.86   |
| $A_{13}$                                | -1133.1  |
| $A_{14}$                                | -813.10  |
| $A_{15}$                                | 1438.6   |
| $A_{16}$                                | 568.70   |
| $A_{17}$                                | -953.47  |
| $A_{18}$                                | -237.50  |
| $A_{19}$                                | 260.21   |
| $A_{20}$                                | 52.050   |
| $c_0$ (mol cm <sup>3</sup> )            | 0.001    |
| $c_{\alpha,max}$ (mol cm <sup>3</sup> ) | 0.0243   |

**Table 3.3:** Parameters for the empirical open circuit potential of the  $\alpha$ -phase derived from the Redlich-Kister expression (see equation 3.28 and Figure 3.11).

### 3.10 List of Symbols

|                      |   |   |
|----------------------|---|---|
| $c_0$                | bulk concentration of lithium in the electrolyte                            | $\text{mol cm}^{-3}$                              |
| $c_{\alpha, \max}$   | maximum solid-state lithium concentration                                   | $\text{mol cm}^{-3}$                              |
| $\bar{c}$            | dimensionless concentration   | (-)   |
| $D$                  | solid-states diffusion coefficient  | $\text{cm}^2 \text{s}^{-1}$                       |
| $D_{eff}$            | effective solid-states diffusion coefficient                                | $\text{cm}^2 \text{s}^{-1}$                       |
| $F$                  | Faradays constant   | $96\,485 \text{ C mol}^{-1}$                      |
| $i$                  | current density   | $\text{A cm}^{-2}$                                |
| $\bar{i}$            | dimensionless current density   | (-)   |
| $i_0$                | exchange current density  | $\text{A cm}^{-2}$                                |
| $i_{app}$            | applied current   | $\text{A g}^{-1}$                                 |
| $k_g$                | growth rate constant  | $\text{s}^{-1}$                                   |
| $k_n$                | nuclei formation rate constant  | $\text{cm}^3 \text{mol}^{-1} \text{s}^{-1}$       |
| $k_{rxn}$            | reaction rate constant  | $\text{cm}^{5/2} \text{mol}^{-1/2} \text{s}^{-1}$ |
| $k_\beta$            | rate constant for phase formation   | $\text{cm}^3 \text{mol}^{-1} \text{s}^{-1}$       |
| $L$                  | characteristic length of the crystal  | $\text{cm}$                                       |
| $m$                  | indicates the dimensionality of growth<br>and nucleation of phase formation | (-)   |
| $n$                  | number of nuclei  | (-)   |
| $r$                  | particle radius   | $\text{cm}$                                       |
| $r^*$                | critical particle radius  | $\text{cm}$                                       |
| $R_G$                | ideal gas constant  | $8.314 \text{ J mol}^{-1} \text{ K}^{-1}$         |
| $t$                  | time  | $\text{s}$  |
| $T$                  | temperature   | $\text{K}$  |
| $v$                  | linear growth rate in Avrami formulation                                    | $\text{cm s}^{-1}$                                |
| $V$                  | volume  | $\text{cm}^3$                                     |
| $V_{tot}$            | total volume  | $\text{cm}^3$                                     |
| $x$                  | linear position in the crystal  | $\text{cm}$                                       |
| $\bar{x}$            | dimensionless posioint  | (-)   |
| $\alpha_a, \alpha_c$ | anodic and cathodic charge-transfer coefficients                            | (-)   |
| $\eta$               | overpotential   | $\text{V}$  |
| $\theta$             | volume fraction of phase  | (-)   |
| $\rho$               | density of crystal material   | $\text{g cm}^{-3}$                                |
| $\tau$               | characteristic time ( $L^2/D$ )   | (-)   |
| $\psi_{Th}$          | ratio of rate of phase transformation<br>to diffusive mass transfer rate    | (-)   |

### Subscript

|          |   |
|----------|---|
| $\alpha$ | denotes the $\alpha$ -phase (alpha-phase) |
| $\beta$  | denotes the $\beta$ -phase (beta-phase)   |
| $CT$     | charge-transfer                           |
| $gb$     | grain-boundary                            |
| $MT$     | mass-transfer                             |

## 3.11 Bibliography

- [1] H. Wu and Y. Cui, *Nano Today*, **7**, 414 (2012).
- [2] M. S. Whittingham, (607) (2004).
- [3] S. Panero, M. Pasquali, and G. Pistoia, *Journal of The Electrochemical Society*, **130**(5), 1225 (1983).
- [4] M. E. Spahr, P. Novák, W. Scheifele, O. Haas, and R. Nesper, **145**(2), 421 (1998).
- [5] N. A. Chernova, M. Roppolo, C. Dillon, and M. S. Whittingham (2009).
- [6] A. Pan, J. Liu, J.-g. Zhang, G. Cao, W. Xu, Z. Nie, X. Jie, D. Choi, B. W. Arey, and S. Liang, *Journal of Materials Chemistry*, **21**, 1153 (2011).
- [7] M. Winter, J. O. Besenhard, M. E. Spahr, and P. Novák, *Advanced Materials*, **10**(10), 725 (1998).
- [8] S. Sarkar, A. Bhowmik, M. D. Bharadwaj, and S. Mitra, *Journal of The Electrochemical Society*, **161**(1), A14 (2014).
- [9] G. Pistoia, M. Pasquali, M. Tocci, R. V. Moshtev, and V. Maner, *Journal of The Electrochemical Society*, **132**(2), 281 (1985).
- [10] L. A. Picciotto, K. T. Adendorff, D. Liles, and M. Thackeray, *Solid State Ionics*, **62**, 297 (1993).
- [11] S. Jouanneau, A. Ñ. Verbaere, and D. Guyomard, *Journal of Solid State Chemistry*, **178**, 22 (2005).
- [12] V. Srinivasan and J. Newman, *Journal of The Electrochemical Society*, **151**(10), A1517 (2004).
- [13] A. S. Andersson and J. O. Thomas, *Journal of Power Sources*, **97-98**, 498 (2001).
- [14] C. Delmas, M. Maccario, L. Croguennec, F. L. Cras, and F. Weill, *Nature Materials*, **7**, 665 (2008).

- [15] L. Laffont, C. Delacourt, P. Gibot, M. Y. Wu, P. Kooyman, C. Masquelier, and J. M. Tarascon, *Journal of Power Sources*, **152**(5), 5520 (2006).
- [16] M. Avrami, *The Journal of Chemical Physics*, **7**, 1103 (1939).
- [17] M. Avrami, *The Journal of Chemical Physics*, **8**, 212 (1940).
- [18] M. Avrami, *Journal of Chemical Physics*, **9**, 177 (1941).
- [19] J. L. Allen, T. R. Jow, and J. Wolfenstine, *Chemistry of Materials*, **19**(8), 2108 (2007).
- [20] N. W. Brady, K. W. Knehr, C. A. Cama, C. N. Lininger, Z. Lin, A. C. Marschilok, K. J. Takeuchi, E. S. Takeuchi, and A. C. West, *Journal of Power Sources*, **321**, 106 (2016).
- [21] A. C. Marschilok, S. H. Lee, C. C. Milleville, P. Chen, E. S. Takeuchi, and K. J. Takeuchi, *Journal of Composite Materials*, **47**(1), 33 (2013).
- [22] J. P. Perdew and Y. Wang, *Physical Review B*, **46**(20), 12947 (1992).
- [23] G. Kresse and J. Furthmüller, *Physical Review B*, **54**(16), 11169 (1996).
- [24] A. Jain, G. Hautier, C. J. Moore, S. Ping Ong, C. C. Fischer, T. Mueller, K. A. Persson, and G. Ceder, *Computational Materials Science*, **50**(8), 2295 (2011).
- [25] H. J. Monkhorst and J. D. Pack, Special points for Brillouin-zone integrations\*, Technical report (1976).
- [26] M. Thackeray, W. David, and J. Goodenough, *Materials Research Bulletin*, **17**(6), 785 (1982).
- [27] T. Jiang and M. L. Falk, *Physical Review B*, **85**(245111), 1 (2012).
- [28] K. W. Knehr, N. W. Brady, C. A. Cama, D. C. Bock, Z. Lin, C. N. Lininger, A. C. Marschilok, K. J. Takeuchi, E. S. Takeuchi, and A. C. West, *Journal of The Electrochemical Society*, **162**(14), A2817 (2015).

- [29] K. W. Knehr, N. W. Brady, C. N. Lininger, C. A. Cama, D. C. Bock, Z. Lin, A. C. Marschilok, K. J. Takeuchi, E. S. Takeuchi, and A. C. West, *ECS Transactions*, **69**(1), 7 (2015).
- [30] A. D. Wadsley, *Acta Crystallographica*, **10**(4), 261 (1957).
- [31] N. Kumagai, A. Yu, and M. Science, **144**(3), 830 (1997).
- [32] J. Newman and K. E. Thomas-Alyea, *Electrochemical Systems*, John Wiley & Sons Inc., Hoboken, New Jersey, 3rd edition (2004).
- [33] K. W. Knehr, C. A. Cama, N. W. Brady, A. C. Marschilok, K. J. Takeuchi, E. S. Takeuchi, and A. C. West, *Electrochimica Acta*, **238**, 384 (2017).
- [34] G. Pistoia, M. L. Di Vona, and P. Tagliatesta, *Solid State Ionics*, **24**(2), 103 (1987).
- [35] A. Hammou and A. Hammouche, *Electrochimica Acta*, **33**(12), 1719 (1988).
- [36] J. Kawakita, Y. Katayama, T. Miura, and T. Kishi, *Solid State Ionics*, **110**, 199 (1998).
- [37] G. Chen, X. Song, and T. J. Richardson, *Electrochemical and Solid-State Letters*, **9**(6), A295 (2006).
- [38] A. Jena and M. C. Chaturvedi, *Phase Transformation in Materials*, Prentice Hall (1992).
- [39] D. K. Karthikeyan, G. Sikha, and R. E. White, *Journal of Power Sources*, **185**, 1398 (2008).

## Chapter 4

# *Operando* Study of $\text{LiV}_3\text{O}_8$ Cathode: Coupling EDXRD Measurements to Simulations<sup>††</sup>

---

<sup>††</sup>This work has been published: Nicholas W. Brady, Qing Zhang, Andrea Bruck, David C. Bock, Christian Alexander Gould, Amy C. Marschilok, Kenneth Takeuchi, Esther Takeuchi, and Alan C. West. “Operando Study of  $\text{LiV}_3\text{O}_8$  Cathode: Coupling EDXRD Measurements to Simulations.” *Journal of The Electrochemical Society* 165, no. 2 (2018): A371-A379.

The thesis writer’s contribution to this work was the model development and the analysis of the simulated results. The electrochemical results and energy dispersive x-ray diffraction results were provided by Qing Zhang, Andrea Bruck, and David C. Bock from the Marschilok-Takeuchi Research Group at Stony Brook University.

## 4.1 Introduction

Lithium trivanadate,  $\text{LiV}_3\text{O}_8$ , and transition metal oxides in general are attractive cathode materials for lithium-ion batteries due to their moderate redox potential, high theoretical capacity, and good rate capability.<sup>1,2</sup>  $\text{LiV}_3\text{O}_8$ , as with many other transition metal oxides, undergoes phase change during lithiation.<sup>1,3,4</sup> Up to a composition of  $\text{Li}_{2.5}\text{V}_3\text{O}_8$ , the material is in the parent layered  $\alpha$ -phase; from  $\text{Li}_{2.5}\text{V}_3\text{O}_8$  to  $\text{Li}_4\text{V}_3\text{O}_8$ , the  $\alpha$ - to  $\beta$ -phase transition process takes place where the layered phase transforms into the defected rock-salt  $\beta$ -phase; beyond  $\text{Li}_4\text{V}_3\text{O}_8$ , lithiation occurs into the single  $\beta$ -phase.<sup>1,4</sup> Phase transitions during battery operation are significant because they have implications for electrochemical performance, rate capability, as well as cycle life. Previous studies have interrogated phase change using a variety of methods, both experimental and theoretical: electrochemical<sup>5-7</sup>, in-situ<sup>8,9</sup> and ex-situ<sup>10</sup> characterization (SEM<sup>7,11</sup>, XRD<sup>4,5,7,10,11</sup>), DFT<sup>9,12</sup>, and continuum modeling<sup>6</sup>.

Electrochemical measurements are commonly used to investigate battery performance. While these measurements are useful, they are indirect measurements of the physical processes that govern performance. For this reason, direct measurements through characterization, such as SEM, XRD, and TEM are used in-situ and ex-situ to try to understand the internal processes. However, because battery systems are highly dynamic, if there are even short delays between operating the battery and interrogating it, the observed profiles may not be indicative of the profiles that exist during operation. This concept is illustrated in Figure 4.1. Using the parameters listed in Table 2 and discharging at C/18 until an equivalence of  $\text{Li}_{2.4}\text{V}_3\text{O}_8$ , simulations show that even with a short gap between discharge and characterization (two hours) the spatial profiles change significantly. And if there is a 10-hour delay or more, the non-uniformities present during operation will be completely undetectable. Operando studies are therefore very valuable because they allow for characterization in time and position and show how these profiles evolve during battery operation; insights about the physical process can be gained from this characterization information. Zhang et al. used synchrotron energy dispersive X-ray diffraction (EDXRD) measurements to probe the evolution of phase change and the

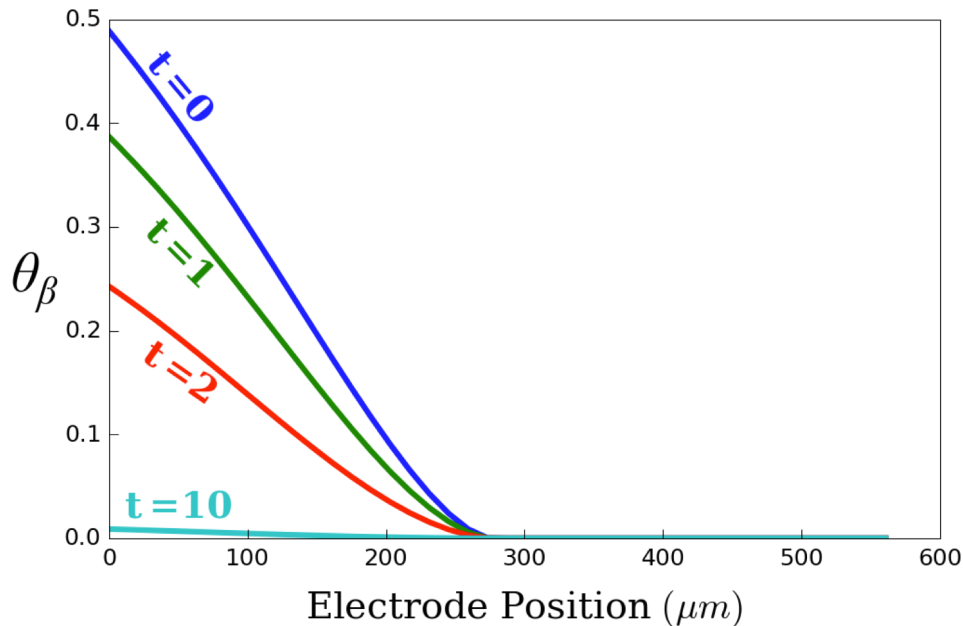


**Figure 4.1:** The volume fraction of  $\beta$ -phase in a 561  $\mu\text{m}$  thick  $\text{LiV}_3\text{O}_8$  cathode as a function of position at 0, 1, 2, and 10 hours after the end of discharge.

spatial variation of solid-state lithium concentrations within an  $\text{LiV}_3\text{O}_8$  electrode during operation.<sup>13</sup> Because the results of the operando EDXRD measurements can be difficult to interpret it is useful to couple these results with simulation studies.

A previously published crystal-scale mathematical model has been shown to be in excellent accord with electrochemical measurements and used to detail the crystal scale transport and phase change dynamics in  $\text{LiV}_3\text{O}_8$ .<sup>6</sup> The model was developed using experimental studies on cathodes with thicknesses of 50  $\mu\text{m}$ , ensuring that electrode-scale transport resistances were minimized. The agreement with electrochemical data present by Brady et al.<sup>6</sup> was compelling, however the predicted concentration profiles were not directly verified. The present study uses operando EDXRD measurements in addition to electrochemical measurements to validate the predicted concentration profiles and hypothesized phase change parameters. In the present study, a  $\sim 500$   $\mu\text{m}$  thick electrode was used in order to effectively exploit the ability of the operando method to map spatial variations as a function of time (state of charge); because the electrode used in this study was  $10\times$  thicker, electrode-scale resistances needed to be accounted for in the simulations in addition to crystal-scale transport effects. While Strobridge et al.<sup>14</sup> used a combination of operando EDXRD characterization, electrochemical measurements, and porous

electrode theory to explore the performance of  $\text{LiFePO}_4$ , this is the first study to use this combination of methods to study  $\text{LiV}_3\text{O}_8$ ; in addition, this is the first study to compare operando EDXRD measurements with a continuum model using crystal scale transport properties coupled with electrode scale transport properties and phase change kinetics based on nucleation and growth. The spatio-temporally resolved operando data provide a means to test the validity of the continuum model, especially the novel description of the phase change kinetics. Furthermore, the model provides context for quantitative interpretation of the operando data.

## 4.2 Experimental

$\text{Li}_{1.1}\text{V}_3\text{O}_8$  material was synthesized via a sol-gel approach, adapted from a previous report.<sup>15</sup> Briefly,  $\text{V}_2\text{O}_5$  and  $\text{LiOH}\cdot\text{H}_2\text{O}$  in a stoichiometric ratio ( $\text{Li}:\text{V} = 1.1:3$ ) were stirred in aqueous solution under nitrogen, dried and annealed at  $500^\circ\text{C}$  to obtain the final product, LVO500. The electrode for EDXRD measurements was prepared using LVO500, carbon and graphite in a weight ratio of 90:5:5, where the mixtures were pressed into a cylindrical electrode 561  $\mu\text{m}$  thick and radius 13 mm; the mass loading of LVO500 in the electrode was 0.124 g. A coin cell with a LVO500 electrode, Li metal anode and polypropylene separator was constructed in an argon-filled glove box. 1 M  $\text{LiPF}_6$  in ethylene carbonate/dimethyl carbonate (a volume ratio of 3:7) was used as an electrolyte. Excess electrolyte is added to the cell to ensure proper wetting. The volume of the electrolyte is usually  $\sim 150$   $\mu\text{L}$ . If the electrode is not properly wetted, during discharge, propagation of the  $\beta$ -phase throughout the entire depth of the electrode would not be observed. Since this is not the case, it is believed that the electrode is properly wetted.

The EDXRD measurements of the LVO500 coin cell were conducted at the Advanced Photon Light Source at Argon National Laboratory on Beamline 6-BM-B. The experimental setup has been published previously.<sup>16</sup> White beam radiation was focused to a final gauge volume of  $3.6 \times 0.1 \times 0.02$   $\text{mm}^3$ . Coin cells were placed on the sample stage, which was moved vertically in 20  $\mu\text{m}$  increments to acquire the EDXRD patterns

for various regions inside the cell. The germanium energy detector was set to  $2\theta = 3^\circ$ . The LVO500 cell was discharged to 1.8 V vs.  $\text{Li}/\text{Li}^+$  and charged to 3.8 V at a current rate of C/18 (20.2 mA/g) on a Maccor cycle life tester while the EDXRD patterns were continuously collected. During lithiation 9 scans were taken (scans 1 - 9), at average equivalences ( $x$  in  $\text{Li}_x\text{V}_3\text{O}_8$ ):  $x = 1.1, 1.5, 1.8, 2.0, 2.3, 2.6, 2.9, 3.2,$  and 3.5; during delithiation 10 scans were taken (scans 11 - 20), at average equivalences  $x = 3.6, 3.3, 3.0, 2.7, 2.3, 2.1, 1.8, 1.5, 1.3,$  and 1.2.

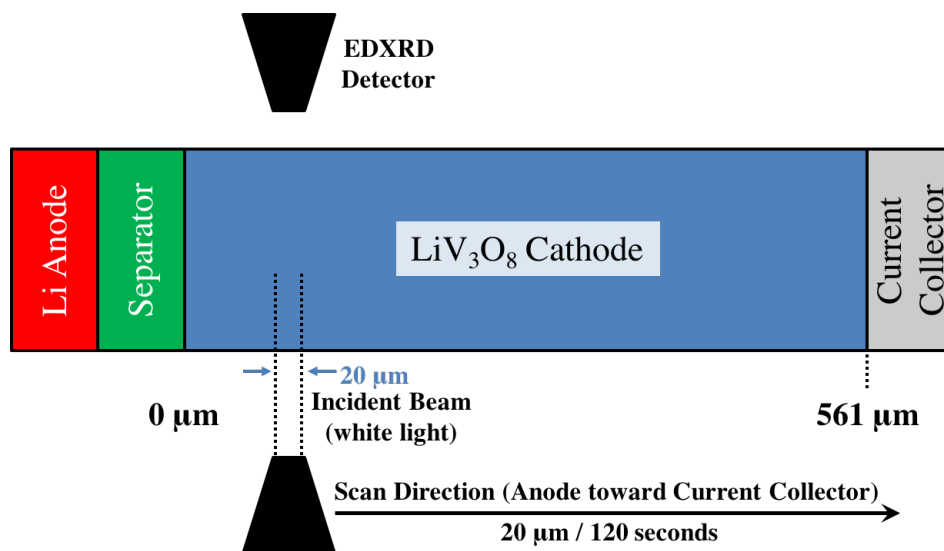


**Figure 4.2:** A schematic of the setup used for operando EDXRD measurements. White beam radiation was focused to a final gauge volume of  $3.6 \times 0.1 \times 0.02 \text{ mm}^3$ . Coin cells were placed on the sample stage, which was moved vertically in  $20 \mu\text{m}$  increments to acquire the EDXRD patterns for various regions inside the cell. The germanium energy detector was set to  $2\theta = 3^\circ$ .

Figure 4.2 is a schematic of the set-up used for the operando EDXRD measurements. The scans start at the anode and move toward the current collector. The gauge thickness is  $\sim 20 \mu\text{m}$ , and the scanning speed is 120 seconds per  $20 \mu\text{m}$ , which equals 80 minutes to scan the entire length of the  $800 \mu\text{m}$  battery.

### 4.3 Theory

The governing equations and boundary conditions used to model the system are shown in Table 1 and follow the development outlined by Knehr et al.<sup>17,18</sup> The model assumptions are identical to those outlined previously<sup>6</sup>, with a modification to assumption

|   | Units  | Symbol           | Brady, et al. <sup>6</sup>                      | Current Study                                   |
|---|--|------------------|---|---|
| <b>Electrode Scale Parameters</b>                       |  |                  |   |   |
| Electrode Porosity                                      | [cm <sup>3</sup> cm <sup>-3</sup> ]                      | $\epsilon$       | -   | 0.45  |
| Diffusion Coefficient of Li <sup>+</sup> in Electrolyte | [cm <sup>2</sup> s <sup>-1</sup> ]                       | $D_{0,eff}$      | -   | $5 \times 10^{-7}$                              |
| Solid-State Electron Conductivity                       | [S cm <sup>-1</sup> ]                                    | $\sigma$         | -   | $1.0 \times 10^{-2}$                            |
| Electrode Length  | [cm]   | $L$              | -   | 0.0561  |
| <b>Crystal Scale Parameters</b>                         |  |                  |   |   |
| Crystal Length in the [001]-direction                   | [nm]   | $L_x$            | 100   | 60  |
| Diffusion Coefficient of Li <sup>+</sup> in Solid-State | [cm <sup>2</sup> s <sup>-1</sup> ]                       | $D_{x,eff}$      | $1 \times 10^{-13}$                             | $1 \times 10^{-13}$                             |
| $\beta$ -phase Formation Reaction Rate Constant         | [cm <sup>3</sup> mol <sup>-1</sup> s <sup>-1</sup> ]     | $k_\beta$        | $5 \times 10^{-3}$                              | $4.5 \times 10^{-3}$                            |
| $\alpha$ -phase Saturation Concentration                | [mol cm <sup>-3</sup> ]                                  | $c_{\alpha,sat}$ | Li <sub>2.5</sub> V <sub>3</sub> O <sub>8</sub> | Li <sub>2.5</sub> V <sub>3</sub> O <sub>8</sub> |
| Lithium Concentration in the $\beta$ -phase             | [mol cm <sup>-3</sup> ]                                  | $c_\beta$        | Li <sub>4.0</sub> V <sub>3</sub> O <sub>8</sub> | Li <sub>4.0</sub> V <sub>3</sub> O <sub>8</sub> |
| Electrochemical Reaction Rate Constant                  | [cm <sup>5/2</sup> mol <sup>-1/2</sup> s <sup>-1</sup> ] | $k_{rxn}$        | $3.5 \times 10^{-8}$                            | $3.5 \times 10^{-8}$                            |
| Electrochemically Active Surface Area                   | [cm <sup>2</sup> cm <sup>-3</sup> ]                      | $a$              | -   | $4.8 \times 10^4$                               |

**Table 4.1:** Comparison of model parameters from previously published study and current study on the LiV<sub>3</sub>O<sub>8</sub>.

3 - concentration and potential variations on the scale of the electrode are now considered significant (in addition to variations on the crystal scale).

1. The system is isothermal.
2. The impact of intermolecular interactions on solute species transport is ignored (dilute solution theory is assumed both in the solid-state and in the electrolyte).
3. Spatial variations in concentration and potential on both the bulk electrode scale on the crystal scale are considered.
4. The LiV<sub>3</sub>O<sub>8</sub> crystals are considered to be rectangular prisms and have a constant volume.
5. The polarization associated with the lithium-metal negative electrode is negligible.
6. Only the  $\alpha$ -phase is electrochemically active. Lithium can only enter the  $\beta$ -phase by first inserting into the  $\alpha$ -phase, and then through a chemical reaction, enter into the  $\beta$ -phase.
7. In the crystal, mass-transfer along the [001] direction is assumed to be rate limiting and mass-transport along the [100] and [010] directions are considered negligible during lithiation. During delithiation, an effectively higher diffusion coefficient was

found and was hypothesized to be the result of the [100] face also being active during delithiation.<sup>6</sup>

In the present study, electrode-scale effects play a significant role in performance based on the dimensional analysis outlined by Knehr et al.<sup>17</sup> and applied by Brady et al.<sup>6</sup>. Porous electrode theory is used to describe the current in the solid-state,  $i_1$ , equation (1) in Table 1, the current in the electrolyte,  $i_2$  (Equation 2), concentration of lithium in the electrolyte,  $c_0$  (Equation 3), concentration of lithium in the solid-state,  $c_\alpha$  (Equation 4), where the current in the electrolyte and solid-state are coupled through the electrochemical reaction rate,  $i_{in}$  (Equation 6), which is described using Butler-Volmer kinetics;  $\eta$  is the overpotential for the electrochemical reaction,  $\phi_1$  is the solid-state potential, and  $\phi_2$  is the solution potential. The description of the electrochemical reaction rate and equilibrium potential,  $U$  (Equation 7) remain identical to what was published by Brady et al.<sup>6</sup> The ionic mobility of the species in the electrolyte,  $u_i$ , is assumed to follow the Nernst-Einstein relation. The governing equations associated with the electrode scale are consistent with previous simulation studies.<sup>19</sup> Although the equations were written generally, it was assumed that the values of the cationic and anionic diffusion coefficients were equal (i.e.  $D_+ = D_- = D_{0,eff}$ ).

Concentration variations within the solid-state are not neglected and are described by equation (4), based on the crystal scale model developed by Brady et al.<sup>6</sup> This equation describes the Fickian transport of lithium through the crystal and assumes that phase change proceeds through a chemical reaction. Equation (5) in Table 1 describes phase change: the process of lithium transferring between the  $\alpha$ - and  $\beta$ -phases, is assumed not to be electrochemically driven, but chemically driven, where the term  $(c_\alpha - c_{\alpha,sat})$  is the driving force for phase change and  $k_\beta$  is the kinetic rate constant. The exponent  $m$  describes the dimensionality of phase growth (planar, cylindrical, spherical) and nucleation (instantaneous, progressive), and the exponent  $p$  describes the degree of self-passivation. It is assumed that the new phase grows planarly and self-passivation is proportional to the volume fraction already transformed ( $m = 0$ ,  $p = 1$  for lithiation and  $m = 1$ ,  $p = 1$  for delithiation).

The crystal scale model development is detailed by Brady et al.<sup>6</sup> The most significant information is that the crystal is composed of three components: the  $\alpha$ -phase,  $\beta$ -phase, and grain boundaries, whose volume fractions,  $\theta_i$ , sum to 1:

$$\theta_\alpha + \theta_\beta + \theta_{gb} = 1 \quad (4.1)$$

And the volume fraction of the grain boundaries is assumed to be proportional to the volume fraction of the  $\beta$ -phase.

$$\theta_{gb} = \zeta\theta_\beta \quad (4.2)$$

where  $\zeta$  is some very small fraction (here it was assumed  $\zeta = 0.01$ ). The diffusion of lithium in the crystal is assumed to proceed through the  $\alpha$ -phase and along the grain boundaries these two diffusion pathways are in parallel:

$$D_{x,eff} = \theta_\alpha D_\alpha + \theta_{gb} D_{gb} \quad (4.3)$$

where the grain boundary diffusion coefficient,  $D_{gb}$  is  $100\times$  greater than  $D_\alpha$ . As stated in 01 - assumption 7, it was also found that the effective crystal scale diffusion coefficient,  $D_{x,eff}$ , was  $5\times$  greater during delithiation than lithiation and this was determined to be caused by an additional crystal face, the (100) face, becoming electrochemically active during delithiation. During lithiation, only the (001) face is assumed to be active, but during delithiation, both the (100) and (001) faces are assumed to be active, which facilitates the improved lithium transport in the solid-state.

### 4.3.1 Boundary and Initial Conditions

- At the beginning of operation, it is assumed that the concentration of lithium everywhere in the electrolyte is the nominal lithium ion concentration,  $c_{bulk} = 1$  M, the lithium concentration in the solid-state is equal to the nominal lithium concentration,  $c_{\alpha,0} = \text{Li}_{1.1}\text{V}_3\text{O}_8$ , and the volume fraction of  $\beta$ -phase is zero.

$$c_0|_{t=0} = c_{bulk} ; \quad c_\alpha|_{t=0} = c_{\alpha,0} ; \quad \theta_\beta|_{t=0} = \theta_{\beta,0} \quad (4.4)$$

The boundary conditions follow those outlined by Newman et al.<sup>19</sup> At the separator all the current is assumed to be carried by the ions ( $i_1 = 0$ ), the solution potential,  $\phi_2$ , is arbitrarily set to zero, and the lithium concentration in the electrolyte is assumed to be equal to the nominal concentration of lithium in the electrolyte,  $c_{bulk}$ .

$$\textbf{Separator: } i_2 = i_{applied} ; \quad \Phi_2 = 0 ; \quad c_0 = c_{bulk} \quad (4.5)$$

At the current collector, the current is carried exclusively through the solid-state ( $i_1 = i_{applied}$ ,  $i_2 = 0$ ) and there is no flux of lithium ions at the cathode/current collector interface.

$$\textbf{Current Collector: } i_1 = i_{applied} ; \quad i_2 = 0 ; \quad \nabla c_0 = 0 \quad (4.6)$$

$i_{applied}$  is the superficial current passed through the device, and is given by the total current passed through the electrode divided by the solid-state cross-sectional area.

$$i_{applied} = i_{spec} \rho_{LiV_3O_8} L \quad (4.7)$$

where  $i_{spec}$  is the mass specific current density ( $\text{mA g}^{-1}$ ).

Because the model couples the electrode and crystal-scale, boundary conditions are also needed for the crystal scale equations. The flux at the crystal surface, the (001) face, is defined by the electrochemical reaction rate at that electrode position and a symmetry condition is assumed at the crystal center.

$$D_{x,eff} \frac{\partial c_\alpha}{\partial x} \Big|_{x=L} = \frac{i_{in}}{F} \quad (4.8)$$

$$\frac{\partial c_\alpha}{\partial x} \Big|_{x=0} = 0 \quad (4.9)$$

### 4.3.2 Numerical Methods

The governing equations were discretized using the forward-time, central-space finite volume method. The scale was discretized, and the resulting block, tri-diagonal matrix was solved in Fortran 95 using the BAND(J) algorithm.<sup>20</sup> For comparison to electrochemical data, mesh sizes of 42 points on the electrode scale and 22 points on the crystal scale were sufficient. The time step was set to 1.0 second. Computer experiments were conducted for the mesh sizes and time steps to ensure convergence. For Figures 4.5 and 4.6, 202 points on the electrode scale were used to obtain a smooth prediction of the position at which the  $\beta$ -phase is present.

The crystal-scale parameters remain the same as those previously published by Brady et al.<sup>6</sup> ( $D_{x,eff} = 1 \times 10^{-13} \text{ cm}^2 \text{ s}^{-1}$ ,  $k_{rxn} = 3.5 \times 10^{-8} \text{ cm}^{5/2} \text{ mol}^{-1/2} \text{ s}^{-1}$ ,  $c_{\alpha,sat} = \text{Li}_{2.5}\text{V}_3\text{O}_8$ , and  $c_{\beta} = \text{Li}_{4.0}\text{V}_3\text{O}_8$ ), but the phase change reaction rate constant,  $k_{\beta}$ , was allowed to vary along with the solid-state electrical conductivity,  $\sigma$ , and electrolyte effective diffusion coefficient,  $D_{x,eff}$ . These parameters were fit to the experimental data using 1000 Sobol points with the bounds:  $[0.5 \times 10^{-6}, 2 \times 10^{-6}] \text{ cm}^2 \text{ s}^{-1}$ ,  $\sigma [1 \times 10^{-1}, 1 \times 10^{-5}] \text{ S cm}^{-1}$ , and  $k_{\beta} [0.1 \times 10^{-3}, 10 \times 10^{-3}] \text{ cm}^3 \text{ mol}^{-1} \text{ s}^{-1}$ . The volume of  $\text{LiV}_3\text{O}_8$  was calculated using the mass loading and the material density ( $3.5 \text{ g cm}^{-3}$ ); the density of the graphite and carbon were both taken to be  $2.26 \text{ g cm}^{-3}$ ; the porosity of the electrode,  $\epsilon$ , is calculated as the difference of the electrode volume and the volume of the active material volume, graphite, and carbon. From the 1000 Sobol points two local minima were found. A dimensionless parameter,  $K$ , describing the ratio of the electrical conductivity in the electrolyte to the electrical conductivity of the solid-state, was used to distinguish between these two sets of simulations parameters.  $K$  is defined below,

$$K = \frac{\epsilon \kappa_{0,eff}}{(1 - \epsilon) \sigma} \quad (4.10)$$

where  $\kappa_{0,eff}$  is the effective electrical conductivity of the electrolyte. One set of simulation parameters had a value of  $K < 0.15$ , which corresponds to large electronic conductivity; another set of parameters had a value of  $K = 1.0$ . It was found that low values of  $K$  were

associated with larger values of  $k_\beta$  ( $\sim 5 \times 10^{-3} \text{ cm}^3 \text{ mol}^{-1} \text{ s}^{-1}$ ) while the higher values of  $K$  were associated with lower values of  $k_\beta$  ( $< 1 \times 10^{-3} \text{ cm}^3 \text{ mol}^{-1} \text{ s}^{-1}$ ). Although simulations using either set of parameters fit the electrochemistry data well, only the  $K < 0.15$  simulations collapsed to the crystal scale model in the limits of low current rate or thin electrodes. It is believed that additional electrochemical data would also resolve the choice between the two sets of simulation parameters. In addition, as shown below, it was found that simulations with  $K < 0.1$  were consistent with operando EDXRD measurements, while simulations with  $K = 1.0$  were not.

The fitted diffusion coefficient  $D_{0,eff}$  was found to be  $5 \times 10^{-7} \text{ cm}^2 \text{ s}^{-1}$ . For the electrical conductivity of the electrode,  $\sigma$ , increasing above  $1.0 \times 10^{-2} \text{ S cm}^{-1}$  had no effect on simulated performance. From the agreement of simulation with electrochemical measurements, it has been determined that  $\sigma > 1.0 \times 10^{-2} \text{ S cm}^{-1}$ . The value of the phase change reaction rate constant was found to be  $4.5 \times 10^{-3} \text{ cm}^3 \text{ mol}^{-1} \text{ s}^{-1}$ , which is in good agreement with the previous study.<sup>6</sup>

Using the Nernst-Einstein relation, the effective conductivity of 1M LiPF<sub>6</sub> in EC/DMC was calculated to be  $4.0 \times 10^{-3} \text{ S cm}^{-1}$ , which is about 3× lower than what is experimentally observed ( $1.0 \times 10^{-2} \text{ S cm}^{-1}$ ). However, the parameters are not estimated for bulk solutions, but are estimated within the porous electrode; this means there are tortuosity effects that are not explicitly accounted for in the formulation, but are implied (hence the labeling as the effective conductivity).

Table 2 compares the parameters derived from simulating thin electrode ( $\sim 50 \text{ }\mu\text{m}$ ) electrochemical measurements against the parameters derived from this study of thick electrode ( $561 \text{ }\mu\text{m}$ ) electrochemical measurements. It should be noted that the thin-electrode material was sintered at  $550^\circ\text{C}$ , while the thick electrode material was sintered at  $500^\circ\text{C}$ . These slight differences in synthesis conditions may account for the difference in observed crystal size.

| Electrode Scale Equations               |  |   |                |                              |                   |   |
|---|--|---|----------------|------------------------------|-------------------|---|
| (1)                                     | Solid-State Current  | $(1 - \epsilon) \sigma \nabla^2 \Phi_1 - a i_{in} = 0$  | Separator      | $i_1 = 0$                    | Current Collector | $i_1 = i_{applied}$   |
| (2)                                     | Electrolyte Current ( $i_2$ )<br>Ionic Conductivity ( $\kappa$ )   | $\nabla \cdot (\kappa \nabla \Phi_2) + \epsilon F (z_+ D_+ + z_- D_-) \nabla^2 c_0 + a i_{in} = 0$<br>$\kappa = \epsilon F^2 (z_+^2 u_+ + z_-^2 u_-) c_0$   |                | $\Phi_2 = 0$                 |                   | $i_2 = 0$   |
| (3)                                     | Electrolyte Concentration ( $c_0$ )                                | $\epsilon \frac{\partial c_0}{\partial t} = \epsilon D_{0,eff} \nabla^2 c_0 + \frac{a i_{in}}{F}$   |                | $c_0 = c_{bulk}$             |                   | $N_+ = N_- = 0$   |
| Crystal Scale Equations                 |  |   |                |                              |                   |   |
| (4)                                     | Lithium Concentration<br>in the $\alpha$ -Phase                    | $\frac{\partial((\theta_\alpha + \theta_{gb})c_\alpha)}{\partial t} = D_{x,eff} \nabla^2 c_\alpha - c_\beta \frac{\partial \theta_\beta}{\partial t}$   | Crystal Center | $\nabla c_\alpha = 0$        | Crystal Edge      | $-D_{x,eff} \nabla c_\alpha = \frac{i_2^n}{F}$                                  |
|   | Solid-State Volume Fractions                                       | $\theta_{gb} = \zeta \theta_\beta$<br>$\theta_\alpha + \theta_\beta + \theta_{gb} = 1$  |                |                              |                   |   |
| (5)                                     | Balance on the<br>$\beta$ -Phase Formation ( $\theta_\beta$ )      | $\frac{\partial \theta_\beta}{\partial t} = k_\beta (c_\alpha - c_{\alpha,sat}) \theta_\beta^m [1 - \theta_\beta]$  | Lithiation     | $m = 0, p = 1$               | Delithiation      | $m = 1, p = 0$  |
| Electrochemical Reaction Rate           |  |   |                |                              |                   |   |
| (6)                                     | Current Density ( $i_{in}$ )<br>Exchange Current Density ( $i_0$ ) | $i_{in} = i_0 \left[ \exp\left(\frac{\alpha_a F \eta}{RT}\right) - \exp\left(-\frac{\alpha_c F \eta}{RT}\right) \right]$<br>$i_0 = F k_{rxn} c_0^{\alpha_a} c_\alpha^{\alpha_c} (c_{\alpha,max} - c_\alpha)^{\alpha_a}$   |                | $\eta = \Phi_1 - \Phi_2 - U$ |                   |   |
| Reversible Potential                    |  |   |                |                              |                   |   |
| (7)                                     |  | $U = U_{ref} + \frac{R_G T}{F} \ln \left[ \left( \frac{c}{c_0} \right) \left( \frac{1 - \bar{c}_{max}}{\bar{c}_{max}} \right) \right] + \sum_{k=0}^N A_k \left[ (2\bar{c}_{max} - 1)^{k+1} - \frac{2\bar{c}_{max} k (1 - \bar{c}_{max})}{(2\bar{c}_{max} - 1)^{1-k}} \right]$ |                |                              |                   | $\bar{c}_{max} = \frac{c_\alpha - c_{\alpha,0}}{c_{\alpha,max} - c_{\alpha,0}}$ |
| Parameter                               | Value  | Parameter   | Value          | Parameter                    | Value             |   |
| $c_{\alpha,max}$ (mol cm <sup>3</sup> ) | 0.0243 [Li <sub>3.0</sub> V <sub>3</sub> O <sub>8</sub> ]          | $A_5$   | 0.32144        | $A_{13}$                     | 1133.1            |   |
| $N$                                     | 20   | $A_6$   | 19.037         | $A_{14}$                     | 813.10            |   |
| $U_{ref}$                               | 2.7671   | $A_7$   | 11.997         | $A_{15}$                     | 1438.6            |   |
| $A_0$                                   | 0.32895  | $A_8$   | 107.13         | $A_{16}$                     | 568.70            |   |
| $A_1$                                   | 0.057048   | $A_9$   | 111.70         | $A_{17}$                     | 953.47            |   |
| $A_2$                                   | 0.21475  | $A_{10}$  | 355.17         | $A_{18}$                     | 237.50            |   |
| $A_3$                                   | 0.24177  | $A_{11}$  | 489.45         | $A_{19}$                     | 260.21            |   |
| $A_4$                                   | 1.8186   | $A_{12}$  | 696.86         | $A_{20}$                     | 52.050            |   |

**Table 4.2:** Governing equations and boundary conditions used to model the thick LiV<sub>3</sub>O<sub>8</sub> electrode. The crystal scale and electrochemical reaction rate equations are consistent with those reported by Brady et al.<sup>6</sup>

## 4.4 Results

Figure 4.3 compares two models - a crystal scale model and a coupled electrode/crystal scale model - to the observed electrochemical data. The published crystal scale model overpredicts the cell potential between  $x = 1.5$  and 3 ( $x$  in Li <sub>$x$</sub> V<sub>3</sub>O<sub>8</sub>), but by accounting for both electrode as well as crystal-scale effects, agreement with the electrochemical measurements is achieved. The electrode-scale model accounts for both potential losses and depletion of Li<sup>+</sup> in the electrolyte. It is observed that the thin-electrode simulation (only crystal-scale effects) shows a voltage plateau for compositions greater than Li<sub>2.5</sub>V<sub>3</sub>O<sub>8</sub>, whereas the thick electrode simulations (coupled electrode and crystal-scale effects) show

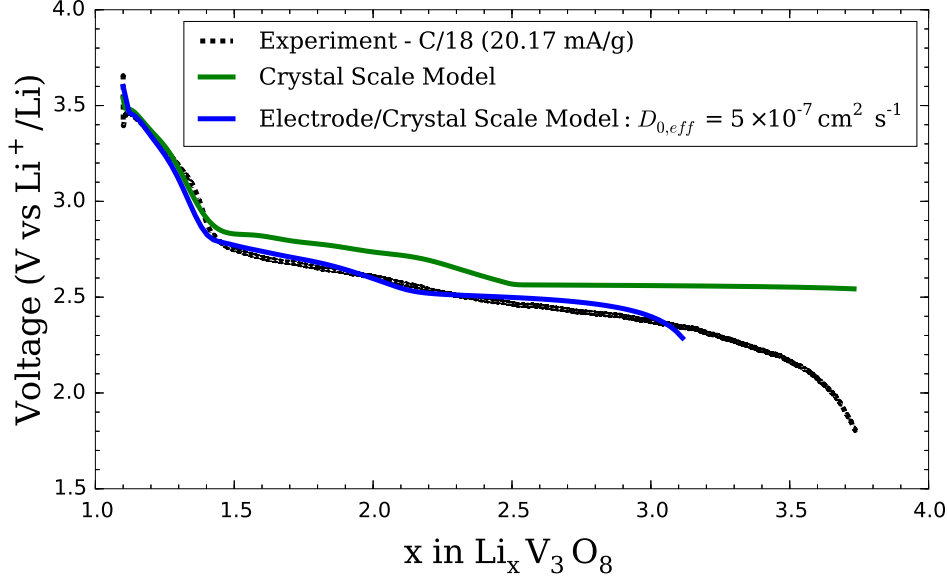


**Figure 4.3:** Cell potential of a 561  $\mu\text{m}$  thick  $\text{LiV}_3\text{O}_8$  cathode discharge data current rate of C/18. Dashed (black) lines are experimental measurements. Simulations neglecting electrode scale resistances (i.e. only modeling crystal-scale resistances) are shown in green and simulations accounting for both electrode and crystal scale resistances in blue, assuming  $\epsilon = 0.45$ .

a more sloping voltage profile. The voltage slope is primarily due to the non-uniformities in the concentration profile, which favor lithiation closer to the separator and cause the voltage to continuously decrease.

Figure 4.4 shows the simulated and measured electrochemical data; the solid circles on the simulated curve give the average equivalence ( $x$  in  $\text{Li}_x\text{V}_3\text{O}_8$ ) during each of the EDXRD scans, and the insets are the simulated concentration profiles at some selected scans. Significant spatial variations in solid-state Li concentration, with higher values near the separator are predicted. These spatial variations lead to a preferential formation of the  $\beta$ -phase near the separator, with the penetration depth of the  $\beta$ -phase increasing with state of charge.

The simulations can predict the penetration depth of the  $\beta$ -phase within the electrode, e.g. at  $x \sim 2.1$  in  $\text{Li}_x\text{V}_3\text{O}_8$  (scan 5) the penetration depth of  $\beta$ -phase is 100  $\mu\text{m}$ ,  $x \sim 2.5$  (scan 6): 240  $\mu\text{m}$ ,  $x \sim 2.7$  (scan 7): 300  $\mu\text{m}$ ,  $x \sim 3.0$  (scan 8): 400  $\mu\text{m}$ . Similarly, the EDXRD patterns can be analyzed to determine the observed penetration depth of the  $\beta$ -phase within the electrode. Figure 4.5 shows the measured penetration depth of the  $\beta$ -phase (measured from the separator) at different values of  $x$  (scan #). The vertical error bars are  $\pm 20$   $\mu\text{m}$  (the gauge thickness of each scan) and the horizontal bars

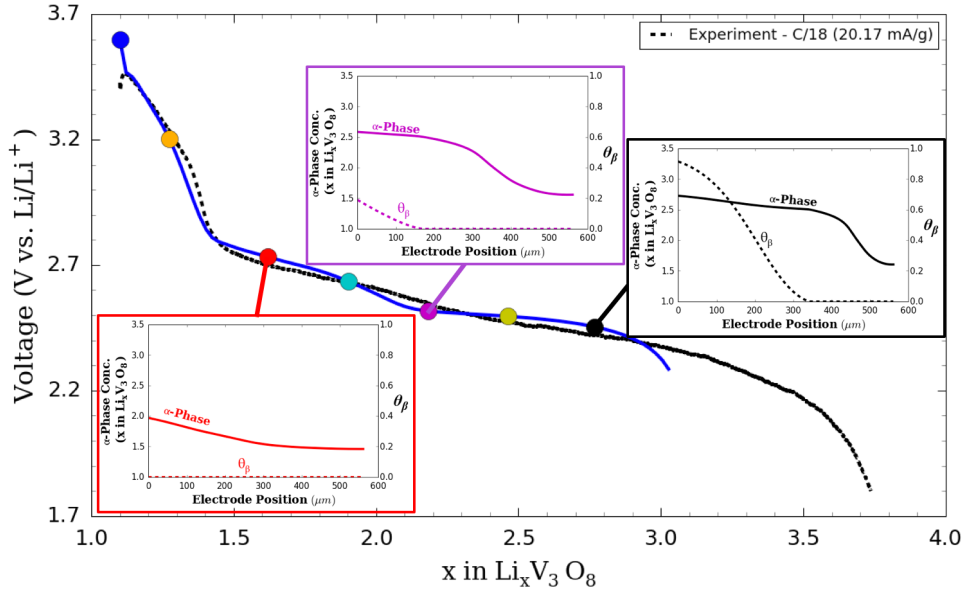


**Figure 4.4:** Simulated and experimental potential as a function of state of charge at a current rate of  $C/18$ . The points along the simulation curve correspond to the average equivalence of the EDXRD scans. The insets are model predictions for the concentration profiles of lithium in the  $\alpha$ -phase as well as the volume fraction of  $\beta$ -phase as a function of electrode position.

are  $\pm 0.007$  equivalence. The horizontal error bars arise from the simultaneous scanning and operation (i.e. discharging) of the cell. It was assumed that the interface could be determined within  $\pm 20 \mu\text{m}$ , and the variation in the equivalence is given by the time needed to scan  $40 \mu\text{m}$ .

For comparison of experiments to simulations, a detection limit for the  $\beta$ -phase is required. Here it was estimated that the minimum detectable volume fraction was  $\sim 4\%$ . The solid lines in Figure 4.5 represent the simulated penetration depth of the  $\beta$ -phase for different thresholds of detection: 0%, 5%, 10% by volume of  $\beta$ -phase. From Figure 4.5 it can be seen that the agreement of penetration depth vs. depth of discharge is largely independent of the detection limit. The agreement between EDXRD measurements and simulated predictions of the  $\beta$ -phase penetration depth using a detection limit of 5% is very good. From the combination of electrochemical measurements and operando characterization it was determined that the simulations accurately capture the physics occurring within the  $561 \mu\text{m}$  LVO electrode.

In a previous theoretical study of the  $\text{LiV}_3\text{O}_8$  electrode<sup>6</sup>, comparisons between electrochemical measurements and simulated results were used to estimate parameter values for crystal-scale transport as well as the kinetics of phase change; the operando EDXRD

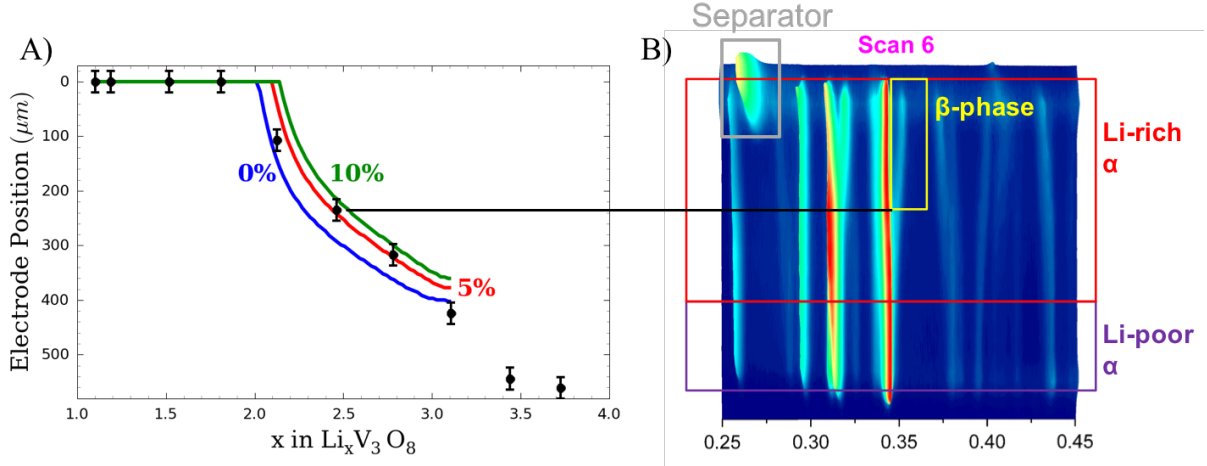


**Figure 4.5:** A) The position (measured from separator) where  $\beta$ -phase is present as a function of the state of charge. Points are determined from the EDXRD measurements and the solid lines are simulations of this interface assuming volume fractions of 0%, 5%, and 10% as the detection thresholds. B) Representative EDXRD scan illustrating how the scans were analyzed to determine the presence of  $\beta$ -phase.

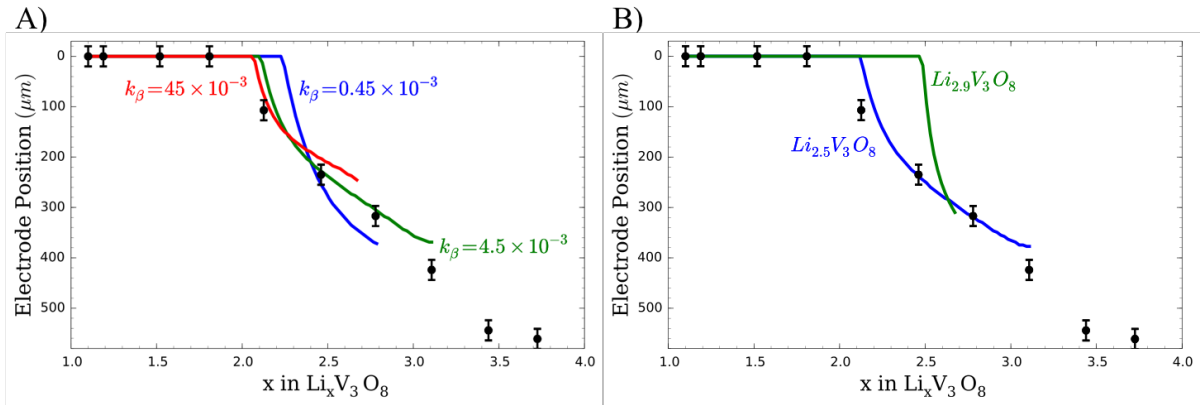


**Figure 4.6:** The position (measured from separator) where  $\beta$ -phase is present as a function of the state of charge. Points are determined from the EDXRD measurements and the solid lines are simulations of this interface. Simulations show the sensitivity of the model to phase-change kinetic parameters A)  $k_\beta$  and B)  $x_{\alpha,sat}$ , assuming a 5% volume fraction detection limit.

measurements provide another avenue to interrogate the kinetics of phase change. Equation 5 in Table 1 gives the analytical expression used to evaluate the formation of  $\beta$ -phase in the material. The two most critical kinetic parameters are the kinetic rate constant,  $k_\beta$ , and the saturation concentration,  $c_{\alpha,sat}$ . Simulations of the  $\beta$ -phase interface as a function of  $k_\beta$  are displayed in Figure 4.6A and simulations of the  $\beta$ -phase interface for different values of  $c_{\alpha,sat}$  are displayed in Figure 4.6B. In 4.6A, it can be seen that  $k_\beta = 0.45$  is inconsistent with the EDXRD data. However, distinguishing between  $k_\beta = 4.5$  and  $k_\beta = 45$  cannot be done from the operando data alone.

From the scientific literature two hypotheses have been proposed for the phase equilibria:  $\text{Li}_{2.5}\text{V}_3\text{O}_8:\text{Li}_4\text{V}_3\text{O}_8$ <sup>21,22</sup> and  $\text{Li}_{2.9-3.0}\text{V}_3\text{O}_8:\text{Li}_4\text{V}_3\text{O}_8$ <sup>1,4,23</sup>. Brady et al.<sup>6</sup> compared electrochemical measurements with simulated results to show that an equilibrium of  $\text{Li}_{2.9-3.0}\text{V}_3\text{O}_8:\text{Li}_4\text{V}_3\text{O}_8$  is inconsistent with electrochemical observations. Similarly, the operando EDXRD measurements also show that  $\text{Li}_{2.9-3.0}\text{V}_3\text{O}_8:\text{Li}_4\text{V}_3\text{O}_8$  is inconsistent with the observed phase profiles. From 6B, it can be seen that the predicted penetration depth of the  $\beta$ -phase using  $c_{\alpha,\text{sat}} = \text{Li}_{2.9}\text{V}_3\text{O}_8$  would be lower than what is experimentally observed; however, using  $c_{\alpha,\text{sat}} = \text{Li}_{2.5}\text{V}_3\text{O}_8$  the  $\beta$ -phase penetration depth agrees very well with the EDXRD measurements. These findings,  $c_{\alpha,\text{sat}} = \text{Li}_{2.5}\text{V}_3\text{O}_8$  and  $k_\beta = 4.5 \text{ cm}^3 \text{ mol}^{-1} \text{ s}^{-1}$ , are consistent with the electrochemical data from both thick ( $\sim 500 \text{ }\mu\text{m}$ ) and thin ( $\sim 50 \text{ }\mu\text{m}$ ) electrodes. While for this material,  $\text{Li}_x\text{V}_3\text{O}_8$ , the phase change parameters could be extracted from the electrochemical data, this may not be the case for all materials. Figures 4.6A and 4.6B illustrate a framework of how EDXRD data (or operando data in general) can be used in combination with simulation results as another metric to quantify physical parameters.

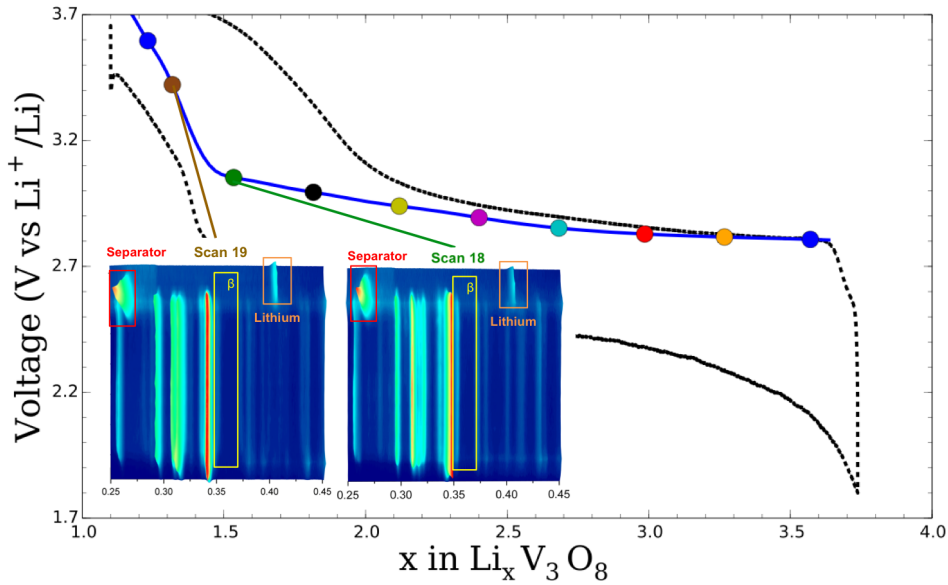


**Figure 4.7:** Simulated and experimental cell potential as a function of state of charge at a current rate of  $C/18$ . Simulations are shown as the blue solid line and experiments as the black dashed line. The points along the simulation curve indicate the average equivalence when EDXRD scans were taken during delithiation. The insets are two scans at the end of delithiation,  $x \sim 1.5$  (scan 18) and  $x \sim 1.3$  (scan 19) in  $\text{Li}_x\text{V}_3\text{O}_8$ .

Because of model limitations, as  $\theta_\beta \rightarrow 1.0$ , the simulations of lithiation cannot

reach the end of discharge capacity, at which delithiation begins. Therefore, the simulations for delithiation were seeded uniformly with  $\theta_\beta = 0.9$  ( $\text{Li}_{3.7}\text{V}_3\text{O}_8$ ); assuming uniform concentration profiles at the start of delithiation or starting delithiation immediately after lithiation produced similar results in terms of the predicted electrochemical measurements and predicted concentration profiles. It was found that simulations did not accurately predict the cell potential. By adding a constant overpotential of 150 mV to the simulations during delithiation (the blue delithiation curve in Figure 4.7), agreement is improved. In contrast, simulations and experiments are in agreement during both the lithiation and delithiation process on studies of 50  $\mu\text{m}$  electrodes without an additional overpotential during delithiation. It is possible that the larger cell potentials measured during the delithiation step in the 561  $\mu\text{m}$  electrode can be attributed to higher anodic overpotentials due to mass transfer limitations, considering that the cathodic current densities on the Li anode are  $10\times$  higher than they were for the thin electrodes.

During lithiation of the cathode, the lithium metal anode is being oxidized, and during delithiation of the cathode, lithium is being reduced. Polarization at the anode is presumably more important during delithiation of the cathode because the mass transfer overpotential associated with depleting lithium is higher than the penalty for creating excess lithium ions near the anode. Despite discrepancies in the cell potential, the model seems to be in agreement with the operando observations for the dissolution of  $\beta$ -phase during delithiation. This hypothesis for why there is a higher observed polarization during delithiation does not preclude other physical reasons for the higher observed polarization.

During delithiation, simulation results of the  $\beta$ -phase profiles were also compared to the profiles observed through operando EDXRD. In contrast to the lithiation process, during delithiation the characterization data suggest that the  $\beta$ -phase disappears uniformly across the electrode. This is interpreted from the  $\beta$ -phase peak being present across the entire electrode at  $x \sim 1.5$  (scan 18), and disappearing uniformly at  $x \sim 1.3$  (scan 19, voltage 3.4 V); scans 18 and 19 are shown in the inset of Figure 4.7, where it can be observed that the peak associated with the  $\beta$ -phase (boxed in yellow) is present across the electrode in scan 18 and completely disappears in scan 19. Simulations suggest that

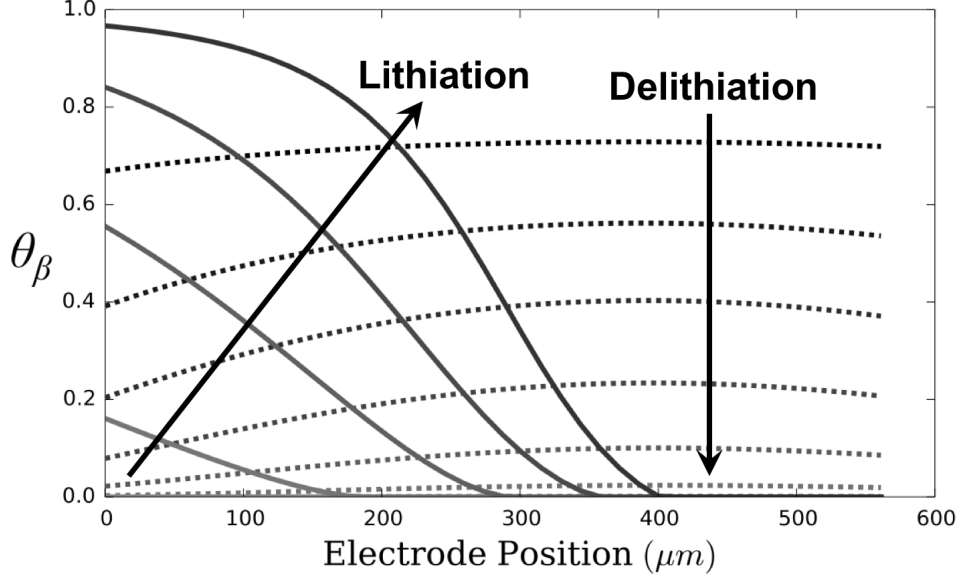


**Figure 4.8:** Simulated volume fraction of  $\beta$ -phase,  $\theta_\beta$ , as a function of electrode position (measured from separator) for an  $\text{LiV}_3\text{O}_8$  electrode 561  $\mu\text{m}$  thick and operated at a current rate of C/18. Solid lines track the evolution of the  $\beta$ -phase profile during lithiation, and dashed lines track the disappearance of the  $\beta$ -phase during delithiation.

during lithiation the  $\beta$ -phase forms heterogeneously due to mass-transport limitations - it more favorable to insert lithium near the separator, therefore  $\beta$ -phase preferentially forms near the separator.

Similar to what is hypothesized to occur at the anode, the mass transfer overpotential associated with depleting lithium near the current collector is higher than the penalty associated with creating excess lithium ions near the anode. Because of the asymmetry in the overpotentials, lithiation of the cathode occurs nonuniformly, but delithiation occurs uniformly, which is depicted in Figure 4.8.

Mass transfer resistances within the electrode lead to large concentration gradients of the lithium ion in the electrolyte during both lithiation and delithiation, as can be observed in Figure 4.9A. However, the depletion of lithium ions near the current collector ( $> 500 \mu\text{m}$ ) during lithiation has a higher penalty associated with it than the production of excess lithium ions in the electrolyte during delithiation. Using the electrolyte concentrations during lithiation and delithiation, and assuming a nominal solid-state concentration of  $\text{Li}_{1.5}\text{V}_3\text{O}_8$ , Figure 4.9B shows  $\Delta\eta$  the deviation of the positional overpotential,  $\eta$ , from the overpotential if there were no concentration variations in the electrolyte  $\eta^*$  (i.e. if  $c_0 = c_{bulk}$  everywhere;  $\Delta\eta = \eta - \eta^*$ ). From this plot it can be observed that during

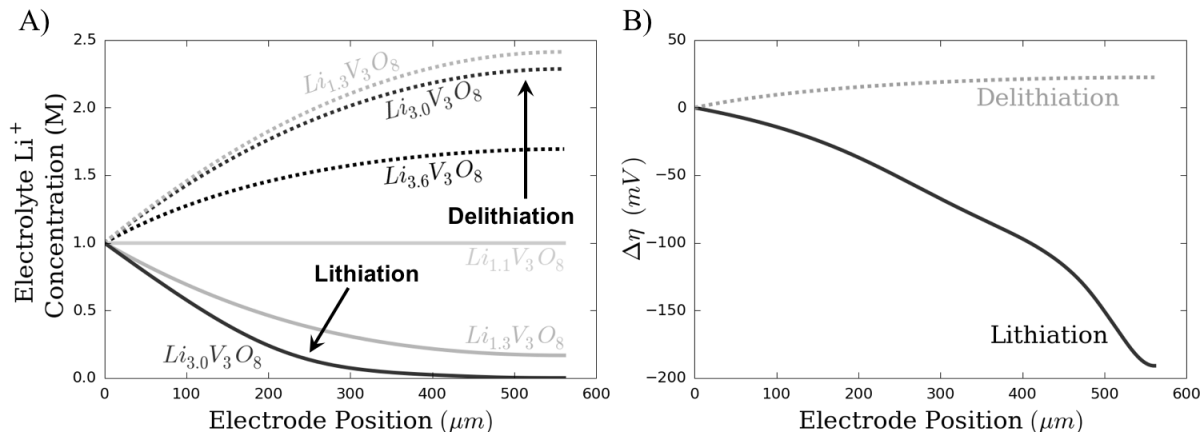


**Figure 4.9:** A) Simulated concentration profiles of Li<sup>+</sup> ions in the electrolyte for varying degrees of lithiation and delithiation. B) The deviation of the positional overpotential from the overpotential if there were no concentration variations in the electrolyte for lithiation (solid) and delithiation (dashed).

lithiation, the reduction potential of lithium is  $\sim 200$  mV lower at the current collector than at the separator, while during delithiation, the oxidization potential of lithium is only  $\sim 20$  mV higher at the current collector than at the separator. This severe asymmetry in the effect of the mass transfer resistance of Li<sup>+</sup> is a large reason for the observed asymmetry in the solid-state concentration profiles between lithiation and delithiation, and the observed asymmetry in the formation and dissolution of the  $\beta$ -phase.

## 4.5 Conclusions

EDXRD operando studies provide an important avenue to study spatial non-uniformities in phase formation and solid-state Li concentrations in LiV<sub>3</sub>O<sub>8</sub> cathodes. Properties obtained from simulation and experiment suggest relaxation of spatial non-uniformities occurs within a few hours for an electrode  $\sim 500$  μm thick. Introduction of an electrode-scale transport resistance coupled to a previously published crystal-scale model leads to an effective electrolyte porosity of 0.21 when compared to experiment. Simulations are in quantitative agreement with operando experiments in the prediction of spatial variations in  $\beta$ -phase formation. During lithiation,  $\beta$ -phase formation moves from the separator toward the current collector. During delithiation, the disappearance of  $\beta$ -phase is spatially uniform.

## 4.6 Acknowledgements

This research was supported by the Center for Mesoscale Transport Properties, an Energy Frontier Research Center supported by the U.S. Department of Energy (DOE), Office of Science, Basic Energy Sciences (BES), under award #DE-SC0012673. This research used resources of the Advanced Photon Source beamlines 6-BM, B and 10-BM, a U.S. Department of Energy (DOE) Office of Science User Facility operated for the DOE Office of Science by Argonne National Laboratory under Contract No. DE-AC02-06CH113. We acknowledge computing resources from Columbia University's Shared Research Computing Facility project, which is supported by NIH Research Facility Improvement Grant 1G20RR030893-01, and associated funds from the New York State Empire State Development, Division of Science Technology and Innovation (NYSTAR) Contract C090171, both awarded April 15, 2010.

## 4.7 Bibliography

- [1] G. Pistoia, M. Pasquali, M. Tocci, R. V. Moshtev, and V. Maner, *Journal of The Electrochemical Society*, **132**(2), 281 (1985).
- [2] Z.-K. Wang, J. Shu, Q.-C. Zhu, B.-Y. Cao, H. Chen, X.-Y. Wu, B. M. Bartlett, K.-X. Wang, and J.-S. Chen, *Journal of Power Sources*, **307**, 426 (2016).
- [3] A. Pan, J. Liu, J.-g. Zhang, G. Cao, W. Xu, Z. Nie, X. Jie, D. Choi, B. W. Arey, and S. Liang, *Journal of Materials Chemistry*, **21**, 1153 (2011).
- [4] L. A. Picciotto, K. T. Adendorff, D. Liles, and M. Thackeray, *Solid State Ionics*, **62**, 297 (1993).
- [5] M. Pasquali, G. Pistoia, V. Manev, and R. V. Moshtev, *Journal of The Electrochemical Society: Electrochemical Science and Technology*, **133**(12), 2454 (1986).
- [6] N. W. Brady, Q. Zhang, K. W. Knehr, P. Liu, A. C. Marschilok, K. J. Takeuchi, E. S. Takeuchi, and A. C. West, *Journal of the Electrochemical Society*, **163**(14), 2890 (2016).
- [7] S. Sarkar, A. Bhowmik, M. D. Bharadwaj, and S. Mitra, *Journal of The Electrochemical Society*, **161**(1), A14 (2014).
- [8] Q. Zhang, A. M. Bruck, D. C. Bock, J. Li, E. A. Stach, E. S. Takeuchi, K. J. Takeuchi, and A. C. Marschilok, *MRS Advances*, **2**(7), 401 (2017).
- [9] Q. Zhang, A. B. Brady, C. J. Pelliccione, D. C. Bock, A. M. Bruck, J. Li, V. Sarbada, R. Hull, E. A. Stach, K. J. Takeuchi, E. S. Takeuchi, P. Liu, and A. C. Marschilok, *Chemistry of Materials*, **29**(5), 2364 (2017).
- [10] S. Jouanneau, A. ã. Verbaere, and D. Guyomard, *Journal of Solid State Chemistry*, **178**, 22 (2005).
- [11] J. Xu, H. Zhang, T. Zhang, Q. Pan, and Y. Gui, *Journal of Alloys and Compounds*, **467**, 327 (2009).

- [12] T. Jiang and M. L. Falk, *Physical Review B*, **85**(245111), 1 (2012).
- [13] Q. Zhang, A. M. Bruck, D. C. Bock, J. Li, V. Sarbada, R. Hull, E. A. Stach, K. J. Takeuchi, E. S. Takeuchi, and A. C. Marschilok, *Phys. Chem. Chem. Phys.*, **19**(21), 14160 (2017).
- [14] F. C. Strobridge, B. Orvananos, M. Croft, H. C. Yu, R. Robert, H. Liu, Z. Zhong, T. Connolley, M. Drakopoulos, K. Thornton, and C. P. Grey, *Chemistry of Materials*, **27**(7), 2374 (2015).
- [15] A. C. Marschilok, S. H. Lee, C. C. Milleville, P. Chen, E. S. Takeuchi, and K. J. Takeuchi, *Journal of Composite Materials*, **47**(1), 33 (2013).
- [16] K. C. Kirshenbaum, D. C. Bock, A. B. Brady, A. C. Marschilok, K. J. Takeuchi, and E. S. Takeuchi, *Physical Chemistry Chemical Physics*, **17**, 11204 (2015).
- [17] K. W. Knehr, N. W. Brady, C. N. Lininger, C. A. Cama, D. C. Bock, Z. Lin, A. C. Marschilok, K. J. Takeuchi, E. S. Takeuchi, and A. C. West, *ECS Transactions*, **69**(1), 7 (2015).
- [18] K. W. Knehr, N. W. Brady, C. A. Cama, D. C. Bock, Z. Lin, C. N. Lininger, A. C. Marschilok, K. J. Takeuchi, E. S. Takeuchi, and A. C. West, *Journal of The Electrochemical Society*, **162**(14), A2817 (2015).
- [19] J. Newman and W. Tiedemann, *AIChE Journal*, **21**(1), 25 (1975).
- [20] J. Newman and K. E. Thomas-Alyea, *Electrochemical Systems*, John Wiley & Sons Inc., Hoboken, New Jersey, 3rd edition (2004).
- [21] G. Pistoia, M. L. Di Vona, and P. Tagliatesta, *Solid State Ionics*, **24**(2), 103 (1987).
- [22] A. Hammou and A. Hammouche, *Electrochimica Acta*, **33**(12), 1719 (1988).
- [23] J. Kawakita, Y. Katayama, T. Miura, and T. Kishi, *Solid State Ionics*, **110**, 199 (1998).

## Chapter 5

# Quantitative Parameter Estimation, Model Selection, and Variable Selection in Battery Science<sup>‡‡</sup>

---

<sup>‡‡</sup>This work has been published: Nicholas W. Brady, Christian Alexander Gould, and Alan C. West. “Quantitative Parameter Estimation, Model Selection, and Variable Selection in Battery Science.” *Journal of The Electrochemical Society* 167, (2020).

## 5.1 Introduction

Since the 1960s, the costs associated with electronic data storage, computational operations, as well as data transfer have decreased exponentially.<sup>1,2</sup> These improvements in computational performance have made simulations easier and cheaper to execute and have led to a proliferation of data generated from numerical physics-based simulations. The challenge of the future (if not already) is that there are too much data to be analyzed manually, and computationally scalable algorithms need to be developed and adopted to maintain the current pace of research; Venkatasubramanian made this observation in 2008 for the broader field of chemical engineering.<sup>3</sup> Data science techniques have enabled software programs to perform complex tasks with remarkable results.<sup>4-6</sup> However, how to apply these techniques to the fundamental study of physical processes and complex systems is not always obvious.

Numerical simulations are particularly useful when applied to complex systems such as those that arise in battery science. Numerical physical models allow for the rapid testing of hypotheses and determination of optimal design and control parameters, especially when compared to a trial-and-error process. Because of the inherent structure of batteries, models are particularly useful because they provide insights that are difficult or impossible to obtain through experimentation alone.<sup>7-12</sup> In addition to providing physical inference, models are often essential in the design of optimal control schemes. However, increasing the accessibility of fundamental physics-based battery models remains a challenge. Though commercial software tools are ubiquitous, they can be difficult to tailor to a particular system; development of a suitable model often needs to be done by a modeling expert. Most battery researchers are not modeling experts and often choose to use less rigorous, but more accessible battery models. However, the assumptions inherent in these models may only be applicable to ideal cases, therefore their link to the observed physics can be ambiguous. If, by leveraging data science techniques, a general, computationally scalable algorithm can be defined for the explicit purpose of developing numerical physics-based battery models, it would increase the accessibility of porous electrode models to all battery researchers, accelerating battery development.

Data science techniques have been applied to battery research, especially in battery state of charge and state of health estimation and battery management<sup>13–15</sup> and Dawson-Elli et al. used machine learning to build a surrogate model from a particular physics-based model in an effort to decrease execution time while retaining electrochemical accuracy.<sup>15</sup> While these applications of data science were not designed to elucidate physical processes, other papers have explored using data science techniques to elucidate physical understanding, specifically to perform physical parameter estimation by comparing well-developed models to the performance of commercial battery cells.<sup>16–18</sup> This paper describes how data science can be applied to four aspects of physics-based model development: parameter estimation, model selection, variable selection, and model-guided design of experiment.

Parameter estimation is the first step of model development after the numerical equations have been established. Modeling experts can produce compelling results by manually estimating physical parameters and systematically comparing simulated results to experimental observations.<sup>19</sup> However, because it is a trial-and-error process, manual parameter estimation is time-consuming and tedious, and often lacks a clear quantitative justification. Quantitative approaches to parameter estimation such as, parameter sampling<sup>12</sup>, least-squares<sup>20</sup> and gradient-descent have been used in the literature. However, uncertainty quantification is another important element of parameter estimation; it is not only necessary to assess model accuracy<sup>21,22</sup>, but it also necessary for optimal control<sup>23,24</sup>. Sensitivity analysis has been deployed in the literature<sup>20,25</sup>, but linearization sensitivity analysis can be inaccurate in determining uncertainty if the model is highly nonlinear.<sup>26</sup> The Markov-Chain Monte-Carlo method provides an alternative to sensitivity analysis that can be applied more generally.<sup>27,28</sup>

Sometimes hypothesis testing leads to the development of multiple physical models, so there is a need to develop a general and quantitative method to assess model performance and to discriminate between models. Statistical t-tests<sup>25</sup> have been used to assess model suitability, and statistical f-tests have been used to discriminate between models.<sup>20</sup> These two tests are good inference tools, however, these statistical tests rely

on the assumption of independent and identically distributed samples and do not give a quantification of the model’s predictive power. Cross-validation can be applied without making such strong statistical assumptions and is therefore a more general way to conduct model discrimination. By dividing the data into a training set and a validation set, cross-validation provides an empirical measure of a model’s predictive power.<sup>29</sup> This manuscript employs  $k$ -fold cross-validation, which uses a loop in which each iteration holds each data set as the validation set and the remaining  $k - 1$  data sets as the training sets.  $k$ -fold cross-validation is widely recommended when applying machine learning to real-world data.<sup>30,31</sup> While the statistical t-test and f-test may be computationally cheaper to perform, using  $k$ -fold cross-validation to compare the predictive power of several models is a computationally scalable way (or at least computationally feasible way) to perform model selection.

When it is suspected that parameter values change as a process proceeds (e.g. as a battery cycles the apparent solid-state diffusion coefficient of lithium decreases), the model can be fit to subsets of the experimental data and the parameter estimates can be tracked during the process.<sup>32</sup> This is reasonable when there are only a few parameters in the model, i.e. the model already provides good inference. However, if the model accounts for many different physical processes, there may be tens of parameters that can vary, and searching for an optimal fit in these instances becomes intractable especially if no prior knowledge is provided. One method to provide prior knowledge is to use Bayesian estimation and Bayesian priors.<sup>33</sup> Another method, covered in this paper, is to use lasso regression. Lasso regression allows for the inclusion of prior knowledge about the parameter values and provides a structured method to select the parameters that are most likely changing during the process.<sup>34</sup>

After a model has been developed from the original experiments, it may be necessary to conduct additional experiments to refine parameter estimates<sup>21,35</sup> or test a new hypothesis. Model-guided design of experiment can be used to determine which experiments and what operating conditions should be used for optimal information extraction.<sup>25,26</sup>

Brady et al.<sup>36</sup> and Knehr et al.<sup>37,38</sup> modeled the  $\text{LiV}_3\text{O}_8$  and  $\text{Fe}_3\text{O}_4$  cathodes, respec-

tively. In these studies, experts used ad hoc methods for parameter estimation, model selection, and variable selection, and the results were validated against experimental data. Herein algorithms are developed and validated by evaluating conclusions compared to those obtained by “expert” battery researchers. The sections Parameter Estimation, Model-Guided Design of Experiment, and Variable Selection compare the conclusions of the modeler and the algorithm with respect to the  $\text{LiV}_3\text{O}_8$  electrode; Model Selection compares conclusion derived from the  $\text{Fe}_3\text{O}_4$  electrode. The conclusions developed in this paper are consistent with those developed by Knehr et al.<sup>38</sup> and Brady et al.<sup>36</sup>. The advantage of the algorithmic workflow is that it allows for streamlined data analysis and decision-making and strengthens conclusions by providing quantitative justification.

## 5.2 Methods

To perform parameter estimation, a designated parameter space was sampled. To obtain confidence intervals for the estimated parameter values, a bootstrapped Markov-Chain Monte-Carlo (MCMC) algorithm was used. The advantage of using sampling instead of an iterative optimization or a sequential stochastic optimization is that the simulations can be executed in parallel. Performing MCMC with a bootstrap allows for the number of accepted points,  $m$ , and the number of simulations,  $q$ , to be independent of each other because the MCMC analysis samples the parameter space with replacement. This allows for  $m > q$ ; which means 10,000 accepted points can be achieved from 1,000 simulations and generate similar statistics to 10,000 uniquely accepted simulations.<sup>39–41</sup> (Bootstrapping means that the random sampling is done with replacement. Once a simulation result has been chosen and either rejected or accepted, it can subsequently be selected again and tested for acceptance or rejection, i.e. a selection of a simulation does not preclude it from subsequent selections; a simulation can be selected and accepted multiple times.)

The simulated voltage data were generated using the methodologies outlined by Brady et al.<sup>36</sup> and Knehr et al.<sup>37,38</sup> for the lithium trivanadate ( $\text{LiV}_3\text{O}_8$ ) and magnetite

(Fe<sub>3</sub>O<sub>4</sub>) systems, respectively. Markov-Chain Monte-Carlo analysis, cross-validation, and lasso regression were performed using code written in Python and contained in a Jupyter notebook.

### 5.2.1 Sampling

Sobol Sampling: To sample the parameter space efficiently, Sobol sequences were usually generated in up to 4-dimensions using a downloadable Python module `sobol_seq`.<sup>42</sup> `sobol_seq` takes as inputs the number of dimensions to sample as well as the number of points to generate. The points generated are in the space  $[0,1]$ , so the numbers are linearly scaled to fit the range needed for the specific parameters. A Sobol sequence is a quasi-random low-discrepancy sequence. These types of sequences are efficient for sampling through hypercubes because they efficiently fill in gaps in the hypercube, and when these points are projected onto lower dimensions, the gaps are also small.<sup>43</sup>

Lasso sampling: Because Sobol sequences produce very few points with parameter values set identically to zero, for the implementation of the Lasso method (variable selection) a grid mesh was used instead of Sobol sequences. The Lasso method regularizes the optimization problem by pushing parameter values toward zero, so it is necessary to have a fair number of points with parameter values set identically to zero.

A metric for how well the simulations emulate the experimental data is the residual sum of squares,  $RSS$ :

$$RSS = \sum_{j=1}^n (\hat{y}_j - y_j)^2 \quad (5.1)$$

where  $n$  is the number of experimental observations (the total number of voltage versus time measurements for a constant current discharge experiment),  $\hat{y}_j$  are the simulated observations and  $y_j$  are the experimental observations. Each parameter set yields an  $RSS$ , and this information is stored in a table, an example of which is shown below (Table 5.1), and used for the MCMC analysis.

| Simulation # | $D_\alpha$ ( $\times 10^{-13}$ cm <sup>2</sup> s <sup>-1</sup> ) | $k_{rxn}$ ( $\times 10^{-8}$ cm <sup>5/2</sup> mol <sup>-1/2</sup> s <sup>-1</sup> ) | Li <sub><math>x_{\alpha,sat}</math></sub> V <sub>3</sub> O <sub>8</sub> | $k_\beta$ ( $\times 10^{-3}$ s <sup>-1</sup> ) | $RSS$    |
|--------------|--|--|---|--|----------|
| 0            | 5.05   | 8.0  | 2.0   | 25.0   | 2.29791  |
| 1            | 7.525  | 7.5  | 2.5   | 12.5   | 2.87751  |
| 2            | 2.575  | 8.5  | 1.5   | 37.5   | 0.716081 |
| $\vdots$     | $\vdots$   | $\vdots$   | $\vdots$  | $\vdots$                                       | $\vdots$ |
| $q$          | 0.103625   | 8.04468  | 1.99487   | 23.5291  | 4.25133  |

**Table 5.1:** Correlation between the simulation parameters and agreement with experimental observations ( $RSS$ ) for a given applied current.

## 5.2.2 Markov-Chain Monte-Carlo

While sampling by itself gives an apparent “optimal” parameter set, it does not directly lead to statistics on the parameters<sup>12</sup>, and for this reason it is desirable to pair sampling with a Markov-Chain Monte-Carlo (MCMC) method. The MCMC method used in this paper is the Metropolis-Hastings algorithm.<sup>28,44</sup> The method uses an accept-reject criterion to find the simulations that most likely emulate the experimental observations. The accept-reject criterion approximates the experimental variation and inherent deviation between the model and the observations.

1. The algorithm is initialized by randomly picking a simulation result; this simulation’s correlated  $RSS$  value is labeled  $RSS_t$ .
2. For each subsequent iteration,  $t$ :
  - (a) Randomly choose a candidate simulation and designate its  $RSS$  value as  $RSS'$ .
  - (b) Calculate the acceptance ratio,  $\alpha = \frac{f(RSS')}{f(RSS_t)}$ , where  $f(RSS)$  is the likelihood that a particular simulation is representative of the observed experimental data.
  - (c) Accept or reject the candidate simulation based on the criteria:
    - Generate a random number,  $u$ , in the range  $[0,1]$ .
    - If  $\alpha \geq u$  then the candidate simulation is accepted and its parameter set is tabulated;  $RSS_{t+1} = RSS'$ .
    - If  $\alpha < u$  then the candidate simulation is rejected;  $RSS_{t+1} = RSS_t$ .

The likelihood,  $f$ , that a particular simulation represents the experimental obser-

vations is quantified by

$$f(\hat{y}|y, s_{exp}) = \prod_{j=1}^n \frac{1}{\sqrt{(2\pi s_{exp,j}^2)}} \exp\left(-\frac{(\hat{y}_j - y_j)^2}{2s_{exp,j}^2}\right) \quad (5.2)$$

When the experimental standard deviation is constant,  $s_{exp,j} = s_{exp}$  for all  $j$ , equation 5.2 can be simplified to

$$f(RSS, s_{exp}) = \frac{1}{(\sqrt{2\pi s_{exp}^2})^n} \exp\left(-\frac{RSS}{2s_{exp}^2}\right) \quad (5.3)$$

Results continue to be tabulated until a threshold number of accepted simulations is reached. Because the initial simulation result is randomly chosen, the initially accepted simulations may not yield an accurate distribution of likely parameters. Therefore, after the threshold acceptance number is reached, the first 10% of the selections are discarded and the remaining 90% are used to calculate the pertinent statistics.

From the accepted parameter values, the mean and variance of the parameter values are calculated from

$$\mu_P = \frac{\sum_{j=1}^m P_j}{m} \quad (5.4)$$

$$\sigma_P^2 = \frac{\sum_{j=1}^m (P_j - \mu_P)^2}{m} \quad (5.5)$$

where the  $P_j$  are the accepted parameter values and  $m$  is the total number of “undiscarded” accepted simulations. The accepted parameter values are assumed to follow a normal distribution. The mean,  $\mu_P$  is the most likely parameter value, and the standard deviation,  $\sigma_P$  is assumed to be the uncertainty in the parameter, whose value depends on the experimental variation as well as the uncertainties in the other parameter values.

### 5.2.3 Physical Model of $\text{Li}_x\text{V}_3\text{O}_8$

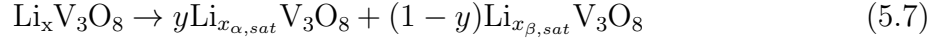
The details of the physical-based model for the  $\text{Fe}_3\text{O}_4$  cathode are given by Knehr et al.<sup>38</sup> and the details of the  $\text{LiV}_3\text{O}_8$  chemistry are given by Brady et al.<sup>36</sup> The most

pertinent details of the  $\text{LiV}_3\text{O}_8$  system are summarized here for the reader. Lithium ions combine with an electron at an insertion site to enter into the host material:



where  $\Gamma$  is an insertion site in  $\alpha$ -phase  $\text{LiV}_3\text{O}_8$ .

Phase change occurs in the material when the local lithium equivalence exceeds a threshold equivalence (or concentration),  $x_{\alpha,sat}$ . The equilibrium fractions of the  $\alpha$  and  $\beta$ -phases are given by a mass balance on the total lithium within a crystal.



$$y = \frac{x_{\beta,sat} - x}{x_{\beta,sat} - x_{\alpha,sat}} ; \quad x_{\alpha,sat} < x < x_{\beta,sat} \quad (5.8)$$

The physical model used for lithium trivanadate,  $\text{LiV}_3\text{O}_8$ , is taken from Brady et al. and summarized in Table 5.2 for the reader.<sup>36</sup>

| <b>Crystal Scale Equations</b>       |   |  |  |
|--------------------------------------|---|--|--|
| (1)                                  | Lithium Concentration<br>in the $\alpha$ -Phase ( $c_\alpha$ )  | $\frac{\partial((\theta_\alpha + \theta_{gb})c_\alpha)}{\partial t} = D_{x,eff}\nabla^2 c_\alpha - c_\beta \frac{\partial \theta_\beta}{\partial t}$ | Crystal Center<br>$\nabla c_\alpha = 0$  |
|                                      | Solid-State Volume Fractions:   | $\theta_{gb} = \zeta \theta_\beta$<br>$\theta_\alpha + \theta_\beta + \theta_{gb} = 1$   | Crystal Edge<br>$-D_{x,eff}\nabla c_\alpha = \frac{i_{app}}{F}$<br>$D_{x,eff} = D_\alpha \theta_\alpha + D_{gb} \theta_{gb}$<br>$D_{gb} = 100D_\alpha$ |
| (2)                                  | Balance on the<br>$\beta$ -Phase Formation ( $\theta_\beta$ )   | $c_\beta \frac{\partial \theta_\beta}{\partial t} = k_\beta (c_\alpha - c_{\alpha,sat}) \theta_\beta^w [1 - \theta_\beta]^v$                         | Lithiation<br>$w = 0, \quad v = 1$   |
|                                      |   |  | Delithiation<br>$w = 1, \quad v = 0$   |
| <b>Electrochemical Reaction Rate</b> |   |  |  |
| (3)                                  | Current Density ( $i_{in}$ )  | $i_{app} = i_0 \left[ \exp\left(\frac{\alpha_a F \eta}{RT}\right) - \exp\left(-\frac{\alpha_c F \eta}{RT}\right) \right]$                            | $i_{app} = i_{spec} \rho_{\text{LiV}_3\text{O}_8} L$   |
|                                      | Exchange Current Density ( $i_0$ )  | $i_0 = F k_{rxn} c_0^{\alpha_a} c_{\alpha,c}^{\alpha_c} (c_{\alpha,max} - c_\alpha)^{\alpha_a}$  | $\eta = V - U$   |
| <b>Reversible Potential</b>          |   |  |  |
| (4)                                  | $U = U_{ref} + \frac{RGT}{F} \ln \left[ \left( \frac{c}{c_0} \right) \left( \frac{1 - \bar{c}_{max}}{\bar{c}_{max}} \right) \right] + \sum_{k=0}^N A_k \left[ (2\bar{c}_{max} - 1)^{k+1} - \frac{2\bar{c}_{max}^k (1 - \bar{c}_{max})}{(2\bar{c}_{max} - 1)^{1-k}} \right]$ |  | $\bar{c}_{max} = \frac{c_\alpha - c_{\alpha,0}}{c_{\alpha,max} - c_{\alpha,0}}$  |

**Table 5.2:** Physical equations used to model the  $\text{Li}_x\text{V}_3\text{O}_8$  cathode.

## 5.2.4 Algorithmic Model Development and Analysis

Figure 5.1 depicts a flowsheet showing the connections between parameter sampling, the numerical physics-based model, and experimental measurements. Sets of tunable

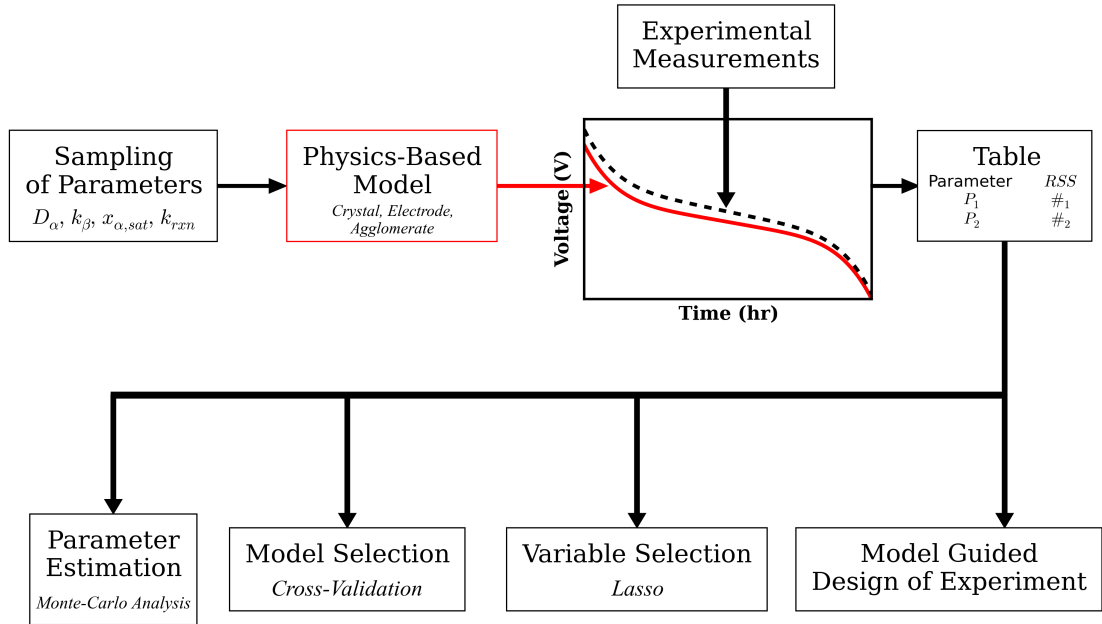


**Figure 5.1:** Flow diagram illustrating a computationally scalable framework to perform model development and subsequent analysis of the model output.

parameter values are fed to the physics-based model; for each set of parameter values simulated data are produced and compared to the experimental data and a table is constructed correlating the parameter values and a metric of the goodness of fit, such as an  $RSS$ , as shown by Table 5.1. This table of information can be used to perform parameter estimation, model selection, variable selection, and model-guided design of experiment.

## 5.3 Results and Discussion

### 5.3.1 Parameter Estimation

In 2016, Brady et al.<sup>36</sup> used current interrupt experiments (lithiation and voltage recovery) to estimate the physical parameters of the  $\text{LiV}_3\text{O}_8$  electrode. The authors estimated the solid-state diffusion coefficient,  $D_\alpha$ , exchange current reaction constant,  $k_{rxn}$ , phase change saturation equivalence,  $x_{\alpha,sat}$ , and phase change reaction rate constant,  $k_\beta$ .

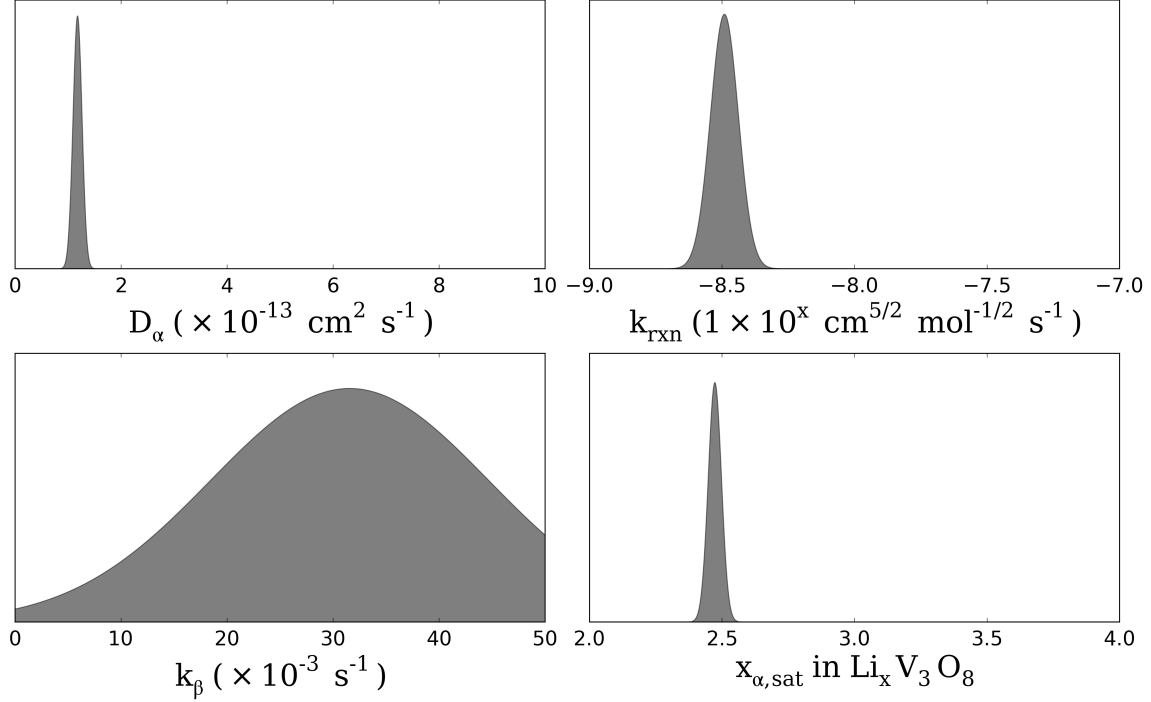


**Figure 5.2:** Physical model parameter estimates obtained from Sobol sampling followed by Markov-Chain Monte-Carlo analysis using the lithiation and voltage recovery data from all four current rates.

| Experiment | $D_\alpha$ ( $\times 10^{-13}$ cm <sup>2</sup> s <sup>-1</sup> ) | $k_{rxn}$ ( $1 \times 10^x$ cm <sup>5/2</sup> mol <sup>-1/2</sup> s <sup>-1</sup> ) | $k_\beta$ ( $\times 10^{-3}$ s <sup>-1</sup> ) | Li <sub><math>x_{\alpha,sat}</math></sub> V <sub>3</sub> O <sub>8</sub> |
|------------|--|---|--|---|
| C/10       | $0.5 \pm 0.1$  | $-7.7 \pm 0.2$  | $6 \pm 10$                                     | $2.48 \pm 0.02$   |
| C/5        | $1.1 \pm 0.1$  | $-8.5 \pm 0.1$  | $40 \pm 13$                                    | $2.48 \pm 0.02$   |
| C/2        | $1.2 \pm 0.2$  | $-8.5 \pm 0.1$  | $31 \pm 12$                                    | $2.45 \pm 0.02$   |
| 1C         | $1.8 \pm 0.2$  | $-8.7 \pm 0.2$  | $25 \pm 15$                                    | $3.1 \pm 0.6$   |
| Overall    | $1.2 \pm 0.1$  | $-8.5 \pm 0.1$  | $31 \pm 13$                                    | $2.47 \pm 0.03$   |

**Table 5.3:** The estimated mean and standard deviation for the physical parameters as a function of applied current, as well as the estimates and standard deviations derived using all rates.

Using the values  $D_\alpha = 1 \times 10^{-13}$  cm<sup>2</sup> s<sup>-1</sup>,  $k_{rxn} = 3 \times 10^{-8}$  cm<sup>5/2</sup> mol<sup>-1/2</sup> s<sup>-1</sup>,  $x_{\alpha,sat} = \text{Li}_{2.5}\text{V}_3\text{O}_8$ , and  $k_\beta = 5 \times 10^{-3}$  s<sup>-1</sup>, the numerical simulations produced compelling agreement with the experimental observations.<sup>36</sup> Figure 5.2 shows the parameter estimates derived from all the rate data during lithiation and voltage recovery and sampling using Sobol sequences in the ranges  $[0.1, 10] \times 10^{-13}$  cm<sup>2</sup> s<sup>-1</sup>,  $[-7, -9]$  for  $1 \times 10^x$  cm<sup>5/2</sup> mol<sup>-1/2</sup> s<sup>-1</sup>,  $[2.1, 4.0]$  for Li <sub>$x_{\alpha,sat}$</sub> V<sub>3</sub>O<sub>8</sub>, and  $[0, 50] \times 10^{-3}$  s<sup>-1</sup>, ( $D_\alpha$ ,  $k_{rxn}$ ,  $x_{\alpha,sat}$ , and  $k_\beta$ , respectively) - 4096 Sobol points were generated, followed by MCMC analysis assuming a uniform experimental standard deviation of 100 mV,  $s_{exp} = 100$  mV and taking 10,000 acceptances. It can be seen that the estimates produced by the algorithm are in good agreement with the estimates derived by Brady et al.<sup>36</sup> Figure 5.2 and Table 5.3 show

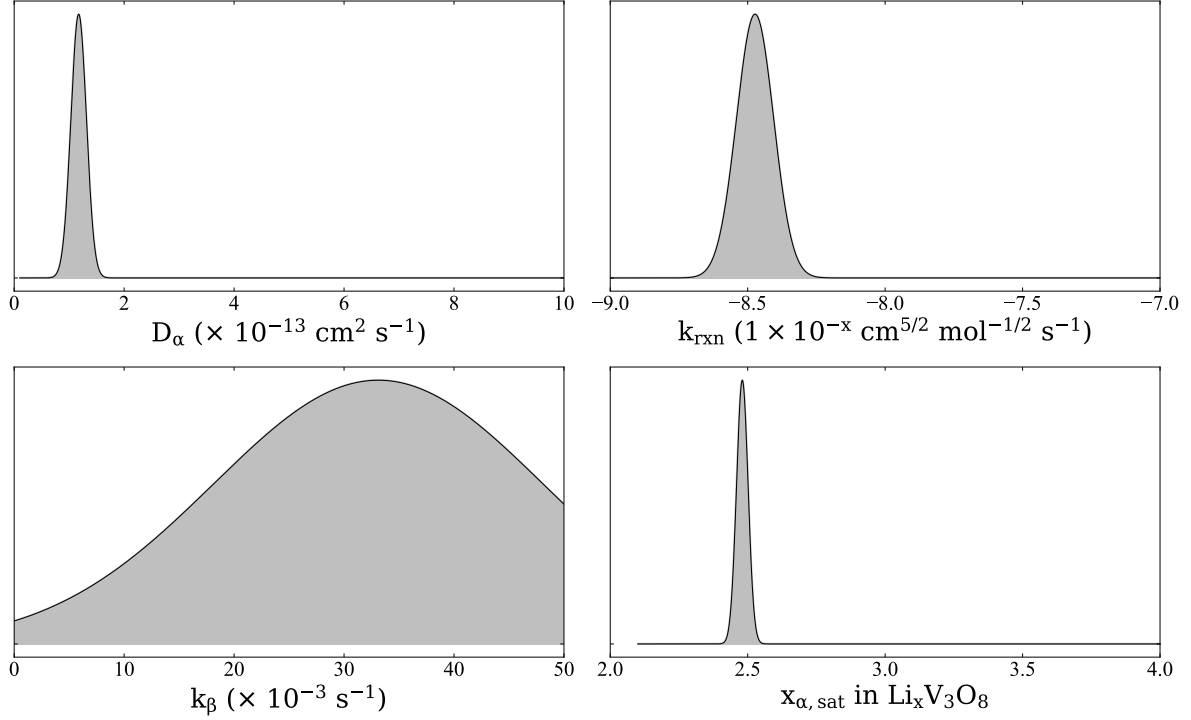


**Figure 5.3:** Physical model parameter estimates obtained from Sobol sampling calculation of the likelihood of the parameter values using equation 5.3. The comparison with 5.2 shows that the derived parameter estimates are identical. This indicates that this simpler, more efficient method can be used in place of MCMC after Sobol sampling to obtain identical results.

that some parameters can be estimated with high confidence even if other parameters have high uncertainty. This is important because during manual parameter estimation, the “expert” sometimes has to use their judgement to determine which parameters are known confidently and which are not.

The experimental standard deviation,  $s_{exp}$ , has an effect on the estimated parameter distribution. This is illustrated in Figure 5.4. Examining only the C/10 lithiation data and assuming a uniform estimate for the experimental standard deviation of 100 mV,  $s_{exp} = 100$  mV, the estimated distribution of the solid-state diffusion coefficient,  $D_\alpha$ , is  $\mu_{D_\alpha} = 0.4 \times 10^{-13} \text{ cm}^2 \text{ s}^{-1}$ , with a standard deviation of  $\sigma_{D_\alpha} = 0.04 \times 10^{-13} \text{ cm}^2 \text{ s}^{-1}$ . From Figure 5.4A, it is clear that using a uniform experimental standard deviation of 100, 50, or 20 mV gives nearly identical estimates of the parameter distribution. If the empirically determined standard deviation, which varies as a function of  $x$  in  $\text{Li}_x\text{V}_3\text{O}_8$ , is used (given as the inset in Figure 5.4A) a different distribution is achieved with  $\mu_{D_\alpha} = 0.7 \times 10^{-13} \text{ cm}^2 \text{ s}^{-1}$ , and  $\sigma_{D_\alpha} = 0.1 \times 10^{-13} \text{ cm}^2 \text{ s}^{-1}$ . The derived mean and standard deviation in

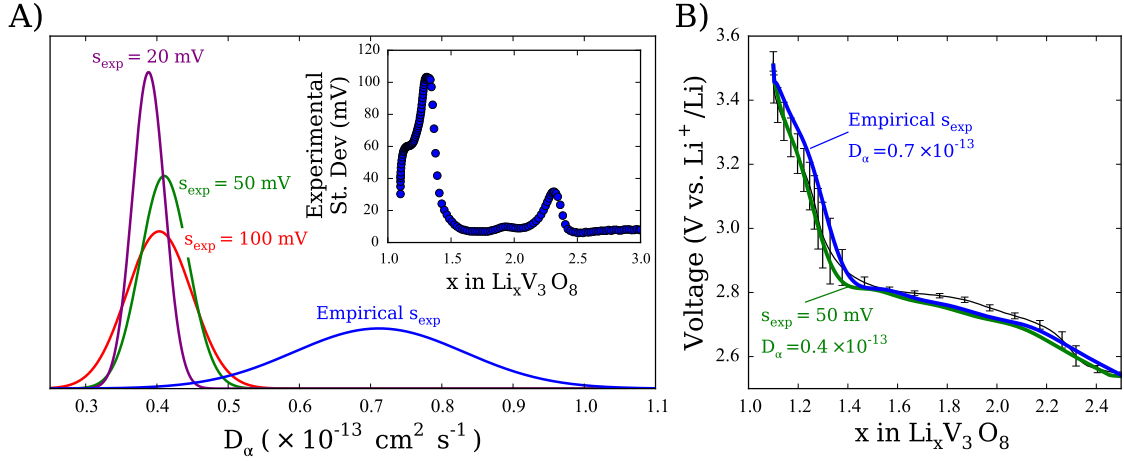


**Figure 5.4:** A) Parameter distribution estimates for the solid-state diffusion coefficient,  $D_\alpha$ , obtained from the lithiation data at C/10 using two different estimates of the experimental standard deviation: uniform estimates of  $s_{exp} = 100$ , 50, and 20 mV, and an empirically determined estimate, which is shown as the inset. B) Comparison of the simulated data with parameter estimates from assuming  $s_{exp} = 50$  mV (green) and parameter estimates from using the empirically calculated deviation (blue). The C/10 lithiation data are shown in black; the error bars show the experimental deviation.

diffusion coefficient show significant discrepancies, highlighting the importance in quantifying experimental variance as a function of state of charge. Furthermore, the value in inferred diffusion coefficients in both cases differ from estimates in Table 5.3, showing the importance in the choice of the experimental conditions in obtaining parameter estimates. Figure 5.4B shows comparisons of simulated data using parameter estimates derived by assuming  $s_{exp} = 50$  mV and using an empirical estimate of  $s_{exp}$ . While both simulations provide good fits to the experimental data, the comparison illustrates the important information obtained by using the empirical  $s_{exp}$ .

It should be noted that this current rate, C/10, is low and it is typically not advisable to extract kinetic information from experiments that do not stress the kinetics. However, lithiation data (not voltage recovery data) at C/10 were the only experimental condition for which replicate experimental data were available and therefore the only condition for which an empirical  $s_{exp}$  could be calculated. The conclusion of this observation is that experiments should be done at least in duplicate to allow for the determination of the experimental variance and, when possible, the empirically observed variance should be used to inform the parameter estimates. Figure 5.4 also suggests that if data from

duplicate experiments are not available, or if replicate data are infeasible to collect, an estimated constant value of the experimental deviation may yield realistic parameter estimates.

The parameter distributions at different current rates are also informative. For instance, as shown in Table 5.3, the experimental measurements at 1C do not inform the values of the parameters that govern phase change,  $x_{\alpha,sat}$  and  $k_{\beta}$ . This makes sense because the voltage plateau indicative of a phase change is not observed during these experiments; i.e. these experiments do not inform phase change because they do not probe phase change. For the lower discharge rates, the parameter distributions for  $x_{\alpha,sat}$  seem to be independent of rate.

The other three parameters,  $D_{\alpha}$ ,  $k_{rxn}$ ,  $k_{\beta}$ , are kinetic parameters. Intuition indicates that, all things being equal, higher current rates are better for discerning kinetic processes; however, there are practical limits to the maximum current. Though higher current rates might reveal more information about  $k_{\beta}$ , currents that are too high are unable to probe phase change before the experimental cutoff conditions are reached. Finding the maximum current rate that gives sufficient information, implies there is an optimum condition. Table 5.3 shows that some experimental conditions provide more precise insights into parameter values than other conditions. Finding the optimal experimental conditions is explored more thoroughly in the section Model-Guided Design of Experiment.

### 5.3.2 Model Selection

It is common in battery studies to have multiple competing hypotheses about the physics that are dictating battery performance; different assumptions lead to different models. This section illustrates how data science approaches can be used to algorithmically perform model selection by quantitatively identifying which model is statistically most consistent with experimental data. Such approaches allow for an unbiased evaluation of the efficacy of alternative modeling hypotheses. The results of these approaches are not purely numerical, but contain physical insights.

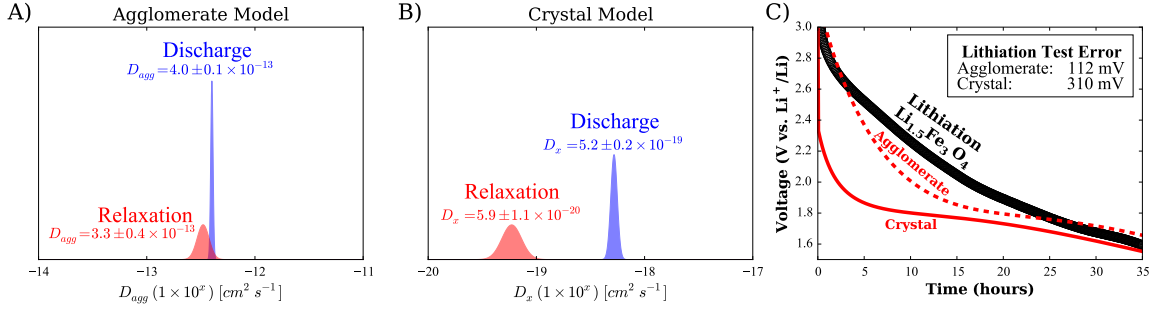


**Figure 5.5:** A) The MCMC determined distributions of the diffusive mass-transfer coefficient  $D_{agg}$  for the agglomerate scale model and B) the MCMC determined distributions of the solid-state mass-transfer coefficient,  $D_x$ , for crystal scale model. The parameters were determined using discharge data (blue) as well voltage recovery data (red). C) Comparisons of the simulated data using the mass-transfer coefficients determined by fitting each model to the relaxation data. The inset shows the average test error per experimental lithiation data point.

For the magnetite electrode,  $\text{Fe}_3\text{O}_4$ , Knehr et al.<sup>37,38</sup> showed through voltage recovery data that for small crystal sizes of 6 and 8-nm, it was not solid-state transport that dominated performance, but transport through the crystal aggregate structures, or agglomerates, that dominated performance. The authors reached that conclusion by observing that the solid-state diffusion coefficient necessary to replicate the observed voltage recovery times was very small, but when using that same diffusion coefficient during the discharge experiments, the simulations produced significant deviation from the observed electrochemical measurements. However, using an agglomerate model, the mass transfer coefficient necessary to emulate the voltage recovery data also produced reasonable agreement with the discharge data. While this paper does not contest the conclusions of the previous work, it does seek to understand how these conclusions can be developed algorithmically.

One method to perform model selection quantitatively is cross-validation.<sup>45</sup> Cross-validation requires the experimental data to be divided into a training set, by which the parameters are tuned, and a testing set, to validate the tuned parameters. Because the data come from current interrupt experiments, it can intuitively be divided into discharge data, when the current is on, and voltage recovery data, when the current is off.

$\text{Fe}_3\text{O}_4$  electrodes composed of 8-nm crystals were lithiated at a rate of C/200 (4 mA/g) to three different equivalences:  $\text{Li}_{0.5}\text{Fe}_3\text{O}_4$ ,  $\text{Li}_{1.0}\text{Fe}_3\text{O}_4$ , and  $\text{Li}_{1.5}\text{Fe}_3\text{O}_4$ ; upon reach-

ing the threshold equivalence, the cell current was turned off and voltage measurements continued to be made up to 100 hours of total test time. The data are divided into two sets: lithiation (current on) and voltage recovery (current off). One set is labeled the training set, by which the mass-transfer diffusion coefficient is fit; the other set is labeled the validation set by which the trained model is tested, and the testing error is recorded. Then the training and testing data are switched and the testing errors are summed; this is done for both models. For the agglomerate model, 256 Sobol points were generated in the range  $[-14, -11]$  for  $1 \times 10^x \text{ cm}^2 \text{ s}^{-1}$  for  $D_{agg}$ , and for the crystal scale model, 256 Sobol points were generated in the range  $[-20, -17]$  for  $1 \times 10^x \text{ cm}^2 \text{ s}^{-1}$  for  $D_x$ . It was found that the agglomerate model tested significantly better than the crystal model in cross-validation, *c.f.* Figure 5.5.

Figure 5.5 shows the MCMC determined distributions (using 10,000 accepted points for both models) for the mass-transfer coefficient for the agglomerate and crystal models when fitted to the discharge data and the voltage recovery data; the experimental deviation is assumed to be 50 mV,  $s_{exp} = 50 \text{ mV}$ . (The experimental data were examined from Knehr et al.<sup>37</sup> in the range  $\text{Li}_{0.0}\text{Fe}_3\text{O}_4$  to  $\text{Li}_{1.5}\text{Fe}_3\text{O}_4$  and it was observed that the experimental standard deviation in that range during lithiation was almost entirely below 40 mV; experimental standard deviation during voltage recovery could not be calculated empirically because there were not replicate data.) It can be seen that for the agglomerate model, the MCMC results for each partition are quite comparable,  $4.0$  and  $3.3 \times 10^{-13} \text{ cm}^2 \text{ s}^{-1}$ , while for the crystal scale model, the mass transfer coefficients differ by an order of magnitude,  $\sim 5 \times 10^{-19}$  and  $\sim 5 \times 10^{-20} \text{ cm}^2 \text{ s}^{-1}$ . The improved precision provided by the agglomerate model as well as the improved testing error both indicate that the agglomerate model is more consistent with the observed electrochemical measurements.

Cross-validation provides a clear methodology to rigorously perform model discrimination in a general way and provides the expert researcher with a quantitative justification; these measures allow for the model development process, specifically the evaluation of competing hypotheses, to be streamlined.

### 5.3.3 Variable Selection

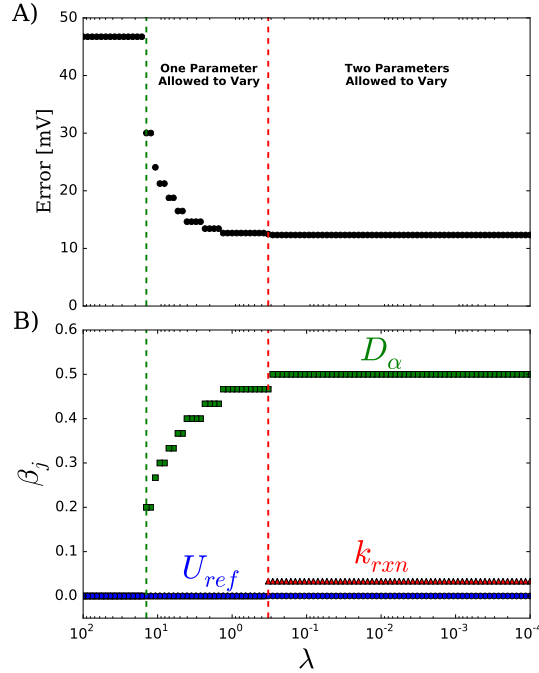


**Figure 5.6:** A) The average deviation per observation between the simulations and experiments versus the value of  $\lambda$ . B) The optimum values of  $\beta_j$  versus the value of  $\lambda$ . The vertical dashed lines indicate the value of  $\lambda$  where an additional parameter is allowed to vary (an additional  $\beta_j \neq 0$ ). A grid mesh of  $13 \times 13 \times 13$  was constructed and the  $\beta_j$ 's were allowed to vary from  $[0, 1]$  for each parameter.

The situation arises where a physical model explains existing experimental data, but fails to adequately describe new observations. In such cases, it may be necessary to select new parameter values or to develop a new model. It may be desirable to initially focus on selecting new parameter values. This section illustrates how data science approaches can be used to systematically identify statistically significant parameter variation.

For the  $\text{LiV}_3\text{O}_8$  electrode, using the physical parameters,  $D_\alpha = 1.0 \times 10^{-13} \text{ cm}^2 \text{ s}^{-1}$ ,  $k_{rxn} = 3 \times 10^{-8} \text{ cm}^{5/2} \text{ mol}^{-1/2} \text{ s}^{-1}$ ,  $k_\beta = 5.0 \times 10^{-3} \text{ s}^{-1}$ ,  $x_{\alpha,sat} = \text{Li}_{2.5}\text{V}_3\text{O}_8$ , Brady et al. achieved excellent agreement between simulations and experiments during lithiation and voltage recovery.<sup>36</sup> However, during delithiation, simulations using the aforementioned physical parameters significantly differed from the experimental observations. Brady et al. concluded that during delithiation, mass transport of lithium in the solid-state was more facile than during lithiation.<sup>36</sup> The authors came to this conclusion because accurate agreement between simulation and experimental observation was achieved by increasing

the value of the diffusion coefficient by a factor of 5,  $D_\alpha = 5.0 \times 10^{-13} \text{ cm}^2 \text{ s}^{-1}$ . The excellent agreement could *only* be achieved by changing the parameter associated with mass transport. Changing the exchange current density or changing the reaction rate constant for phase change did not improve agreement.

Again, this paper does not question the conclusions of the previous work, but seeks to explore if an algorithmic approach can come to the same or a similar conclusion. Because the values of the parameters during lithiation are already validated, and physical intuition and experience indicate that *most* of these parameters likely do not change during delithiation, the implied question is: what is the minimum number of parameters that need to be adjusted to improve agreement?

Regularization is a method to optimize a problem (achieve the best fit) while also providing additional constraints. Lasso regression regularizes the optimization problem as well as performs variable selection.<sup>34,46</sup> This method performs variable selection by only allowing the parameters that most significantly improve agreement to vary; parameters that do not significantly contribute toward improved agreement are not allowed to vary, i.e. they assume their lithiation values. Lasso performs variable selection mathematically by placing a penalty on non-zero parameters. If the parameter values during delithiation are defined in terms of their values during lithiation:

$$P_{j,delithiation} = P_{j,lithiation} \times 10^{\beta_j} \quad (5.9)$$

it is observed that  $\beta_j = 0$  produces no difference between the lithiation and delithiation parameter values. The lasso objective function introduces a bias to minimize changes in the parameters:

$$Lasso = RSS + \lambda \sum_{j=1}^N |\beta_j| \quad (5.10)$$

where the *RSS* is calculated according to equation 5.1. The additional parameter,  $\lambda$ , weights how significantly the model is constrained; high values of  $\lambda$  force all  $\beta_j$  to 0, which returns the lithiation model, while small values of  $\lambda$  give the ordinary *RSS* objective

function - all parameters are allowed to vary without constraint. Figure 5.6 shows how the parameter values (for mass transfer -  $D_\alpha$ , charge-transfer -  $k_{rxn}$ , and the thermodynamic potential -  $U_{ref}$ ) and the agreement between simulations and electrochemical observations vary as the penalty,  $\lambda$ , varies. The vertical dashed lines denote the regions where (from left to right) no parameters, one parameter, then two parameters vary. Figure 5.6 shows that almost all of the reducible error during delithiation is achieved by increasing the diffusion coefficient and only a small amount of the error is reduced by varying the exchange current density. In addition, immediately before two parameters are allowed to vary, the optimal value of the solid-state diffusion coefficient is  $D_\alpha = 3.2 \pm 0.4 \times 10^{-13} \text{ cm}^2 \text{ s}^{-1}$ , which is in good agreement with the previous study.<sup>36</sup> Figure 5.6 suggests that the lasso method is a useful tool in identifying physical changes in battery systems; the lasso method may also be a general tool that can be applied to investigate changes that occur between charge and discharge, during cycling, through temperature changes, etc.

As in the Model Selection section, the utility of a variable selection framework is to provide researchers with rigorous quantitative justification for conclusions. In addition, utilizing the lasso method allows researchers to simultaneously interrogate many parameters in various combinations, instead of having to change each parameter individually, or in a sequential combinatorial fashion. These aspects of lasso regression allow for another process of model development, variable selection, to be streamlined and performed systematically.

The previous sections have shown how to use quantitative and algorithmic approaches to perform parameter estimation, model selection, and variable selection. After gathering insights from these processes it may be desirable or even necessary to validate the conclusions with additional experiments; sometimes it is not clear which experiments to perform. The next section illustrates how these quantitative approaches can be used to guide experimental design.

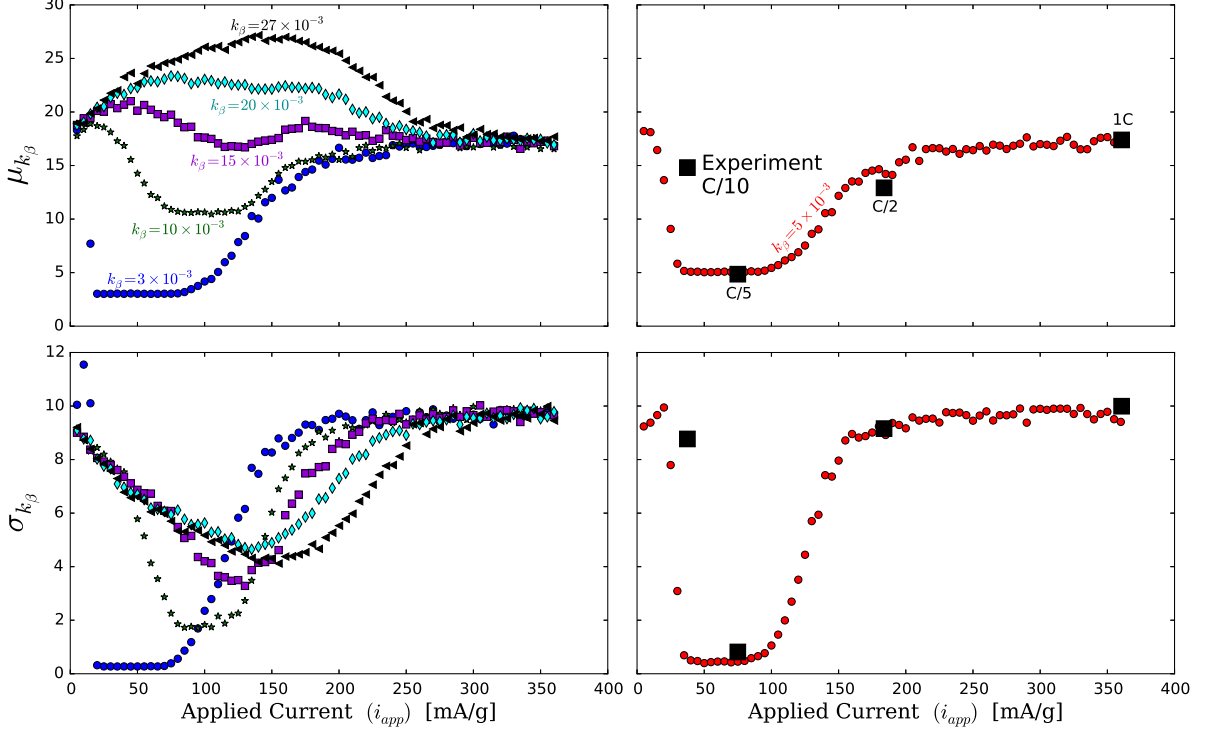


**Figure 5.7:** The left two plots show, for given true values of  $k_\beta$ , how the estimated value of  $k_\beta$ ,  $\mu_{k_\beta}$ , and the uncertainty in the estimation,  $\sigma_{k_\beta}$ , vary for different applied currents. The right two plots show, for  $k_\beta = 5 \times 10^{-3} \text{ s}^{-1}$  (red), how the apparent value,  $\mu_{k_\beta}$ , and uncertainty,  $\sigma_{k_\beta}$ , vary for different applied currents. These data are overlaid with the estimated value and uncertainty of  $k_\beta$  derived from four current rates: C/10, C/5, C/2, 1C.

### 5.3.4 Model Guided Design of Experiment

In the Parameter Estimation section, the value of the phase change reaction rate constant,  $k_\beta$ , could not be determined precisely. So the question is: what experimental conditions, specifically what constant current lithiation rate, would allow a precise determination of  $k_\beta$ ? To answer this question, simulations are used to generate mock experimental data, and the sampling and MCMC analysis are used to show which experimental conditions minimize parameter uncertainty.

In the previous sections, simulated data are compared against experimental data to generate an  $RSS$  (equation 5.1). In this section, sampled simulated data are compared to mock experimental data; the  $y_{j,mock}$  are the mock experimental observations and the  $\hat{y}_j$  are the simulated observations; for clarity this is given in the following equation:

$$RSS = \sum_{j=1}^n (y_{j,mock} - \hat{y}_j)^2 \quad (5.11)$$

It is important to note that the mock experimental observations,  $y_{j,mock}$ , are a function of  $k_{\beta,TRUE}$ , i.e.  $y_{j,mock} = f(k_{\beta,TRUE})$ .

For simplicity it is assumed that  $D_{\alpha}$ ,  $k_{rxn}$ , and  $x_{\alpha,sat}$  are known with exact precision:  $D_{\alpha} = 1 \times 10^{-13} \text{ cm}^2 \text{ s}^{-1}$ ,  $k_{rxn} = 3 \times 10^{-8} \text{ cm}^{5/2} \text{ mol}^{-1/2} \text{ s}^{-1}$ ,  $x_{\alpha,sat} = \text{Li}_{2.5}\text{V}_3\text{O}_8$ , and only lithiation data are used for parameter estimation (voltage recovery data are not used); this is a simplified case of the parameter estimation reported in Table 5.3 and Figure 5.2. A mock experiment is generated using a specific applied current, and a value of  $k_{\beta} = k_{\beta,TRUE}$ . Sampling simulations are conducted in the range inferred from existing experiments,  $k_{\beta} = [0, 30] \times 10^{-3} \text{ s}^{-1}$  using 50 Sobol points, and a table is constructed correlating  $k_{\beta}$  (sampled) with  $RSS$ , equation 5.11. Using MCMC analysis,  $\mu_{k_{\beta}}$  and  $\sigma_{k_{\beta}}$  are determined for a specific value of  $k_{\beta,TRUE}$  at a specific applied current.

Using five different values of  $k_{\beta,TRUE} = 3, 10, 15, 20, 27 \times 10^{-3} \text{ s}^{-1}$ , constant current lithiation mock experiments were run at varying current rates (5, 10, 15,  $\dots$ , 360 mA/g), with a cutoff potential 2.4 V or a cutoff equivalence of  $\text{Li}_{3.0}\text{V}_3\text{O}_8$ . Then the parameter estimation framework (sampling followed by MCMC analysis) was applied at every current rate for each value of  $k_{\beta,TRUE}$  and the results are shown in Figure 5.7. The left two plots of Figure 5.7 show the inferred values of  $k_{\beta}$  - the mean,  $\mu_{k_{\beta}}$ , and standard deviation,  $\sigma_{k_{\beta}}$ , derived from sampling combined with MCMC analysis, assuming  $s_{exp} = 50 \text{ mV}$ . These inferred values are plotted as a function of the applied current rate. Assuming the optimum maximizes precision, i.e. minimizes  $\sigma_{k_{\beta}}$ , an optimal current range is found for each value of  $k_{\beta,TRUE}$ .

This method can be applied to a hypothetical example where the phase change reaction rate constant has an estimated value and confidence interval of  $k_{\beta} = 15 \pm 12 \times 10^{-3} \text{ s}^{-1}$ . Using the mean of this range, the information on the left of Figure 5.7 indicates the optimal current rate would be 125 mA/g. If  $k_{\beta,TRUE} = 5 \times 10^{-3} \text{ s}^{-1}$ , algorithmic analysis of experimental data would reveal a new estimated value and confidence interval,  $k_{\beta} = 7.5 \pm 3 \times 10^{-3} \text{ s}^{-1}$ . If it is desired to achieve more precision, a subsequent experiment can be performed, at a new optimum current of 100 mA/g; this current would likely reduce the uncertainty to a value of about  $1 \times 10^{-3} \text{ s}^{-1}$ .

It can be seen from Figure 5.7 that there is an optimal applied current and that the optimal discharge current varies depending on the value of  $k_{\beta,TRUE}$ ; as the value of  $k_{\beta,TRUE}$  increases, the optimum discharge current also increases. This is a reasonable conclusion because as the system kinetics increase, the higher the experimental rate needed to accurately investigate kinetics.

It should be noted that the minimum  $\sigma_{k_{\beta}}$  does not necessarily correlate with the most accurate value of  $\mu_{k_{\beta}}$  (i.e. the minimum  $\sigma_{k_{\beta}}$  does not imply  $\mu_{k_{\beta}} = k_{\beta,TRUE}$ ). The methodology outlined here can also be used to test different types of experiments (e.g. constant voltage experiments, constant power, galvanostatic interrupt titrations) in addition to testing different operating conditions.

The left side of Figure 5.7 shows theoretically that this process can be used, but is this process *actually* informative? The right side of Figure 5.7 shows how the apparent value of  $k_{\beta}$  and its uncertainty vary with applied current when  $k_{\beta,TRUE} = 5 \times 10^{-3} \text{ s}^{-1}$ ; this was the value of  $k_{\beta}$  proposed by Brady et al.<sup>36</sup> The simulated results are overlaid with experimental data at four different current rates: C/10, C/5, C/2, and 1C (36, 72, 180, 360 mA/g, respectively). It is observed that the experimentally determined values of  $\mu_{k_{\beta}}$  and  $\sigma_{k_{\beta}}$  agree with the values determined from the mock experiments, which validates this methodology and confirms that simulations in combination with the framework outlined in this paper can be leveraged to help design experiments for maximum utility.

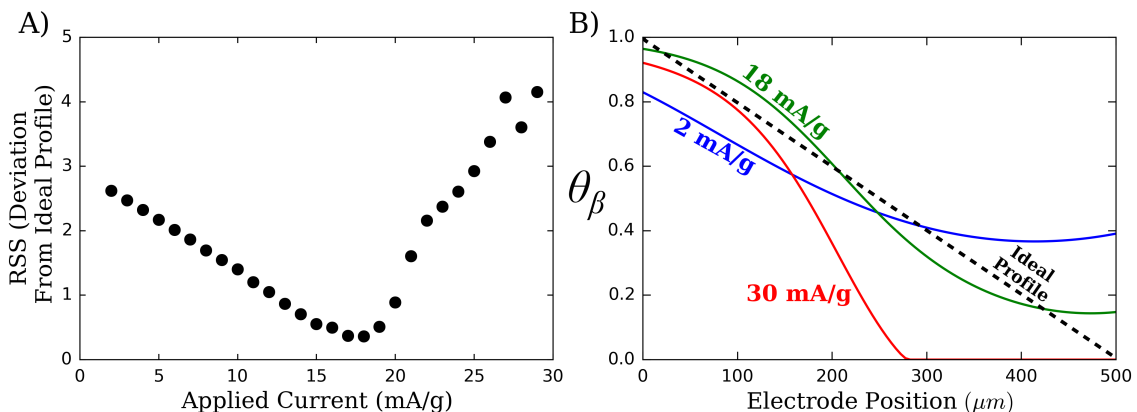


**Figure 5.8:** The plot on the left shows how the best simulated  $\theta_{\beta}$  profile compares to the ideal profile as a function of applied current. The plot on the right shows representative  $\theta_{\beta}$  plots for three current rates: 2, 18, and 30 mA/g as well as the defined ideal profile.

In the previous sections, simulations have been used to deduce parameter values, but this framework can also be used to maximize other metrics; one obvious metric is performance, but here we examine how this framework can be used to optimize characterization conditions. Coin cells are relatively cheap to fabricate and test, so it is reasonable that an experimental group could quickly make and test multiple coin cells and bypass the simulations entirely and do the optimization empirically. However, there are experiments that are more expensive to conduct, for instance conducting operando EDXRD experiments on a synchrotron beam line may be expensive, with limited opportunities for using such state of the art facilities. In these instances, using simulations to guide experimental endeavors is useful to maximize the utility of these opportunities.

Figure 5.8 shows a hypothetical optimization of design parameters for an operando EDXRD experiment. Assuming the physical parameters of the electrode are known, how can the applied current be tailored to achieve an optimal profile of the  $\beta$ -phase volume fraction,  $\theta_\beta$ , during the experiment? The ideal profile needs to be informed by experimental experience, but here it was assumed that a profile spanning the full range of possible  $\theta_\beta$  values over the full length of the electrode was best; i.e. it is neither ideal to have a profile that is flat (does not vary) across the electrode, nor is it ideal to have a sharp step-change in the profile. Using the physical parameters outlined by Brady et al.<sup>47</sup> and assuming an electrode length of 500  $\mu\text{m}$ , simulations were run to determine the optimal applied current. Figure 5.8A shows how the profiles generated at different current rates deviate from the ideal profile; this deviation was calculated using equation 5.12, where  $\theta_{\beta,j}$  are the ideal volume fractions of the  $\beta$ -phase at the electrode positions and  $\hat{\theta}_{\beta,j}$  are the simulated volume fractions of the  $\beta$ -phase at the electrode positions. It was also assumed that the EDXRD gauge thickness is 20  $\mu\text{m}$  so the total number of observations is 25. It was found that the current rate that minimized this deviation was 18 mA/g.

$$RSS = \sum_{j=1}^{n=25} \left( \theta_{\beta,j, \text{mock}} - \hat{\theta}_{\beta,j} \right)^2 \quad (5.12)$$

Figure 5.8B shows representative profiles for 2, 18, and 30 mA/g. From Figure 5.8B

it is seen that at 30 mA/g, from 300-500  $\mu\text{m}$  the volume fraction of the  $\beta$ -phase is 0. This is not ideal because scan time is wasted over that range and would give no additional information. Another constraint may be the total experimental time. The  $\beta$ -phase profile produced at 18 mA/g is optimal, but 18 mA/g also corresponds to C/20; 20 hours for one synchrotron experiment may be too expensive. In contrast, the 30 mA/g profile is not ideal, but that experiment corresponds to a rate of C/12 (it would take 12 hours), which may be more feasible. Researchers must weigh the improvement in information obtained versus the cost of beam time.

## 5.4 Conclusion

The authors do not anticipate that the expertise and intuition of expert physical modelers can be easily replaced by software. However, the recent advances in computational capabilities as well as data science algorithms are significant. This paper has outlined how some of these algorithms can be effectively applied to battery science, but further work is necessary for mathematical modelers to stay abreast of the developments in data science and remain informed of how they can be applied to battery studies. Implementation of computationally scalable techniques has the potential to improve the productivity of modelers as well as strengthen the conclusions of modeling studies. The physical insights provided by these techniques in regard to the  $\text{LiV}_3\text{O}_8$  and  $\text{Fe}_3\text{O}_8$  electrodes are consistent with previous studies. The novelty of this paper is that the same conclusions can be reached using a methodology that is more quantitative, provides more information about the fitted physical parameters, minimizes human time, and is computationally scalable.

## 5.5 Acknowledgements

This research was supported by the Center for Mesoscale Transport Properties, an Energy Frontier Research Center supported by the U.S. Department of Energy (DOE), Office of Science, Basic Energy Sciences (BES), under award #DE-SC0012673. We ac-

knowledge computing resources from Columbia University's Shared Research Computing Facility project, which is supported by NIH Research Facility Improvement grant 1G20RR030893-01, and associated funds from the New York State Empire State Development, Division of Science Technology and Innovation (NYSTAR) Contract C090171, both awarded April 15, 2010. The authors would also like to thank Timothy Jones whose expertise in statistics was influential in the understanding and application of the Markov-Chain Monte-Carlo analysis.

## 5.6 Bibliography

- [1] H. Koh and C. L. Magee, *Technological Forecasting and Social Change*, **73**(9), 1061 (2006).
- [2] W. D. Nordhaus, *The Journal of Economic History*, **67**(1), 128 (2007).
- [3] V. Venkatasubramanian, *AIChE Journal*, **55**(1), 2 (2009).
- [4] D. Silver, A. Huang, C. J. Maddison, A. Guez, L. Sifre, G. Van Den Driessche, J. Schrittwieser, I. Antonoglou, V. Panneershelvam, M. Lanctot, S. Dieleman, D. Grewe, J. Nham, N. Kalchbrenner, I. Sutskever, T. Lillicrap, M. Leach, K. Kavukcuoglu, T. Graepel, and D. Hassabis, *Nature*, **529**(7587), 484 (2016).
- [5] D. Silver, J. Schrittwieser, K. Simonyan, I. Antonoglou, A. Huang, A. Guez, T. Hubert, L. Baker, M. Lai, A. Bolton, Y. Chen, T. Lillicrap, F. Hui, L. Sifre, G. van den Driessche, T. Graepel, and D. Hassabis, *Nature*, **550**(7676), 354 (2017).
- [6] Y. Tian, K. Pei, S. Jana, and B. Ray, in *Proceedings of the 40th International Conference on Software Engineering, ICSE '18*, p. 303–314, ACM, New York, NY, USA (2018).
- [7] M. Doyle, T. F. Fuller, and J. Newman, *Journal of the Electrochemical Society*, **140**(6), 1526 (1993).
- [8] T. F. Fuller, M. Doyle, and J. Newman, *Journal of the Electrochemical Society*, **141**(1), 1 (1994).
- [9] T. F. Fuller, M. Doyle, and J. Newman, *Journal of the Electrochemical Society*, **141**(4), 982 (1994).
- [10] M. Thomas, P. Bruce, and J. Goodenough, *Journal of The Electrochemical Society*, **132**(7), 1521 (1985).
- [11] M. Doyle, J. Newman, A. S. Gozdz, C. N. Schmutz, and J.-M. Tarascon, *Journal of the Electrochemical Society*, **143**(6), 1890 (1996).

- [12] J. T. Vardner, T. Ling, S. T. Russell, A. M. Perakis, Y. He, N. W. Brady, S. K. Kumar, and A. C. West, *Journal of The Electrochemical Society*, **164**(13), A2940 (2017).
- [13] U. Krewer, F. Röder, E. Harinath, R. D. Braatz, B. Bedürftig, and R. Findeisen, *Journal of The Electrochemical Society*, **165**(16), A3656 (2018).
- [14] E. Chemali, P. J. Kollmeyer, M. Preindl, R. Ahmed, and A. Emadi, *IEEE Transactions on Industrial Electronics*, **65**(8), 6730 (2018).
- [15] N. Dawson-Elli, S. B. Lee, M. Pathak, K. Mitra, and V. R. Subramanian, *Journal of The Electrochemical Society*, **165**(2), A1 (2018).
- [16] A. M. Bizeray, J.-H. Kim, S. R. Duncan, and D. A. Howey, *IEEE Transactions on Control Systems Technology*, (99), 1 (2018).
- [17] J. C. Forman, S. J. Moura, J. L. Stein, and H. K. Fathy, in *Proceedings of the 2011 American Control Conference*, p. 362–369, IEEE (2011).
- [18] J. C. Forman, S. J. Moura, J. L. Stein, and H. K. Fathy, *Journal of Power Sources*, **210**, 263 (2012).
- [19] J. Newman and W. Tiedemann, *AIChE Journal*, **21**(1), 25 (1975).
- [20] S. Santhanagopalan, Q. Guo, and R. E. White, *Journal of the Electrochemical Society*, **154**(3), A198 (2007).
- [21] S. M. Miller and J. B. Rawlings, *AIChE Journal*, **40**(8), 1312 (1994).
- [22] Z. K. Nagy and R. D. Braatz, *IEEE Transactions on Control Systems Technology*, **11**(5), 694 (2003).
- [23] D. L. Ma, S. H. Chung, and R. D. Braatz, *AIChE Journal*, **45**(7), 1469 (1999).
- [24] B. Srinivasan, D. Bonvin, E. Visser, and S. Palanki, *Computers & Chemical Engineering*, **27**(1), 27 (2003).

- [25] S. Santhanagopalan and R. E. White, *Russian Journal of Electrochemistry*, **53**(10), 1087 (2017).
- [26] J. V. Beck and K. J. Arnold, *Parameter Estimation in Engineering and Science*, John Wiley & Sons Inc., New York, NY (1977).
- [27] M. W. Hermanto, N. C. Kee, R. B. Tan, M.-S. Chiu, and R. D. Braatz, *AIChE Journal*, **54**(12), 3248 (2008).
- [28] N. Metropolis, A. Rosenbluth, M. Rosenbluth, A. Teller, and E. Teller, *The Journal of Chemical Physics*, **21**(6), 1087–1092 (1953).
- [29] G. James, D. Witten, T. Hastie, and R. Tibshirani, *An Introduction to Statistical Learning*, p. 176–186, Springer Texts in Statistics, Springer New York, New York, NY (2013).
- [30] L. Breiman and P. Spector, *International Statistical Review / Revue Internationale de Statistique*, p. 291–319 (1992).
- [31] R. Kohavi, in *Proceedings of the 14th International Joint Conference on Artificial Intelligence - Volume 2, IJCAI'95*, p. 1137–1143, Morgan Kaufmann Publishers Inc., San Francisco, CA, USA (1995).
- [32] V. Ramadesigan, K. Chen, N. A. Burns, V. Boovaragavan, R. D. Braatz, and V. R. Subramanian, *Journal of The Electrochemical Society*, **158**(9), A1048 (2011).
- [33] M. F. Samadi, S. M. Alavi, and M. Saif, in *2013 American Control Conference*, p. 4693–4698, IEEE (2013).
- [34] R. Tibshirani, *Journal of the Royal Statistical Society. Series B (Methodological)*, **58**, 267 (1996).
- [35] D. L. Ma and R. D. Braatz, *IEEE Transactions on Control Systems Technology*, **9**(5), 766 (2001).

- [36] N. W. Brady, Q. Zhang, K. W. Knehr, P. Liu, A. C. Marschilok, K. J. Takeuchi, E. S. Takeuchi, and A. C. West, *Journal of the Electrochemical Society*, **163**(14), 2890 (2016).
- [37] K. W. Knehr, N. W. Brady, C. N. Lininger, C. A. Cama, D. C. Bock, Z. Lin, A. C. Marschilok, K. J. Takeuchi, E. S. Takeuchi, and A. C. West, *ECS Transactions*, **69**(1), 7 (2015).
- [38] K. W. Knehr, N. W. Brady, C. A. Cama, D. C. Bock, Z. Lin, C. N. Lininger, A. C. Marschilok, K. J. Takeuchi, E. S. Takeuchi, and A. C. West, *Journal of The Electrochemical Society*, **162**(14), A2817 (2015).
- [39] B. Efron, in *Breakthroughs in Statistics*, p. 569–593, Springer (1992).
- [40] B. Efron and R. J. Tibshirani, *An Introduction to the Bootstrap*, CRC press (1994).
- [41] G. James, D. Witten, T. Hastie, and R. Tibshirani, *An Introduction to Statistical Learning*, p. 187–190, Springer Texts in Statistics, Springer New York, New York, NY (2013).
- [42] naught101, `sobol_seq` (2015–), [https://pypi.org/project/sobol\\_seq/](https://pypi.org/project/sobol_seq/) [Accessed 8-January-2018].
- [43] H. Niederreiter, *Journal of Number Theory*, **30**(1), 51 (1988).
- [44] W. K. Hastings, *Biometrika*, **57**(1), 97–109 (1970).
- [45] T. Hastie, R. Tibshirani, and J. Friedman, *Elements of Statistical Learning: Data Mining, Inference, and Prediction*, Springer Series in Statistics, NY, New York, 2nd edition (2009).
- [46] G. James, D. Witten, T. Hastie, and R. Tibshirani, *An Introduction to Statistical Learning*, p. 219–228, Springer Texts in Statistics, Springer New York, New York, NY (2013).

- [47] N. W. Brady, Q. Zhang, A. Bruck, D. C. Bock, C. A. Gould, A. C. Marschlok, K. Takeuchi, E. Takeuchi, and A. C. West, *Journal of The Electrochemical Society*, **165**(2), A371 (2018).

# Chapter 6

## Conclusion

Chapters 2, 3, and 4 have shown that mathematical models are effective tools to explore a variety of physical phenomena that occur in batteries: surface layer formation, solid-state transport and phase change, as well as electrode scale processes. Through careful experimentation and thoughtful model development, these physical models provide accurate simulation of battery physics as evidenced by their agreement with electrochemical measurements and, when available, operando characterization data, such as energy dispersive x-ray diffraction (EDXRD). Chapter 5 provided evidence that many aspects of the model development process can be outsourced to computer algorithms without loss of fidelity or physical inference.

The author hopes that the reader understands that:

1. Mathematical modeling is a highly effective tool researchers have to interrogate batteries and that physical models provide unique insights that can be inaccessible through experimentation alone.
2. Just as modeling does not provide a full replacement of experimental research, data science algorithms are unlikely to fully replace mathematical models and modelling experts. However, battery researchers, especially modeling experts, need to keep abreast of the developments occurring within the field of data science because these fields are rapidly advancing the utility of computational resources, and therefore implicitly the utility of numerical simulations themselves. Simple awareness of developments in the field of data science will, if not already, provide a significant boost in research productivity by decreasing both the human time spent and financial funds necessary to develop predictive, physically intuitive models.

The full potential of leveraging both physical models and algorithmic approaches has not been reached yet. It was shown in Chapter 5 that accurate models in conjunction with efficient algorithms can be leveraged to design more physically insightful experiments. Using the same infrastructure, these tools will be instrumental in designing optimal battery architectures, such as the ratio of binder, conductive additive, and active material, as well as the optimal electrode thickness and material loading. In addition,

these tools will be essential in developing optimal control schemes and in resolving the real-time state of charge of battery devices, which are fundamental to the wide-scale penetration of batteries into the electric vehicle market as well as grid-level energy storage.